PROBING LOW GRAVITY GRADIENT WITH LISA PATHFINDER

Der QUEST-Leibniz-Forschungsschule der
Gottfried Wilhelm Leibniz Universität Hannover
zur Erlangung des Grades
Doktor der Naturwissenschaften
Dr. rer. nat.

genehmigte Dissertation

von

M.Sc. und Dipl.-Math. NATALIA KORSAKOVA
geboren am 26.02.1985 in Leningrad, USSR

2015

REFERENT: Prof. Dr. rer. nat. Karsten Danzmann
AEI Hannover

KORREFERENT: Dr. Jonathan R. Gair
The University of Edinburgh

KORREFERENT: Prof. Dr. Timothy Sumner
Imperial College London

TAG DER DISPUTATION: 26.11.2015

Curioser and curioser!

— Alice

ABSTRACT

The LISA Pathfinder mission will have a unique opportunity to test alternative theories of gravity after the main task of verifying technologies for future space-based gravitational wave detectors has been accomplished. Requiring no additional modifications, the precise gradiometer on board of LISA Pathfinder (LPF) can be sent from the first Sun–Earth Lagrange point to the Sun–Earth saddle point (SP), a special position within the Solar System where the gravity gradient becomes very low. The motivation for this proposal is that there is a large class of alternative theories of gravity that predict deviations from Newtonian gravity for small gravitational accelerations. These theories were originally motivated by the observation of galaxy rotation curves and emerged as an alternative attempt (alternative to dark matter) to explain the discrepancies between the observations and predictions. In order to verify the scientific feasibility of an SP mission, we must investigate which type of signal can be sensed by the instrument and what impact it can make on existing theories.

First, it is necessary to define the spacecraft trajectory in terms of parameters that can be inferred from the position of the spacecraft relative to the SP and the alignment of the sensitive axes of the LPF instrument. Given the uncertainty on the determination of the spacecraft position and alignment, we have shown that they will not influence the prediction for the measurement of the gravity gradient.

Thereafter, the alternative theories of gravity parameters can be investigated independently from the trajectory parameters. A study of the parameter estimation for Tensor-Vector-Scalar (T*e*V*e*S) theories determines the parameter space that is accessible to our experiment and the impact on the theory that a null result will make.

Furthermore, feasible spacecraft trajectories allow us to perform an SP flyby measurement only once or twice and from the LPF test campaign we know that during the measurement so-called *glitches* can occur. For these reasons, we developed a *glitch* model and investigated the impact of a *glitch* in the data during the flyby. Moreover, an analysis of the detector noise indicates that the background noise is better described by a *Student's t* distribution rather than a Gaussian. In addition, a generalised model for the signal is proposed and a mapping of the generalised signal parameter space to the parameter space of TeVeS signals is demonstrated. The generalised signal and the glitch models are studied within a Bayesian model selection framework. The study shows that our methods will be effective in determining whether a detector glitch or a signal is present in the LPF data.

Keywords: Bayessian data analysis, alternative theories of gravity, space-born gravitational wave detectors

ZUSAMMENFASSUNG

Die LISA Pathfinder Mission hat die einzigartige Gelegenheit, alternative Gravitationstheorien zu testen, nachdem sie ihre Hauptaufgabe abgeschlossen hat, die darin besteht, Technologien für zukünftige weltraumgebundene Gravitationswellendetektoren zu verifizieren. LISA Pathfinder (LPF) kann zu diesem Zweck vom ersten Sonne-Erd-Lagrangepunkt zum Sonne-Erd-Sattelpunkt (SP) transferiert werden, ohne dass zusätzliche Modifikationen des hochpräzisen Gradiometers nötig sind. Der SP ist ein spezieller Ort im Sonnensystem, an dem der Gravitationsgradient sehr klein ist. Die Motivation für diesen Missionsvorschlag ist, dass es eine große Klasse alternativer Gravitationstheorien gibt, die eine Abweichung von Newtons Gravitationstheorie bei kleinen gravitativen Beschleunigungen vorhersagen. Ursprünglich wurden diese alternativen Theorien motiviert durch die Beobachtung der Rotationskurven von Galaxien und entstanden als Alternative zur Dunklen Materie, um die Abweichung zwischen beobachteter Rotationskurve und Vorhersage zu erklären. Um den wissenschaftlichen Wert einer SP-Mission zu evaluieren, muss man bestimmen, welche Art von Signal das LPF-Instrument eigentlich messen kann und welche Auswirkung das auf die bestehenden alternativen Theorien hätte. Die vorliegende Arbeit konzentriert sich dabei auf die folgenden drei Themen.

Erstens ist es notwendig, die Flugbahn des Satelliten zu definieren. Die dabei relevanten Parameter leiten sich von der Position des Satelliten relativ zum SP und von der Ausrichtung der sensitiven Achsen des LPF-Instruments ab. Mit einer angenommenen Unsicherheit in der Bestimmung der Satelliten-Position und -Orientierung haben wir gezeigt, dass die resultierenden Unsicherheiten der Flugbahn-Parameter nicht die Vorhersage für die Messung des Gravitationsgradienten beeinflussen.

Zweitens, da der gemessene Gravitationsgradient unabhängig von den Fehlern der Flugbahn-Parameter ist, können wir die Parameter der alternativen Theorien getrennt von den Flugbahn-Parametern des Satelliten betrachten. Die Untersuchung der Parameter-Abschätzung für Tensor-Vektor-Skalar-Theorien (TeVeS) bestimmt den Parameterraum, der für unser Experiment zugänglich ist und den Einfluss einer Null-Messung auf die entsprechende alternative Theorie. Realisierbare Satelliten-Flugbahnen erlauben bestenfalls eine zweimalige Durchführung unseres Experiments. Ferner ist aus LPF Testmessungen bekannt, dass es während der Messung zu einer Störung, einem sogenannten "Glitch", kommen kann. Daher haben wir drittens untersucht, welchen Einfluss ein "Glitch" in den Daten während eines Vorbeiflugs am SP hat. Dafür wurde eigens ein "Glitch"-Modell entwickelt. Desweiteren hat eine Analyse des Detektor-Rauschens gezeigt, dass das Hintergrund-Rauschen besser durch "Student’s t"-Verteilung als durch eine Gauß-Verteilung beschrieben wird. Darüber hinaus wird ein generalisiertes Modell für das Signal vorgeschlagen und eine Abbildung des generalisierten Signal-Parameterraums in den TeVeS-Signal-Parameterraum demonstriert. Das generalisierte Signal und die "Glitch"-Modelle werden innerhalb eines Bayesianischen Modell-Auswahl-Rahmens untersucht. Diese Untersuchung zeigt, dass sich mit unseren Methoden eindeutig zwischen einem "Glitch" und einem Signal in den LPF-Daten unterscheiden lässt.

Schlagwörter: Bayessche Datenanalyse, Alternative Gravitationstheorien, Weltraumgebundene Gravitationswellendetektoren

CONTENTS

---

i GRAVITY AND GRAVITATIONAL WAVE ASTRONOMY 3
1 INTRODUCTION TO GRAVITATIONAL WAVE ASTROPHYSICS 5
  1.1 General relativity and Gravitational waves 5
    1.1.1 Einstein's field equations 5
    1.1.2 Weak field limit 7
    1.1.3 Plane wave 7
    1.1.4 The transverse traceless gauge 8
    1.1.5 Effect of the gravitational wave on test mass following geodesics 10
    1.1.6 Polarisation of the gravitational waves 11
    1.1.7 Generation of the gravitational waves 13
  1.2 Detectors and sources 15
    1.2.1 Energy loss by the radiating system 15
    1.2.2 Sources of gravitational waves 17
    1.2.3 Frequencies of gravitational waves 25
    1.2.4 Detection 26
    1.2.5 Sensitivity of laser detectors 32
    1.2.6 Ground based laser interferometer detectors 34
    1.2.7 Pulsar timing 34
  1.3 Detection of Gravitational Waves in Space 35
2 ACTION PRINCIPLE FOR GRAVITY THEORIES 41
  2.1 General Relativity derived from Action Principle 41
    2.1.1 Einstein-Hilbert Action 41
  2.2 Modifications of the action of Gravity 44
    2.2.1 Validity of gravitational theories 44
    2.2.2 f(R) theories of Gravity 46
    2.2.3 Theories with additional dimensions – Kaluza-Klein Gravity 46
    2.2.4 Theories with the additional fields 47
3 LISA PATHFINDER 51

3.1 LISA Pathfinder – Technology Demonstration for LISA 51
3.2 Mission timeline 52

ii MISSION EXTENSION 57

4 TESTING GRAVITY IN THE WEAK FIELD LIMIT 59
4.1 Gravity theories with an additional scalar field 59
4.2 Objectives for modifications of gravity 60
4.3 TeVeS theory as an example 62
4.4 Non-relativistic limits of TeVeS 63
4.5 Parameters of the theories 65
5 LISA PATHFINDER MEASUREMENT 67
5.1 Newtonian limit of GR 67
5.2 Measurements of the gravity stress tensor 68
5.3 Noise sources in the LISA Pathfinder measurement 69
5.4 Extended mission trajectories 71
5.5 Spacecraft navigation and parameterisation of the trajectory 73
5.5.1 Parameterisation of the trajectory 73
6 SIGNAL TEMPLATES 79
6.1 Numerical solutions for non-relativistic limit of TeVeS 79
6.2 Generation of templates 81
6.3 Newtonian stress tensor 83

iii DATA ANALYSIS 85

7 MISSION PARAMETERS ANALYSIS 87
7.1 Data model 87
7.2 Mission parameters analysis 87
7.2.1 signal-to-noise ratio (SNR) as a function of mission parameters 90
7.2.2 SNR loss due to mismatched mission parameters 93
8 DATA ANALYSIS FOR THEORETICAL PARAMETERS 101
8.1 Bayesian approach to data analysis 101
8.1.1 Analysis of the theory parameters 101
8.1.2 Bayesian parameter estimation 102
8.1.3 Prior space 103

8.2 Model selection 106
8.3 Results 108
  8.3.1 Parameter estimation 111
  8.3.2 The no signal injection case 115
  8.3.3 Model Selection 118
8.4 Conclusions 121

iv MODEL SELECTION 129
9 DETECTOR NOISE ARTEFACTS. MODEL SELECTION BETWEEN GLITCHES AND SIGNALS 131
9.1 The glitch problem 131
9.2 Real Optical Metrology System noise from the test campaign 133
  9.2.1 Non-Gaussianities in interferometric measurements 133
  9.2.2 Test campaign data for LPF 134
9.3 LISA Pathfinder software simulator 135
9.4 Conversion of the displacement data to acceleration 136
9.5 Typical non-Gaussianities observed in the data 139
9.6 Modelling noise artefacts 144
9.7 Model of the signal 146
  9.7.1 Two parameter model of the signal 146
  9.7.2 Prior ranges on parameters 147
9.8 Signal, noise and glitch models 149
9.9 Artificial data 152
9.10 Student's t likelihood 153
  9.10.1 Prior for the variance 154
  9.10.2 Marginalised likelihood 155
  9.10.3 Choice of the parameter values 156
9.11 Performance of the model selection 156
  9.11.1 Bayes Factor distributions for data with only noise present $\tilde{d}_j = \tilde{n}_j$ 159
  9.11.2 Bayes Factor distributions for data with a signal present $\tilde{d}_j = \tilde{s}_j + \tilde{n}_j$ 161

9.11.3 Bayes Factor distributions for data with a glitch present $\tilde{d}_j = \tilde{g}_j + \tilde{n}_j$ and a mixture of signal and glitch $\tilde{d}_j = \tilde{s}_j + \tilde{g}_j + \tilde{n}_j$. 162
9.12 Parameter estimation for glitches and signals 169
9.13 Conclusions on the model selection 175

V CONCLUSIONS AND FUTURE PLANS 177
10 CONCLUSIONS AND FUTURE PLANS 179
10.1 Data analysis framework for mission extension 179
10.2 Future work 180
10.2.1 Observations of the planetary motions in the Solar System 180
10.2.2 Pulsar timing tests 181

vi APPENDIX 183
A DEFINITION OF THE FOURIER TRANSFORM 185

BIBLIOGRAPHY 205

ACRONYMS

LPF	LISA Pathfinder
LTP	LISA Technology Package
DRS	Disturbance Reduction System
LISA	Laser Interferometer Space Antenna
ESA	European Space Agency
T*e*V*e*S	Tensor-Vector-Scalar
MOND	MOdified Newtonian Dynamics
SNR	signal-to-noise ratio
ASD	Amplitude Spectral Density
PSD	Power Spectral Density
GR	General Relativity
OMS	Optical Metrology System
LTP	LISA Technology Package
OSTT	On-Station Thermal Tests
ASD	Astrium Deutschland
SP	saddle point
IS	Inertial Sensor
DFT	Discrete Fourier Transform
DECIGO	DECI-Hertz Interferometer Gravitational wave Observatory

OB	Optical Bench
iABG	Industrieanlagen-Betriebsgesellschaft mbH
ST	Star Tracker
DFACS	Drag-Free Attitude Control System
OBC	On-board Computer
LTPDA	LISA Technology Package Data Analysis
cdf	cumulative distribution function
pdf	probability density function

PREFACE

The LPF is an experiment that was designed to test novel technologies that are required to detect gravitational waves in space. This thesis will be dedicated to the proposed mission extension for LPF to test a class of theories of gravity that predict deviations from General Relativity (GR) for small gravity gradients. In particular it is focused on the data analysis and investigation of the impact that the results of this experiment can make to restrict some modified theories of gravity.

To explain the origins of the LPF experiment and the reasons why it can be used for testing theories of gravity we will start with an overview of Gravitational Wave Astronomy and formulations of Gravity theories, which will be introduced in Chapters 1 and 2 respectively. First the GR equations, and gravitational waves as their solution, will be given with the insight into the experiments designed to directly detect and observe gravitational waves. Thereafter we will consider the derivation of GR from the action principle and the ways in which the action can be modified.

LPF as a testbed for precise laser interferometry distance measurements in space and drag-free control of the free falling test masses, will provide the evidence for the feasibility of building a space laser interferometer for gravitational wave measurements. The overview of the design implementations and in particular the description of the Optical Metrology System (OMS) and drag-free control will be given in Chapter 3. Moreover we give an outline of the mission timeline, followed by the description of the trajectories and the navigation of the spacecraft.

Next, in Chapter 4, we give the motivation for the LPF mission extension. This arises from the discrepancies between the observations of the rotational curves of spiral galaxies and the theoretical predictions that one can make based on calculations from the observed mass in galaxies. This problem gave rise to particular class of theories with modification of gravity. They are proposed as an alternative to the commonly accepted solution to this problem, the introduction of dark matter. We describe a set of theories of gravity which try to explain these deviations, how they can be parameterised and explain how they can be tested with LPF.

In Chapter 5 we describe the measurement that would be made with LPF while passing by the Earth–Sun saddle point, and how it can be parameterised in terms of the trajectory. The gravity potential that corresponds to this trajectory will be calculated by approximating the numerical solutions.

The data analysis for the parameters of the trajectory will be given in Chapter 7. The parameter estimation for the theoretical parameters will be described in Chapter 8. Finally the application of the analysis to realistic data, a model of the glitches in the data, generalised models of the signal and the method for the model selection will be given in the Chapter 9.

We finish with the conclusions and the description of the future plans in Chapter 10.

Part I

GRAVITY AND GRAVITATIONAL WAVE ASTRONOMY

1

INTRODUCTION TO GRAVITATIONAL WAVE ASTROPHYSICS

1.1 GENERAL RELATIVITY AND GRAVITATIONAL WAVES

In this Section we give a general introduction to the theoretical foundations of the work that we will discuss in the main part of the Thesis. This would give an insight into the reasons for designing LPF and explain how we can benefit from this design beyond the main goal of the mission.

The gravitational interaction is very weak, therefore gravitational waves that we aim to measure are very small perturbations of the space-time, which require measurements of the distance between two free falling masses with an incredible precision. Hence we start with the principles on which GR is formulated, followed by the solutions of these equations in the weak field. We will review the effect that gravitational waves produce on space-time, the ways to measure them and the challenges involved in performing the measurements. The derivation of the properties of the waves, such as their polarisation and amplitude will motivate the layout of the instruments that are designed to measure them.

1.1.1 *Einstein's field equations*

We shall start with the formulation of gravity in terms of Differential Geometry. In GR space is seen as a four-dimensional curved differentiable manifold with a certain metric that determines the dynamics of the matter. At the same time, conservation of matter (stress-energy tensor) determines the form of the tensor that describes gravity [74].

Let us formulate GR in a form with two postulates and field equations [55]. The postulates are the following: local causality and local conservation of energy and momentum. Causality means that two points can be only joined by a timelike or null curve, which sets the condition on the interval to be

$$ds^2 \leqslant 0. \tag{1.1}$$

Conservation of energy-momentum means that the divergence of the stress-energy tensor should be zero

$$\nabla \cdot \mathbf{T} = 0. \tag{1.2}$$

Therefore we need an object that would represent the gravitational field and be a symmetric, divergence-free tensor like the stress energy tensor. Something like

$$\mathbf{G} = k\mathbf{T}. \tag{1.3}$$

To describe the geometry of space-time, **G** has to be constructed out of the curvature tensor and the metric. It has to be linear in the Riemann tensor, be symmetric and of second rank and have vanishing divergence [74]. There is only one tensor that satisfies these requirements: Einsteins curvature tensor **G**, which is expressed in terms of [39] the Ricci curvature tensor and metric in the following way:

$$G_{\mu\nu} = R_{\mu\nu} - \frac{1}{2} g_{\mu\nu} R. \tag{1.4}$$

The constant k, is determined from the requirement that gravity has to be Newtonian in the weak field limit, $k = 8\pi G/c^4$; written in geometrised unit system as $k = 8\pi$ [93].

There is one more term that is missing from the Einstein's field equations. To have a static solution for the evolution of the Universe he introduced the additional *cosmological constant*, Λ [40],

$$G_{\mu\nu} + \Lambda g_{\mu\nu} = \kappa T_{\mu\nu}. \tag{1.5}$$

Nowadays this cosmological constant is considered as a vacuum energy density.

1.1.2 *Weak field limit*

Let us consider the formulation of Einstein's field equations for weak gravitational fields. We will be interested in observation of gravitational waves and measurements of the gravity field far from strong sources of gravity, therefore we need a weak field approximation. This means that the metric can be presented as a sum of two components

$$g_{\mu\nu} = \eta_{\mu\nu} + h_{\mu\nu} + \mathcal{O}([h_{\mu\nu}]^2), \tag{1.6}$$

where $|h_{\mu\nu}| \ll 1$ and

$$\eta_{\mu\nu} = \begin{pmatrix} -1 & 0 & 0 & 0 \\ 0 & 1 & 0 & 0 \\ 0 & 0 & 1 & 0 \\ 0 & 0 & 0 & 1 \end{pmatrix} \tag{1.7}$$

is a Minkowski flat spacetime. Thus, gravity field equations (see Eq. 1.5) can be expanded in powers of $h_{\mu\nu}$. Keeping only the linear terms, and imposing the Lorenz gauge condition $\bar{h}^{\mu\alpha}{}_{,\alpha} = 0$, one arrives at linearised field equations

$$\bar{h}_{\mu\nu} \equiv \bar{h}_{\mu\nu,\alpha}{}^{\alpha} = -16\pi T_{\mu\nu}, \tag{1.8}$$

where $\bar{h}_{\mu\nu} \equiv h_{\mu\nu} - \frac{1}{2}\eta_{\mu\nu}h$ is a trace-reversed perturbation variable and $h \equiv h^{\alpha}{}_{\alpha} = \eta^{\alpha\beta}h_{\alpha\beta}$. The gauge condition fixes the coordinate system. The Lorentz gauge is the one in which the equations of linearised gravity have their simplest form. It sets the condition on ξ, which is the difference between two coordinate systems $x^{\mu} = x^{\mu\prime} - \xi^{\mu}$, to be $\Box\xi = 0$. Therefore the choice of coordinates is not uniquely determined and still leaves some freedom for selecting the gauge to which we will return later.

1.1.3 *Plane wave*

Far from the sources of gravity this equation will describe the propagation of the gravitational field

$$\Box\bar{h}_{\mu\nu} = 0. \tag{1.9}$$

The vacuum solution for linearised Einstein's equations (see Eq. 1.9) will be a plane monochromatic wave

$$\bar{h}_{\mu\nu} = \Re[A_{\mu\nu} \exp(ik_\alpha x^\alpha)] = \Re[A_{\mu\nu} \exp(ik_i x^i) \exp(-i\omega t)], \quad (1.10)$$

where $\mathbf{k}$ is a wave vector that can be decomposed into its time and space components $\mathbf{k} \to (k_0, k_1, k_2, k_3) = (-\omega, k_1, k_2, k_3)$ with ω being a frequency of a gravitational wave.

If we substitute the expression for the gravitational wave (Eq. 1.10) to the expression for the gravitation field (Eq. 1.9) we obtain that $\mathbf{k}$ is a null vector [93]

$$k_\alpha k^\alpha = 0. \quad (1.11)$$

This means that the frequency of the wave is $\omega = \pm\sqrt{k_1^2 + k_2^2 + k_3^2}$ and the gravitational wave propagates in the direction $(1/\omega)(k_1, k_2, k_3)$ with the speed of light. Imposing the Lorentz gauge condition

$$\bar{h}^{\mu\alpha}{}_{,\alpha} = 0 \quad (1.12)$$

gives us another restriction on $\mathbf{A}$,

$$A_{\mu\alpha} k^\alpha = 0, \quad (1.13)$$

which means that the direction of propagation for the gravitational wave $\mathbf{k}$ is orthogonal to its amplitude $\mathbf{A}$.

1.1.4 *The transverse traceless gauge*

The amplitude $A_{\mu\nu}$ has 6 independent components. However, as it was mentioned earlier, the gauge condition does not fix the coordinate system uniquely. It was

$$\Box \xi = 0. \quad (1.14)$$

We can write the solution for this equation in the form [74]

$$\xi^\mu = -iB^\mu \exp[ik_\alpha x^\alpha]. \quad (1.15)$$

This coordinate change will impose the following change in $h_{\mu\nu}$

$$h_{\mu\nu} \rightarrow h_{\mu\nu} - \xi_{\mu,\nu} - \xi_{\nu,\mu}. \tag{1.16}$$

If we substitute this in the expression for $\bar{h}_{\mu\nu}$, we can choose a coordinate system such that

$$A^{\mu}{}_{\mu} = 0 \qquad \text{and} \qquad A_{0i} = 0. \tag{1.17}$$

The last two conditions (Eq. 1.17) combined together with (Eq. 1.13) determine a *transverse traceless gauge*. Moreover these conditions fix the gauge rigidly, which means that the solutions that we have found (gravitational waves) have a physical meaning and cannot be eliminated by the gauge transformation. These conditions leave us with the two non-zero components of $A_{\mu\nu}$ representing two different polarisations. The gauge that we have chosen implies the following properties for $A_{\mu\nu}$ components:

1. $A^{0\alpha} = A^{\alpha 0} = 0$, which means that $A_{\mu\nu}$ is purely spatial;
2. condition $A^{\alpha}{}_{\alpha} = 0$ means that it is *traceless*;
3. and the relation between the spatial components $A_{ij}k_j = 0$ implies that it is *transverse*, i.e., orthogonal to the direction of propagation.

Moreover the transverse traceless condition implies that [93]

$$\bar{h}^{TT}_{\mu\nu} = h^{TT}_{\mu\nu}. \tag{1.18}$$

Therefore we will use $h_{\mu\nu}$ without the bar from now on. Also in the TT gauge the Riemann curvature tensor can be written in the form

$$R_{j0k0} = -\frac{1}{2} h^{TT}_{jk,00}. \tag{1.19}$$

Let us now assume that the spatial coordinates are chosen in a way such that the gravitational wave is travelling in the k^3 direction, then

$$k^{\mu} = (\omega, 0, 0, \omega). \tag{1.20}$$

Then $A_{\alpha 3}k^3 = 0$. Therefore if we write the first index as t, second as x, third as y and the fourth as z, the components of $A_{\mu\nu}$ can be written in matrix form as

$$(A^{TT}_{\mu\nu}) = \begin{pmatrix} 0 & 0 & 0 & 0 \\ 0 & A_{xx} & A_{xy} & 0 \\ 0 & A_{xy} & -A_{xx} & 0 \\ 0 & 0 & 0 & 0 \end{pmatrix}. \tag{1.21}$$

Hence there are two independent components A_{xx} and A_{xy}.

1.1.5 *Effect of the gravitational wave on test mass following geodesics*

When one particle is following a geodesic the effect of a gravitational wave passing by will not be observable. This means that the particle remains at the same coordinate position. Therefore to observe the effect of the gravitational waves we have to measure the change in the distance between two freely falling particles by computing a coordinate independent quantity – a proper distance between two particles. Let us, for the illustration purposes, consider the distance between two free falling particles

$$\begin{aligned} \Delta l \equiv \int |ds^2|^{1/2} = \int |g_{\alpha\beta}dx^{\alpha}dx^{\beta}|^{1/2} = & \\ \int \big(-dt^2 + dz^2 + & \\ [1 + \Re(A_{xx}\exp[ik_{\alpha}x^{\alpha}])]dx^2 + & \\ 2\Re(A_{xy}\exp[ik_{\alpha}x^{\alpha}])dxdy + & \\ [1 - \Re(A_{xx}\exp[ik_{\alpha}x^{\alpha}])]dy^2\big)^{-1/2}, & \end{aligned} \tag{1.22}$$

where $x^{\alpha} = (it, x, y, z)$. If the separation between particles is only along the x-axis, i.e, $dx = \epsilon$, then Δl becomes

$$\Delta l = \int_0^{\epsilon} \sqrt{g_{xx}}dx = \int_0^{\epsilon} \sqrt{\eta_{xx} + h_{xx}}dx \approx (1 + \frac{1}{2}h_{xx})\epsilon. \tag{1.23}$$

The rigorous way to derive the effect of the gravitational wave is to look at how it influences the geodesics as a tidal force. Let us say that we have two geodesics, one of which we define as A and the other one B. Let us assume that the reference frame is co-moving with the particle A, such that $x_A^j = 0$ and $x_A^0 = \tau$ (coordinate time equal to the proper time). The distance between two geodesics can be defined as

$$\xi^j = x_B^j - x_A^j. \tag{1.24}$$

Following [74] we can write the expression for the tidal acceleration between two test particles as

$$\frac{d^2\xi^j}{dt^2} = -R_{j0k0}\xi_k = \frac{1}{2}\frac{\partial^2 h_{jk}}{\partial t^2}\xi^k. \tag{1.25}$$

Thus we have a differential equation that determines the acceleration of the particle B in the reference frame of particle A. It can be interpreted as a tidal force pushing on the particle B. This is an important equation because it shows how the gravitational wave distorts space time and how it can be measured, either by measuring the tidal force applied to a body or a change in the distance between two free falling particles. Some ways to measure gravitational waves based on these two principles will be discussed later in Sec. (1.2.4).

1.1.6 *Polarisation of the gravitational waves*

The tidal stress induced by a gravitational wave (see Eq. 1.25) acts like an oscillating tidal force on the free falling test particles in the direction orthogonal to the propagation of the gravitational wave

$$\frac{d^2\xi^j}{dt^2} = \Re\left(-\frac{1}{2}\omega^2 A_0 \exp[-i\omega(t-z)e_{Pjk}\xi^k]\right), \tag{1.26}$$

where $\mathbf{e}_P$ is the polarisation tensor. The field lines are graphically presented in Fig. 1.

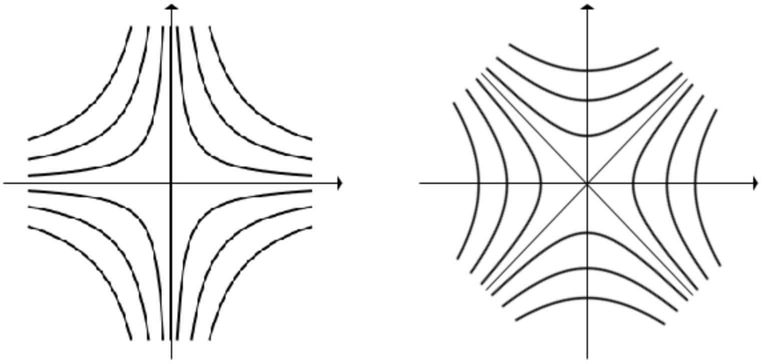

(a) Plus polarisation (b) Cross polarisation

Figure 1: Field lines of the stress tensor from an oscillating gravitational wave.

Moreover from the metric perturbations induced by gravitational waves in transverse traceless gauge we have seen that

$$(h^{TT}_{\mu\nu}) = \Re\left\{\begin{pmatrix} 0 & 0 & 0 & 0 \\ 0 & A_+ & A_\times & 0 \\ 0 & A_\times & -A_+ & 0 \\ 0 & 0 & 0 & 0 \end{pmatrix} \exp[-i\omega(t-z)]\right\}. \quad (1.27)$$

We have rewritten the non-zero amplitudes as $A_+ = A_{xx} = -A_{yy}$ and $A_\times = A_{xy} = A_{yx}$. They represent the two independent polarisation modes of gravitational waves.

A gravitational wave can be decomposed into either two linearly or two circularly polarised components. For the *plus* (see Fig. 2) and *cross* (see Fig. 3) polarisations we can write in terms of the unit polarisation vectors $\mathbf{e}_x$ and $\mathbf{e}_y$ [74]

$$\begin{aligned} \mathbf{e}_+ &\equiv \mathbf{e}_x \otimes \mathbf{e}_x - \mathbf{e}_y \otimes \mathbf{e}_y \quad (1.28) \\ \mathbf{e}_\times &\equiv \mathbf{e}_x \otimes \mathbf{e}_y + \mathbf{e}_y \otimes \mathbf{e}_x . \end{aligned}$$

And the circular polarisation can be given as the decomposition of the following unit vectors $\mathbf{e}_R$ and $\mathbf{e}_L$

$$\begin{aligned}\mathbf{e}_R &= \frac{1}{\sqrt{2}}(\mathbf{e}_+ + i\mathbf{e}_\times) \\ \mathbf{e}_L &= \frac{1}{\sqrt{2}}(\mathbf{e}_+ - i\mathbf{e}_\times).\end{aligned} \tag{1.29}$$

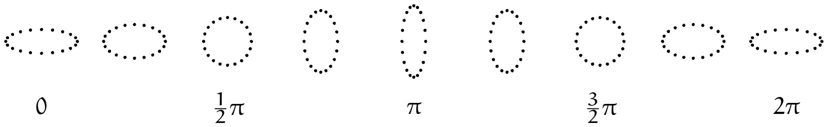

Figure 2: The impact of the plus polarised gravitational wave on a ring of particles.

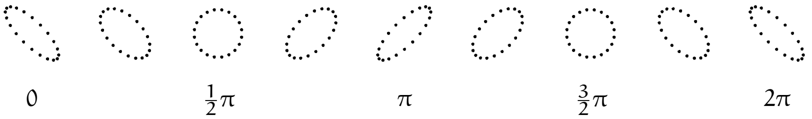

Figure 3: The impact of the cross polarised gravitational wave on a ring of particles.

1.1.7 *Generation of the gravitational waves*

To look into the generation of gravitational waves, we will start with Einstein's field equation,

$$\bar{h}_{\mu\nu} = -16\pi T_{\mu\nu}. \tag{1.30}$$

This is, however, not the transverse traceless approximation. It is based only on the assumption that the source of gravity is isolated and that spacetime becomes asymptotically flat far away from the source of gravity [74].

The solutions for this type of differential equation can be formally found with the help of the Green's function, which is defined by

$$G(x^{\alpha}) = \delta^{(4)}(x^{\alpha}). \tag{1.31}$$

Then we can write a general solution for Eq. 1.30 in the form

$$\bar{h}_{\mu\nu}(x^{\alpha}) = -16\pi \int G(x^{\alpha} - y^{\alpha}) T_{\mu\nu}(y^{\alpha}) d^4 y. \tag{1.32}$$

To solve this equation we need to find the expression for Green's function. However there is no unique solution to this problem. Therefore we need to define some additional conditions. We will look for the solution that has a physical meaning, which is the so-called *retarded* Green's function. It is zero for $x^0 \equiv t < 0$. This condition means that there is no incoming gravitational radiation and that the gravitational waves are not radiated in the past. Following [26] we can write the expression for the retarded Green's function

$$G(x^{\alpha} - y^{\alpha}) = -\frac{1}{4\pi|\mathbf{x}-\mathbf{y}|} \delta[|\mathbf{x}-\mathbf{y}| - (x^0 - y^0)] \theta(x^0 - y^0), \tag{1.33}$$

where $\mathbf{x} = (x^1, x^2, x^3)$ and $\mathbf{y} = (y^1, y^2, y^3)$. The function θ is defined as

$$\theta(x^0 - y^0) = 1, \quad x^0 > y^0 \tag{1.34}$$

$$\theta(x^0 - y^0) = 0, \quad \text{otherwise}. \tag{1.35}$$

The solution for the metric then becomes

$$\bar{h}_{\mu\nu}(\mathbf{x}, t) = 4 \int \frac{1}{r} T_{\mu\nu}(t - |\mathbf{x}-\mathbf{y}|, \mathbf{y}) d^3 y, \tag{1.36}$$

where $t - |\mathbf{x}-\mathbf{y}|$ is called the *retarded* time and we have also taken into account the far distance to the source by defining $r = |\mathbf{x}|$. Additionally we can define the second moment of the mass distribution which is called the quadrupole moment tensor as

$$I_{ij}(t) \equiv \int y^i y^j \rho(t, \mathbf{y}) d^3 y. \tag{1.37}$$

Taking into account the conservation of the stress-energy tensor and that T^{00} is the mass density ρ we can write the perturbation of the metrics in terms of a quadrupole moment tensor as

$$\bar{h}_{ij}(t,\mathbf{x}) = \frac{2}{r}\frac{d^2 I_{ij}(t-r)}{dt^2}. \tag{1.38}$$

Thus the metric perturbations produced by a gravitational wave coming from an isolated non-relativistic object are proportional to the second derivative of the quadrupole moment of the energy density. Therefore the gravitational wave can be generated only by a source with non-zero quadrupole moment. Let us now rewrite it in transverse traceless gauge. First we will remove the trace of the quadrupole moment

$$Q_{ij} = I_{ij} - \frac{1}{3}\delta_{ij} I. \tag{1.39}$$

Then using the projection operator that removes any components parallel to the direction of propagation $\mathbf{n}$,

$$P_{ij} = \delta_{ij} - n_i n_j, \tag{1.40}$$

we will form the operator that will act on the metric in the way that it transforms the metric perturbations into transverse traceless gauge

$$h_{ij}^{TT} = \bar{h}_{kl} P_{ik} P_{jl} - \frac{1}{2} P_{ij} P_{kl} \bar{h}_{kl}. \tag{1.41}$$

Hence the *quadrupole formula* for the transverse traceless gauge becomes

$$h_{ij}^{TT}(t,\mathbf{x}) = \frac{2}{r}\frac{d^2 Q_{kl}(t-r)}{dt^2}[P_{ik}(\mathbf{n})P_{jl}(\mathbf{n}) - \frac{1}{2}P_{kl}(\mathbf{n})P_{ij}(\mathbf{n})]. \tag{1.42}$$

1.2 DETECTORS AND SOURCES

1.2.1 *Energy loss by the radiating system*

We have derived that if the astrophysical system has a non-zero quadrupole moment it produces perturbations in the metric. To understand the magnitude to which the metric is perturbed we need to estimate the energy loss by the system. However there is no concept of the local energy in GR. Therefore it is not straightforward to calculate the energy loss due to gravitational radiation. We would try to derive an approximation to the energy-momentum tensor in the weak field limit, where we have been considering gravitational waves thus far. However to estimate the energy carried away by the gravitational waves we would need to take into account the metric expansion at least up to the second order of $h_{\mu\nu}$. Therefore let us then consider Einstein's field equations up to second order in the weak field approximation

$$g_{\mu\nu} = \eta_{\mu\nu} + h^{(1)}_{\mu\nu} + h^{(2)}_{\mu\nu} + o([h_{\mu\nu}]^3). \tag{1.43}$$

Then Einstein's field equations can be rewritten in the following form to include the contribution from the energy-momentum associated with the gravitational field (which is, however, not the stress-energy of the gravitational field)

$$G^{(1)}_{\mu\nu} = -8\pi(T_{\mu\nu} + t_{\mu\nu}). \tag{1.44}$$

Here $t_{\mu\nu}$ is the energy-momentum pseudo tensor. If we expand Einstein's tensor up to the second order in $h_{\mu\nu}$ and take the second term into account, we get the following approximation to the field equations

$$G_{\mu\nu} \equiv G^{(1)}_{\mu\nu} + G^{(2)}_{\mu\nu} + o(G^{(3)}_{\mu\nu}) = -8\pi T_{\mu\nu}. \tag{1.45}$$

From Eqs. 1.44 and 1.45 follows that

$$t_{\mu\nu} \equiv \frac{1}{8\pi} G^{(2)}_{\mu\nu}. \tag{1.46}$$

Therefore the correction to the space-time metric from the second order $h_{\mu\nu}$ can be considered as the contribution from the additional stress-energy tensor of the matter $t_{\mu\nu}$. The energy-momentum pseudo tensor $t_{\mu\nu}$ is not gauge invariant. To construct a gauge-invariant quantity out of this tensor we can average it over the volume surrounding the point in space-time instead of considering it at that particular point

$$t_{\mu\nu} = -\frac{1}{8\pi}\langle R^{(2)}_{\mu\nu} - \frac{1}{2}\eta_{\mu\nu} R^{(2)}\rangle. \tag{1.47}$$

Moreover let us take into account the condition that we have adopted for the generation of gravitational waves. It said that the dependence on time of the metric perturbation in the case that the wave propagates in the z direction will be $h_{\mu\nu}(t-z)$, which implies that

$$\partial_0 h_{\mu\nu} = -\partial_z h_{\mu\nu}. \tag{1.48}$$

Therefore the average taken over the space also implies averaging in time; then the expression for the energy carried by gravitational waves becomes

$$t^{GW}_{\mu\nu} = \frac{1}{32\pi}\langle(\partial_\mu h^{TT}_{ij})(\partial_\nu h^{TT}_{ij})\rangle. \tag{1.49}$$

The gravitation energy density is then

$$t_{00} = -t_{0z} = \frac{1}{32\pi}\langle \dot{h}^{TT}_{ij}\dot{h}^{TT}_{ij}\rangle = \frac{1}{16\pi}\langle \dot{h}^2_+ + \dot{h}^2_\times\rangle, \tag{1.50}$$

where t_{0z} is the energy flow along the z direction per unit area and unit time. Therefore the total emitted power is the loss of energy per unit time in all directions carried by the gravitational waves

$$\mathcal{F} = -\frac{dE}{dt} = r^2 \int_{\partial V} t^{00} d^2x, \tag{1.51}$$

which is also called the gravitational energy flux or gravitational luminosity. Following Eqs. 1.49 and 1.42 we obtain the *quadrupole formula for energy emission*

$$\mathcal{F} = \frac{1}{16\pi}\langle \dddot{Q}_{ij}\dddot{Q}_{ij}\rangle. \tag{1.52}$$

Gravitational waves also carry away angular momentum

$$\frac{dL^i}{dt} = \frac{2}{5}\epsilon^{ijk}\langle \ddot{Q}_{jl}\dddot{Q}_{lk}\rangle. \tag{1.53}$$

1.2.2 *Sources of gravitational waves*

Here some of the astrophysical objects that emit gravitational waves are reviewed. It is important to look at the estimates of the amplitudes of these waves at Earth, which show that they are all very weak and therefore require very precise instruments to detect them. We also give the estimates of frequencies for the different source. This is important to determine which method of detection best fits each sources. It was shown in the previous section that a system can radiate gravitational waves when it has non-zero quadrupole moment. Therefore the radiation of gravitational waves depends on the mass distribution. For the sources to be strong enough for us to observe them they have to be from compact objects which undergo some mass redistribution, for example, binary systems. We can support this statement with estimates of the metric perturbations based on the quadrupole formula (see Eq. 1.38)

$$\bar{h}_{jk}(t) = \frac{2}{r}\frac{G}{c^4}\ddot{I}_{ij}(t-r). \tag{1.54}$$

The magnitude of the quadrupole moment (see Eq. 1.37) can be estimated as $I = 2MR^2$, where R is the characteristic size of the system. Then if the system rotates with the period P, the above equation can be expressed as

$$\bar{h}_{jk} \simeq \frac{G}{c^4}\frac{4}{r}\frac{MR^2}{P^2}. \tag{1.55}$$

The ratio of the radius and the period can be related to each other by the velocity of the system's centre of mass $v = 2\pi R/P$, resulting in

$$\bar{h}_{ij} \simeq \frac{G}{c^4}\frac{Mv^2}{\pi^2 r}. \tag{1.56}$$

Next let us express the mass in terms of the Schwarzschild radius of the astrophysical object $M = r_s c^2/2G$, then

$$\bar{h}_{ij} \approx \frac{r_s}{r}\left(\frac{v}{c}\right)^2, \tag{1.57}$$

which states that the amplitude of the gravitational wave would be maximal when the size of the object is close to its Schwarzschild radius.

BINARY SYSTEMS of compact objects can be sources of gravitational waves. For the gravitational radiation to be considerable, the binary system has to consist of compact objects such as neutron stars, black holes or white dwarfs.

Binaries are a reliable source of gravitational radiation because the presence of gravitational waves from such systems was already indirectly observed by gathering information of the orbit shrinkage of the Hulse-Taylor pulsar.

THE HULSE-TAYLOR PULSAR was detected with the Arecibo Observatory's radio telescope in 1974 as a 59 ms pulsar. It was assigned the name *PSR 1913+16*. Russell Hulse and Joseph Taylor measured the time of the pulse arrivals, which allowed them to identify periodic changes in the observed pulsation rate. The irregularity of the frequency of pulse arrival times can be explained by the presence of a second component of a binary system that orbits around the same centre of mass as the observed pulsar. Therefore when the pulsar is at periastron the pulses arrive more frequently, compared to the time when it is at apastron when they arrive less frequently (see Fig. 4). This variation is caused by the Doppler effect. The measurements of the time of arrival of the pulses allowed to calculate the orbital parameters of the binary system and the characteristics of its components, including those in Table 1.

a	$1.95 \cdot 10^9$ m
m_1	$1.441\ M_\odot$
m_2	$1.383\ M_\odot$
e	0.617

Table 1: Parameters of the Hulse-Taylor pulsar.

In the formalism that was used in deriving the quadrupole formula, the computations can also be done using the Newtonian laws of motion. Correspondingly if we calculate the gravitational energy flux $\mathcal{F} = -dE/dt$ using the Newtonian expression for the energy of the system and Kepler's third law [21], we get the expression for the

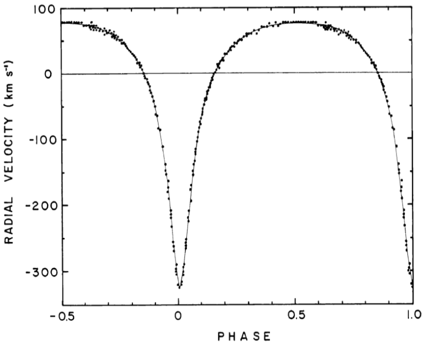

Figure 4: Figure taken from [63]. Measurements of the pulsar period, over several orbital periods. Pulsar radial velocity was calculated from the doppler shift.

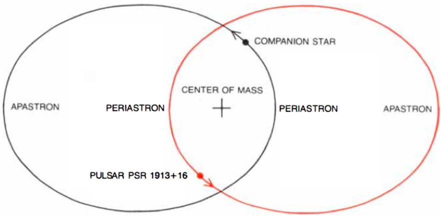

Figure 5: Figure taken from [112]. Schematic representation of the orbits of the binary system of the neutron stars inferred from the observation of the pulsar.

evolution of the orbital period of a binary system that emits gravitational waves in terms of the parameters of the orbit [103, 111] (in SI units)

$$\dot{P}_b = -\frac{192\pi G^{5/3}}{5}\left(\frac{P_b}{2\pi}\right)^{-5/3}(1-e^2)^{-7/2}\left(1+\frac{73}{24}e^2+\frac{37}{96}e^4\right)m_p m_c (m_p+m_c)^{-1/3}. \tag{1.58}$$

The energy that is emitted by gravitational waves will cause changes in the orbital motion of the binary system. It is possible to measure the decrease in the orbital period by measuring the time when the pulsar passes the periastron, compared to the time when the pulsar

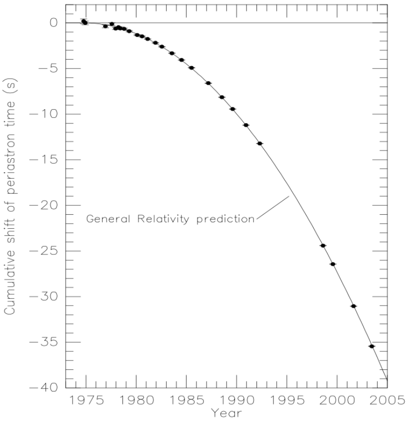

Figure 6: Figure taken from [111]. Accumulated orbit phase error with the assumption that P_b had a fixed error at 1974.7 with $\dot{P}_b = 0$.

should have passed the periastron if there was no shrinkage of the orbit. The cumulative shift builds up as the square of time passed from the time taken as the beginning of the observations, and is proportional to $\dot{P}/Pt^2$. That leads to the components spiralling inwards towards each other and to a decrease in the orbital period. The predictions agree very well with the measurements, which can be seen in Fig. 6. The observation of this pulsar as a member of a binary system led to the first indirect evidence for gravitational wave emission as predicted by GR. Since then, other pulsars have been observed in binary systems that also exhibit orbital decay; they are *PSR J0737-3039*, which is a double pulsar, and *PSR J0348+0432*, which is a pulsar – white dwarf binary system. These systems contain a pulsar component which is a very precise clock. It gives a unique opportunity to test GR in the regime of strong gravity.

COMPACT BINARY SYSTEMS are sources of gravitational waves that are close binary systems in the final stages of their evolution before coalescence. From the quadrupole formula it is possible to estimate the amplitude of gravitational waves on Earth [117] for such systems. If we consider, for simplicity, a binary system with a circular orbit and components of equal mass, then

$$h = \frac{M^{5/3}\Omega^{2/3}}{r}. \tag{1.59}$$

Then for realistic values for the mass and frequency we get the following estimates

$$h \simeq 10^{-21}\left(\frac{M}{2M_\odot}\right)^{5/3}\left(\frac{1\text{hour}}{P}\right)\left(\frac{1\text{kpc}}{r}\right). \tag{1.60}$$

Low frequency

Eq. 1.60 uses typical values of the masses, orbital periods and distances of the white dwarf binary systems in our galaxy. They are a very common source of gravitational wave radiation. The frequency of these sources lies in the range detectable by space-based observatories (see Sec. 1.3). The sky location and amplitude of the wave for some of these sources can be precisely calculated, which makes them a good test for the functionality of space-based detectors such as Laser Interferometer Space Antenna (LISA). However, because of the great number of such sources they would be considered also as a confusion noise.

If we substitute in Eq. 1.59 the characteristic values for neutron star binaries we obtain

$$h \simeq 10^{-22}\left(\frac{M}{2.8M}\right)^{5/3}\left(\frac{0.01\text{s}}{P}\right)^{2/3}\left(\frac{100\text{Mpc}}{r}\right) \tag{1.61}$$

High frequency

as an estimate of the perturbation of the gravity field on Earth from binary neutron star systems in the final stages of their evolution, when they spiral towards each other and merge. This is a likely source of gravitational waves for the ground based detectors discussed in the Sec. 1.2.4.

Hight frequency

CONTINUOUS SOURCES of gravitational waves are rotating neutron stars which can radiate gravitational waves if their crust is non-axisymmetric. This non-symmetry is defined in terms of the *ellipticity* given by

$$\epsilon = \frac{I_{xx} - I_{yy}}{I}. \tag{1.62}$$

It characterises the degree of the neutron star's distortion. The upper determined bound on *ellipticity* is from gravitational-wave observations to be $\epsilon \lesssim 10^{-6}$. In terms of the parameter ϵ the gravitational wave metric perturbation is given by [25]

$$h \sim 4\pi^2 \frac{G}{c^4} \frac{If^2\epsilon}{r}. \tag{1.63}$$

To get an order of magnitude estimate for these sources we can substitute typical values to Eq. 1.63 to obtain [25]

$$h \simeq 10^{-25} \left(\frac{\epsilon}{10^{-6}}\right) \left(\frac{I}{10^{45} \text{g cm}^2}\right) \left(\frac{10\text{kpc}}{r}\right) \left(\frac{f_{GW}}{1\text{kHz}}\right)^2, \tag{1.64}$$

which is quite small. However this type of source produces a continuous monochromatic wave, therefore SNR can be increased by accumulating measurements over a large number of cycles, N, which would increase the SNR by a factor $\sqrt{N}$.

GRAVITATIONAL COLLAPSE is a Type II supernova explosion, which is a core collapse of a massive star that forms either a neutron star or a black hole. The core collapse is very rapid and it is accompanied by motion of matter at relativistic speeds. However gravitational waves will be emitted from this source only in the case when the collapse is asymmetric. This source of gravitational waves encouraged Joseph Weber to build a bar detector – the first gravitational wave detector (see Sec. 1.2.4).

High frequency

The interesting property of these events is that they are likely to have an electromagnetic or neutrino counterpart which can be used to trigger the time when one can search for the gravitational wave in the data from detector. An estimate of the amplitude of the waves from a supernova in our Galaxy [91] is then

$$h \sim 6 \times 10^{-21} \left(\frac{E}{10^{-7} M_\odot}\right)^{1/2} \left(\frac{1\text{ms}}{T}\right)^{1/2} \left(\frac{1\text{kHz}}{f}\right) \left(\frac{10\text{kpc}}{r}\right). \tag{1.65}$$

However the event rate of supernova explosions in our Galaxy is not very high and the amplitude of the predicted wave decreases once the distance to the source would increase. For example, the distance to the Virgo cluster is tens of Mpc, which would increase the event rate but decrease the amplitude of the gravitational wave as seen on Earth.

Low frequency

MASSIVE BLACK HOLE COALESCENCES would produce low frequency gravitational waves and would be a source for a space-based gravitational wave detector. Super massive black holes have masses of $10^6 - 10^9 M_\odot$. The mergers of such black holes will accompany galactic mergers [4]. Moreover they are thought to be the black holes that power quasars, the active galactic nuclei at cosmological redshifts. With space gravitational wave detectors (see Sec. 1.3) it would be possible to observe these sources from the whole range of redshifts and masses [10], completely covering the parameter space of these sources. Furthermore, the SNRs of massive black hole mergers will be very large, making it possible to extract important astrophysical information by observing them.

Low frequency

EXTREME MASS RATIO INSPIRALS are systems of low mass stars orbiting massive black holes. For example, Solar mass black holes, neutron stars and the stars of the main sequence orbiting the supermassive black hole *Sgr A** in the centre of the Milky Way will produce this kind of gravitational waves. It would be possible to observe such sources in the local Universe to distances up to 10 Gpc [91]. The amplitude of gravitational waves will depend on whether the stars that fall on a black hole are tidally disrupted or not. The highest possible amplitude of the gravitational waves would be if the star falls on a massive black hole without any tidal disruption. The last $O(10^5)$ orbits of the inspiraling object would occure in a highly non-linear gravitational field, which would lead to a direct observation of GR in the strong limit.

All frequencies (especially interesting at low frequencies)

THE STOCHASTIC BACKGROUND is comprised of independent uncorrelated, unmodelled gravitational waves superposed with each other.Unresolved astrophysical sources are one of the contributions to the stochastic background. The other particularly interesting contribution comes from gravitational waves that are emitted in the primordial Universe from various mechanisms, such as cosmological first-order phase transition happening immediately after the Big Bang. Therefore this is a way to observe the earliest times in the history of the universe because of the weak coupling of the gravitational waves with matter. The stochastic background is described by the energy density $\rho_{gw} = t_{00} = 1/32\pi\langle \dot{h}_{ij}\dot{h}^{ij}\rangle$ per unit logarithmic frequency [117]

$$\Omega_{gw}(f) = \frac{1}{\rho_c}\frac{d\rho_{gw}}{d\ln f}, \tag{1.66}$$

where $\rho_c = 3H_0^2/8\pi G$ is the critical density required to close the Universe. The power spectrum of the gravitational wave background is [104] written as

$$S_{gw}(f) = \frac{3H_0^2}{10\pi} f^{-3}\Omega_{gw}(f). \tag{1.67}$$

It is particularly interesting to observe stochastic background in the very low frequency band because it is expected that in this frequency range it would be possible to set the tightest constraints on Ω_{gw}.

1.2.3 *Frequencies of gravitational waves*

Different sources will emit gravitational waves at different frequencies, which in the case of a binary system or a rotating neutron star will simply depend on the frequency of rotation. For example, the frequency of the gravitational wave from a periodic source will be twice the frequency of its rotation $f_{GW} = 2\Omega$. Otherwise for non-periodic sources the frequency will be determined by the *natural frequency* of the gravitating object. Depending on the frequency of the system it can be observed by different types of detectors that are sensitive to different frequency ranges. It is common [117] to distinguish the frequency ranges by the frequency ranges in which detectors are sensitive to gravitational waves in the following categories

- High frequencies (Ground based detectors)
  $1 \lesssim f \lesssim 10^4$ Hz

- Low frequencies (Space based laser interferometers)
$10^{-5} \lesssim f \lesssim 1$ Hz
- Very low frequencies (Pulsar timing)
$10^{-9} \lesssim f \lesssim 10^{-7}$ Hz
- Extremely low frequencies (Cosmic Microwave Background)
$10^{-18} \lesssim f \lesssim 10^{-13}$ Hz

1.2.4 *Detection*

Gravitational waves are very weak, requiring considerable efforts in both development of extremely sensitive instruments and refined data analysis techniques in attempts to detect gravitational waves. Here instruments to detect gravitational waves will be discussed. As shown in Sec. 1.1.5 the effect that a gravitational wave has on the metric can be seen in two ways:

- either as a tidal force (see Eq. 1.25);
- or as a change in the distance between two free falling bodies (see Eq. 1.23).

This leads to two ways of observing gravitational waves: resonant and laser detectors.

RESONANT DETECTORS were the first concept proposed for detecting gravitational waves [110], based on the measurements of a solid bar deformation. Several detectors were built based on this measurement principle.

The principle of measuring gravitational waves with a bar detector is based on considering the effect of the gravitational wave as a tidal force (see Eq. 1.25)

$$F_{gw} = \frac{1}{2} m l_0 \frac{\partial^2 h_{xx}}{\partial t^2}, \tag{1.68}$$

where m is the mass of the detector and l_0 is the length of the undeformed spring. Then we can consider our detector as two masses connected by a spring to each other. The periodic deformation of the spring due to gravitational waves can be described by the driven harmonic oscillator. For example, for the gravitational wave with the "+" polarisation the equation will look like

$$\ddot{\xi} + \dot{\xi}/\tau_0 + \omega_0^2\xi = \frac{1}{2} l_0 \ddot{h}_{xx}, \tag{1.69}$$

where τ_0 is a damping time and $\tau_0 \equiv Q/\omega_0$.

The solution of this differential equation is

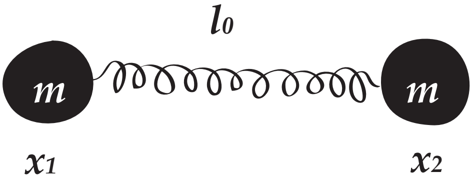

Figure 7: The scheme that represent the principle of the resonant detector. The space stretches due to the gravitational wave to $\xi = x_2 - x_1 - l_0$.

Parameters of Weber's detector

m	1410 *kg*
l_0	1.5 *m*
ω_0	1660 *Hz*
Q	$2 \cdot 10^5$

$$\xi = \frac{\frac{1}{2}\omega^2 l_0 A_{xx} e^{i\omega t}}{\omega_0^2 - \omega^2 + i\omega/\tau}. \tag{1.70}$$

The maximum response of the detector is at its resonance

$$\xi_{\mathrm{max}} = \omega_0 \tau l_0 A_{xx}/2. \tag{1.71}$$

Therefore the gravitational wave acts like an external force on a solid bar, which has its maximum sensitivity at the resonance frequency.

The typical shape for a gravitational wave detector of this kind is a cylindrical bar (see Fig. 8). Here is an example of two such detectors with their power spectral densities. On Fig. 9 it is seen that the detectors at their resonance frequencies are more sensitive, however these sensitivities are still not enough for the detection of gravitational waves from astrophysical sources. Unfortunately limitations on the size of such detectors makes it extraordinary difficult to achieve higher sensitivities.

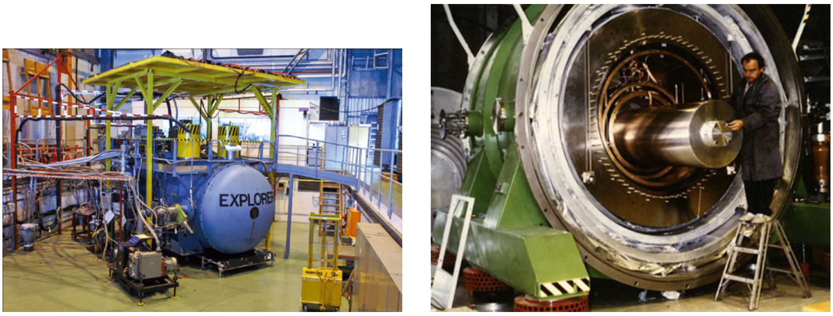

(a) Explorer (b) Nautilus

Figure 8: Two resonant bar detectors.

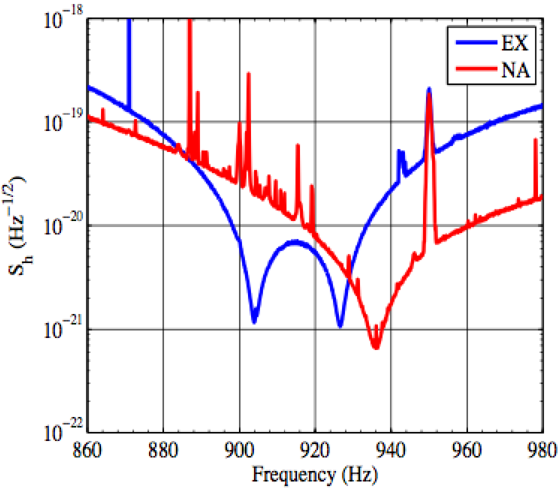

Figure 9: Sensitivities of Explorer and Nautilus detectors. The plot is taken from [14].

LASER INTERFEROMETERS are based on the measurement of the change in the distance between two free-falling test masses (see Eq. 1.23) that occur due to the metric perturbation imposed by a gravitational wave. The distance is measured as a variation of a roundtrip of the laser light that is reflected from mirrors that serve as the test masses [82]. This type of detector is not prone to the limitations in size that the solid detectors have. Therefore laser detectors achieve a better sensitivity due to the large distances between the mirrors. We can consider the measurement of the distance as a measurement of the time that it takes for the light to travel from one mirror to the other and back.

Let us imagine a gravitational wave detector based on the Michelson interferometer (see Fig. 10) with the geometry of the detector such that one arm is parallel to the x-axis and the other one to the y-axis. In the simplified case when the gravitational wave has only "+" polarisation and we consider only the x arm of the interferometer the photon travels from the beam splitter to the mirror and back along its world line

$$ds^2 = -dt^2 + [1 + h_+]dx^2 = 0. \qquad (1.72)$$

We will approach the derivation of the *strain sensitivity* as it is given in [94] by considering the rate of change of the roundtrip time. Namely the time that it takes a photon after it passes the beam splitter (point B on the Fig. 10) to reflect from the mirror in one arm and return back to the place where it interferes with the beam of the perpendicular interferometer arm (BY on the Fig. 10). Therefore we need a very precise measurement of time. The second arm of the interferometer in this case serves as a reference time. The measurement that we make is an interference picture on the photodetector that depends on the phase difference between the two beams of light. The phase difference is directly proportional to the difference in the arm lengths of the detector

$$\delta\phi = \frac{2\pi}{\lambda}\delta l. \qquad (1.73)$$

Let us now derive how changes in the distance in the interferometer's arms depend on the *strain* h of the incoming gravitational wave. If the gravitational wave arrives at an angle θ to the z-axis in the x-z plane the time that the light needs to travel to the distant mirror and back can be written as

$$t'_0 = t_0 + 2L + \frac{1}{2}\cos^2\theta \left[\int_0^L h_+^{xx}(t_0 + (1-\sin\theta)x)dx + \int_0^L h_+^{xx}(t_0 + 2L - (1+\sin\theta)x)dx \right], \tag{1.74}$$

where L is the arm length of the interferometer. In the case there is no gravitational wave, this time will be constant. Therefore to measure the effect of a gravitational wave, we have to measure the rate of variation of the time as a function of the initial time

$$\frac{dt'}{dt_0} = 1 - \frac{1}{2}(1+\sin\theta)h_+^{xx}(t_0) + \sin\theta h_+^{xx}[t_0 + (1-\sin)L] + \frac{1}{2}(1-\sin\theta)h_+^{xx}(t_0 + 2L). \tag{1.75}$$

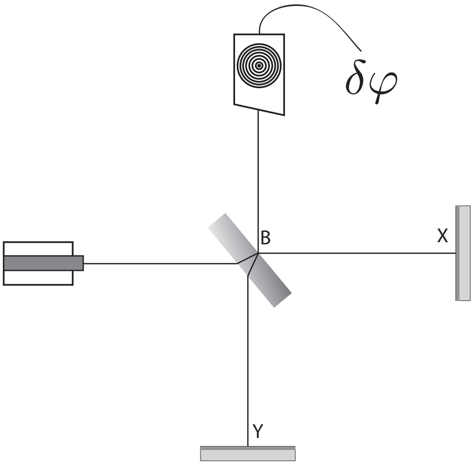

Figure 10: Michelson interferometer. It measures the difference in the lengths of the arms as $\delta\varphi$.

Then following closely [91] for ground-based interferometers that have a small arm length compared to the wavelength of the gravitational waves that are measured, the rate of the travel time change can be Taylor expanded around the small value of L

$$\frac{dt'}{dt_0} = 1 + \sin^2\theta L\dot{h}_+(t). \tag{1.76}$$

It is generalised then to an arbitrary combination of gravitational wave polarisations

$$\mathbf{h}(t) = h_+(t)\mathbf{e}_+ + h_\times(t)\mathbf{e}_\times \tag{1.77}$$

making Eq. 1.76 become

$$\frac{dt'}{dt_0} = 1 + L\hat{e}_x \cdot \dot{\mathbf{h}} \cdot \hat{e}_x. \tag{1.78}$$

The difference between two arms can be integrated over dt yielding

$$\delta t' = L\hat{e}_x \cdot \dot{\mathbf{h}} \cdot \hat{e}_x - L\hat{e}_y \cdot \dot{\mathbf{h}} \cdot \hat{e}_y = \mathbf{d} : \mathbf{h}, \tag{1.79}$$

where the *detector tensor* is defined as $\mathbf{d} = L(\hat{e}_x \otimes \hat{e}_x - \hat{e}_y \otimes \hat{e}_y)$. When rewritten in terms of the travel time instead the Eq. 1.79 becomes

$$\delta l(t) = \frac{1}{2}\mathbf{d} : \mathbf{h}. \tag{1.80}$$

It describes a response of the detector to the gravitational wave for the case of the detector's arm being shorter than the gravitational wave wavelength. Therefore this derivation is only applicable to ground-based detectors. Whereas for space-based detectors such as LISA with its million kilometres arm lengths this approximation is not valid any more. Moreover the orbital motion of the spacecrafts will introduce additional modulation to the frequency, amplitude and phase of the observed gravitational wave [31, 28, 30]. Following these references, the response of the LISA detector is given as

$$\delta l_{ij}(t_i) = \frac{1}{2}\frac{\hat{e}_{ij}(t_i) \otimes \hat{e}_{ij}(t_i)}{1 - \hat{\Omega} \cdot \hat{e}_{ij}(t_i)} : \int_{\xi_i}^{\xi_j} \mathbf{h}(\xi) d\xi, \tag{1.81}$$

where $\hat{\Omega}$ is the direction of the gravitational wave propagation and $\hat{e}_{ij}(t_i) = (\mathbf{x}_j(t_j) - \mathbf{x}_i(t_i))/j_{ij}(t_i)$ is a unit vector. t_i is the time of the photon emission (from spacecraft i to spacecraft j) and t_j is the time of the photon reception. Moreover $\xi(\lambda) = t(\lambda) - \hat{\Omega} \cdot \mathbf{x}(\lambda)$ is a parameterised wave variable with $t(\lambda) = t_i + \lambda$ and $\mathbf{x}(\lambda) = \mathbf{x}_i(t_i) + \lambda\hat{e}_{ij}(t_i)$.

1.2.5 *Sensitivity of laser detectors*

NOISE SOURCES of the detectors that are based on the measurement of the photon travel time will be reviewed here. We have already discussed some of the noise sources when we pointed out that for the measurement of the clock rate change very precise clocks are required, and that this can be achieved, for example, with the Michelson interferometer where the second interferometer arm serves as a "reference clock".

Let us review the other major noise sources. We recall the Eq. 1.80 and write it in the simplified form

$$h = 2\frac{\delta l}{l_0}. \tag{1.82}$$

The noise sources come in this equation in the δl, determining that the detector's frequency range and strain sensitivity are defined not only by the chosen size of the detector but also by the precision of the measurement.

Theoretically it is possible to build a detector that would have its sensitivity limited by the standard quantum limit, which is imposed by the Heisenberg uncertainty principle [34] on the mirror position. However, in reality there are other noises that limit the detector's sensitivity [62]. If we can get rid of the frequency noise the main limiting noises would become shot noise, gravity gradient noise, seismic noise and thermal noise.

- *Seismic noise*
  It is caused by the seismic activity of the Earth and the anthropogenic factor that results in the additional fluctuating Newtonian gravity force on the test masses [61].

- *Gravity gradient noise*
  It is a limiting noise for ground-based detectors that cuts their sensitivities at the low frequency below $f \lesssim 20$ Hz. The frequency dependence of the noise is

  $$x_s \approx \alpha f^{-2} m/\sqrt{Hz}, \tag{1.83}$$

  where α depends on the place where the detector is located and ranges from 10^{-6} to 10^{-9}. It is possible to get improvements for this noise source by using the suspensions and vibration isolation for the test masses, however, it is not possible to get rid of this noise completely in the ground based detectors, making it the reason for building low frequency gravitational wave detectors in space.

- *Shot noise*
  Limiting noise at the high frequencies caused by the fluctuation of the number of photons. It is inversely proportional to the power of the laser light thus can be reduced when the power is increased.

- *Radiation pressure noise*
  Increase in the power of the laser light will increase the radiation pressure noise which is caused by the fluctuation of the number of photons hitting the mirrors.

- *Thermal noise*
  This noise excites the vibration on the test masses with their suspensions. This is the limiting noise at intermediate frequencies.

There are also other noise sources; we will review only the ones that are limiting for the LPF in the later chapters.

POWER SPECTRAL DENSITIES are usually used to describe the sensitivity of gravitational wave detectors. The actual measurement that the detector makes is

$$x(t) = h(t) + n(t), \tag{1.84}$$

where $h(t)$ is the gravitational wave signal and $n(t)$ is the noise of the measurement. The detectors noise level can be characterised by its power spectral density which can be defined as

$$\langle \tilde{n}(f)\tilde{n}^*(f')\rangle = \frac{1}{2}S_n(f)\delta(f-f') \tag{1.85}$$

where $\tilde{n}(f)$ is the frequency transform of the detectors noise (see Appendix A for our definition of the Fourier transform). We do the analysis in the frequency domain because the noise in the time domain is correlated. Whereas, in the frequency domain it is uncorrelated for each frequency bin which incredibly simplifies data analysis. The averaged power spectral density for a detector can be calculated as

$$S_h(f) = \lim_{T\to\infty} \mathrm{E}\left[\frac{1}{T}|\tilde{x}(f)|^2\right]. \tag{1.86}$$

1.2.6 *Ground based laser interferometer detectors*

The ground based laser detectors (see Fig. 11) are trying to observe gravitational waves in the high frequency band from 1 Hz up to several kHz.

In Fig. 12 a comparison of detector sensitivities is presented. It is expressed in terms of analytical approximations to the Amplitude Spectral Density (ASD) of the detectors from [38]. The sensitivity curve for aLIGO is based on [7, 96]. The sensitivity curve for AdV is based on [8, 5]. The sensitivity curve for KAGRA is based on [79, 100].

1.2.7 *Pulsar timing*

The property of pulsars to be very stable clocks can not only help in proving the existence of the gravitational radiation (see Sec. 1.2.2) but can also be used to directly observe gravitational waves. The observation of gravitational waves with *pulsar timing* [92, 36] is based on the idea of measuring the perturbations between Solar System barycentre and distant pulsars over the timescale T. The pulsar's "clock" rate is compared to clocks on Earth and the gravitational wave should then show up as the irregularities in the arrival time of the pulses. The sensitivity of the pulsar timing detector can be expressed in terms of the uncertainties on the arrival of the pulses [19, 22]

$$h \geqslant \epsilon / T, \tag{1.87}$$

where ϵ is the error on the determination of the times of the pulses arrival. The length of the observation time defines also the lower limit of the frequencies that can be detected and the longer the time is the lower frequencies can be observed

$$f \propto 1/T. \tag{1.88}$$

Cosmological models imply that the Universe is filled with a stochastic gravitational wave background at very low frequencies, below 10^{-5} Hz. This background can be observed in the residuals of pulsar timings after modelling the rotation of the pulsar and transmission of the signal [68].

The most stable pulsars that are usually observed for these purposes are millisecond pulsars [35].

COSMIC MICROWAVE BACKGROUND OBSERVATIONS might be able to detect gravitational waves of ultra-low frequencies that have wavelengths comparable to the size of the Universe; such gravitational waves are predicted to be generated during cosmological inflation [117].

Ultra low frequency band

1.3 DETECTION OF GRAVITATIONAL WAVES IN SPACE

To detect gravitational waves at low frequencies, one has to find a way to suppress the gravity gradient noise from the Earth. The only feasible way to do this is by putting the detector into space. The proposed concept for a space-based gravitational wave detector is LISA [102, 42].

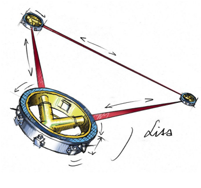

The space detector is based on the same principles as the ground-based, which means that it is a Michelson interferometer that monitors the distance between two free-falling test masses by measuring the rate of the photon travel time from one mirror to the other. However many technical solutions due to the operations of detectors in space are different. The light, for example, is not reflected from mirrors, due to the power loss caused by the divergence of the laser beam over the large distances between spacecrafts (several million kilometres) but instead the local laser is phase-locked to the light from the distance spacecraft. This scheme is analogous to the Doppler tracking used in satellite navigation. The free-fall of the mirrors accommodated within the spacecraft is implemented with *drag-free control*. The technical implementation is described in great detail in [64]. The important technologies that are required for LISA such as laser interferometry in space and test masses free-fall will be demonstrated with the test mission LPF (see Ch. 3).

The three spacecrafts that form LISA will be following the Earth on the heliocentric orbit 20° behind it, with the plane of the LISA triangle inclined 60° with respect to the ecliptic (see Fig. 14).

The design of the detector was optimised for the interesting sources that it can observe [64]. However due to the European Space Agency (ESA) requirement for descoping the *Large scaled* missions there were some changes introduced to the LISA design and the project was renamed to eLISA, reflecting the inherited design in the name *evolved*-LISA. Though the solutions that were found to downscale the mission reduce the instrument's sensitivity, the scientific impact that the gravitational wave observatory would make on understanding the astrophysical sources that it would observe through gravitational radiation and on the theory of gravity that it would be able to investigate in the strong regime remains eminent [52].

The sensitivity of LISA at low frequencies would allow us to study astrophysical black holes, super massive black hole coalescences, extreme mass ratio inspirals, stochastic gravitational wave background, white dwarf binaries and other interesting astrophysical phenomena. These sources, and the knowledge that can be learned from observing them, are described in the *White Paper* [4, 10]. Due to the high SNRs of the signals it would be possible not only to observe gravitational waves but to study astrophysical phenomena that produce them, such as astrophysics and evolution of black holes [9]. In addition, one of the advantages of the LISA frequency range is that there exist known astrophysical continuous wave sources (white dwarf binaries) that would have a high SNR, making them a test of the detectors performance [73, 59].

The main noise sources for both LISA and eLISA would be acceleration noise on the test masses at low frequencies and shot noise of the read-out system [15]. To give the impression of the power spectrum that contribute to the overall sensitivity of the detector, we will give the analytical expression provided in [11] for eLISA

$$S(f) = \frac{20}{3}\frac{4S_{acc}(f) + S_{sn}(f) + S_{omn}(f)}{L^2} \times \left(1 + \left(\frac{f}{0.41c/2L}\right)\right)^2, \quad (1.89)$$

where the requirement on the residual acceleration noise on the test mass is

$$S_{acc} = 1.37 \times 10^{-32}\left(1 + \frac{10^{-4}\text{Hz}}{f}\right)\frac{\text{Hz}}{f}\text{m}^2\text{Hz}^{-1} \quad (1.90)$$

the shot noise is

$$S_{sn} = 5.25 \times 10^{-23}\text{m}^2\text{Hz}^{-1} \quad (1.91)$$

and the other measurement noises contributions are

$$S_{omn} = 6.28 \times 10^{-23}\text{m}^2\text{Hz}^{-1}. \quad (1.92)$$

At the moment, according to the ESA timeline, in the year 2016 the mission project for *the Gravitational Universe* [4] is going to be selected [6] where eLISA was a straw-man mission. Furthermore there are other proposed concepts for the gravitational wave detectors in space, such as DECI-Hertz Interferometer Gravitational wave Observatory (DECIGO) [95].

(a) LIGO Livingston (b) LIGO Hanford

(c) VIRGO (d) GEO

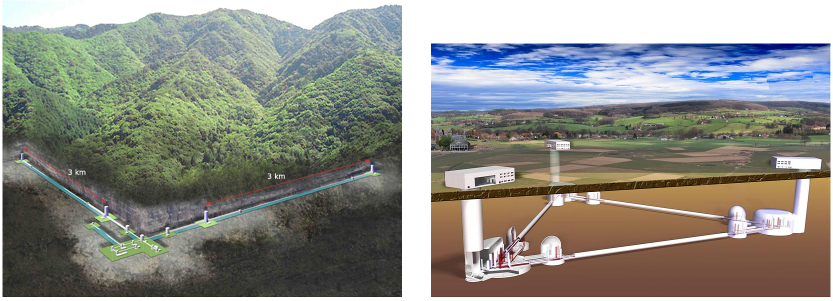

(e) KAGRA (f) ET

Figure 11: Ground based gravitational wave detectors. Current, under construction and planned.

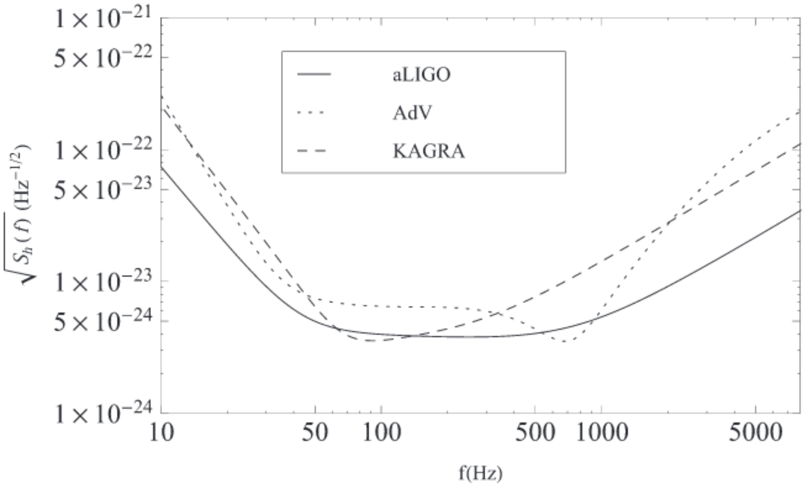

Figure 12: Noise curves for laser interferometer detectors. This Figure is taken from [38].

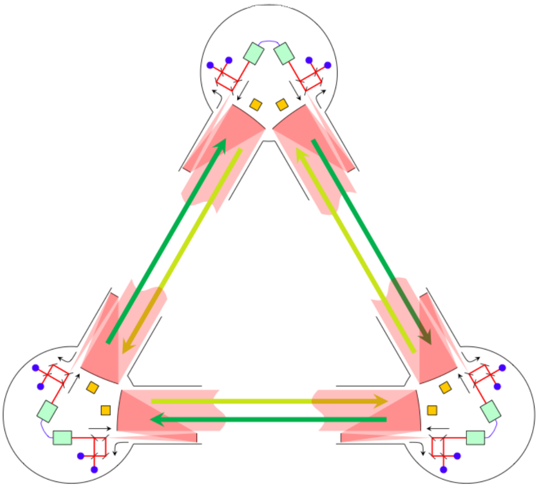

Figure 13: Scheme of the LISA constellation. Figure is taken from [64].

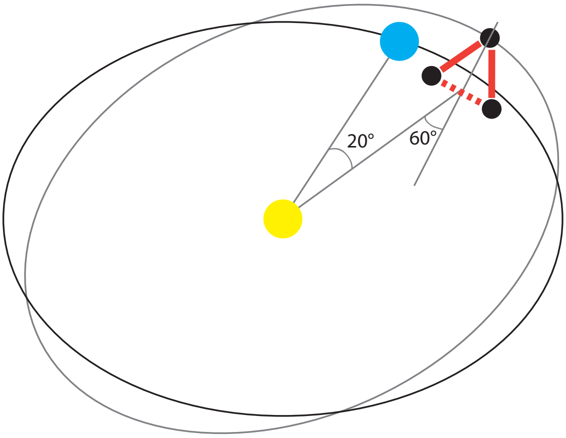

Figure 14: Schematic representation of the LISA orbits.

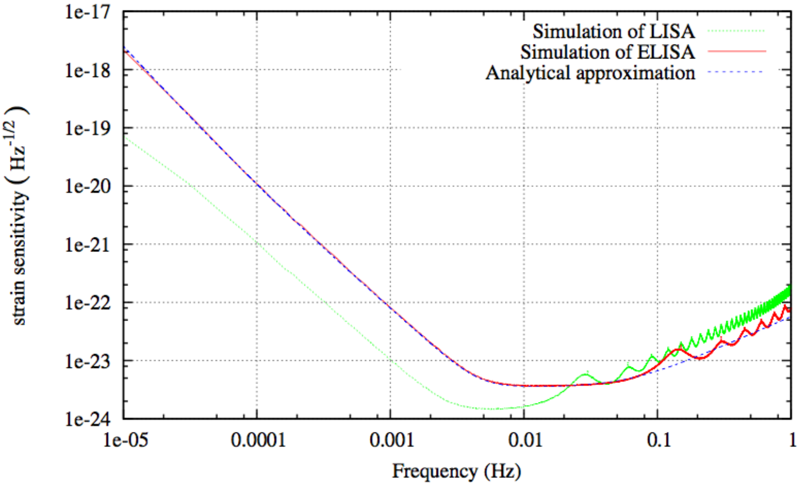

Figure 15: LISA and eLISA sensitivities. This plot is taken from [11].

2

ACTION PRINCIPLE FOR GRAVITY THEORIES

2.1 GENERAL RELATIVITY DERIVED FROM ACTION PRINCIPLE

Since this thesis is dedicated to the experimental way of testing modifications to the theories of gravity, we have to state how these modifications can be introduced. In the previous Chapters 1.1.1 we have discussed Einstein field equations and how gravity is described through the relation between matter and geometry. Now we will formulate GR in terms of the action principle, which was first done by Hilbert [58]. In this approach we will derive the Einstein field equations as Euler-Lagrange equations by varying the appropriately defined Lagrangian.

2.1.1 *Einstein-Hilbert Action*

Let us guess the action based on some set of assumptions. First of all it has to be gauge invariant and we should be able to write it down as an integral of the Lagrangian density over the space-time

$$S = \int \mathcal{L} d^{(4)} V, \tag{2.1}$$

where $g = \det(g_{\alpha\beta})$, $d^{(4)}V = \sqrt{-g} dx^4$ [60] is an invariant 4-volume element and $\mathcal{L}$ is a scalar. The Lagrangian has to be the simplest possible and it has to follow the required symmetries and the field content. This will help us to understand how it can be modified to get the theory that would still be covariant.

The Lagrangian density has two components, the one that describes the matter and the other that describes the metric

$$\mathcal{L} = \mathcal{L}_{\text{gravity}} + \mathcal{L}_{\text{matter}}. \tag{2.2}$$

One can derive the Einstein field equations by taking a functional derivative of the action

$$\frac{\delta S}{\delta g_{\mu\nu}} = \frac{\delta S_{\text{gravity}}}{\delta g_{\mu\nu}} + \frac{\delta S_{\text{matter}}}{\delta g_{\mu\nu}} = 0. \tag{2.3}$$

To proceed, let us write the components of the action separately.

VACUUM FIELD EQUATIONS describe gravity without the presence of matter. The *gravity* part of the Lagrangian density has to be a scalar that solely depends on the metric $g_{\alpha\beta}$

$$S_{\text{gravity}}[g_{\alpha\beta}] = \int \phi(g_{\alpha\beta})\sqrt{-g}d^4x, \tag{2.4}$$

where $\phi(g_{\alpha\beta})$ is some scalar function. The simplest choice that can be formed from the second derivatives of the metric would be a *Ricci scalar* $R = g^{\alpha\beta}R_{\alpha\beta}$. This gives us the expression for the *Einstein-Hilbert action*

$$S_{\text{gravity}}[g_{\alpha\beta}] = S_{\text{EH}}(g_{\alpha\beta}) = \int R\sqrt{-g}d^4x. \tag{2.5}$$

The Lagrangian density for this action can be written in the form

$$\mathcal{L}_{\text{gravity}} = k_1 R + k_2, \tag{2.6}$$

where k_1 and k_2 are some constants. For this Lagrangian

$$\frac{\delta S_{\text{gravity}}}{\delta g_{\mu\nu}} = k_1 \frac{\delta}{\delta g_{\mu\nu}} \int R\sqrt{-g}d^4x + k_2 \frac{\delta}{\delta g_{\mu\nu}} \int \sqrt{-g}d^4x. \tag{2.7}$$

After some calculations it is possible to write [60]

$$\frac{\delta S_{\text{gravity}}}{\delta g_{\mu\nu}} = \left(-k_1 G^{\mu\nu} + \frac{1}{2}k_2 g^{\mu\nu}\right)\sqrt{-g}, \tag{2.8}$$

where $G^{\mu\nu} \equiv R^{\mu\nu} - \frac{1}{2}g^{\mu\nu}R$ is the *Einstein tensor*; for the vacuum solution $G^{\mu\nu} = 0$ is fulfilled with the constant $k_2 = 0$. However, in principle, k_2 stands for the Λ cosmological constant. The value of the constant k_1 will be determined later after we will write the *matter* part of the action.

NON-VACUUM FIELD EQUATIONS take into account the presence of matter. Accordingly we have to define the action for matter [23]

$$S_{\text{matter}}[\phi; g_{\mu\nu}] = \int \mathcal{L}_{\text{matter}}(\phi(x), \partial_\lambda \phi(x), \dots, g_{\mu\nu}(x), \partial_\lambda g_{\mu\nu}(x), \dots) \sqrt{-g} d^4x, \tag{2.9}$$

where ϕ is any type of matter field, such as a scalar, vector or tensor. The metric variation of the matter action [46] is

$$\frac{\delta S_{\text{matter}}}{\delta g_{\mu\nu}} = \int \left[\frac{\partial \mathcal{L}_{\text{matter}}}{\partial g_{\mu\nu}} - \frac{1}{2} \mathcal{L}_{\text{matter}} g^{\mu\nu} \right] \sqrt{-g} d^4x. \tag{2.10}$$

Then if we define a *covariant energy-momentum tensor*

$$T^{\mu\nu} \equiv 2 \left[\frac{\partial \mathcal{L}_{\text{matter}}}{\partial g_{\mu\nu}} - \frac{1}{2} \mathcal{L}_{\text{matter}} g^{\mu\nu} \right], \tag{2.11}$$

we can express the variation of the action through this tensor

$$\frac{\delta S_{\text{matter}}}{\delta g_{\mu\nu}} = -\frac{1}{2} \int T^{\mu\nu} \sqrt{-g} d^4x. \tag{2.12}$$

THE FULL ACTION can be used to write the field equations for GR. The variation of the full action $\delta S / \delta g_{\mu\nu} = 0$ leads to the following expression:

$$-k_1 G^{\mu\nu} + \frac{1}{2} k_2 g^{\mu\nu} + \frac{1}{2} T^{\mu\nu} = 0. \tag{2.13}$$

The factor before the Einstein tensor has to be determined from the Newtonian limit of the resulting equations, which would also influence the choice of the constants k_1 and k_2. Therefore for a sufficient value of this constant we can rewrite

$$16\pi k_1 G^{\mu\nu} - 8\pi k_2 g^{\mu\nu} = 8\pi T^{\mu\nu} \tag{2.14}$$

and in SI units

$$\frac{16\pi G}{c^4} k_1 G^{\mu\nu} - \frac{8\pi G}{c^4} k_2 g^{\mu\nu} = \frac{8\pi G}{c^4} T^{\mu\nu}. \tag{2.15}$$

Now we have to define the constants k_1 and k_2. The coefficient k_1 determines the *coupling constant of gravity*. We can set it to be

$k_1 = c^4/16\pi G$. For example, if it goes to infinity ($k_1 \to \infty$) it means that the gravitational constant $G = 0$, which would imply that gravity is not coupled to the matter, "turned off" in some sense [60]. Whereas, the other constant k_2 is related to the cosmological constant Λ. In the action the Λ-component is not associated with the metric curvature but instead with the volume of the spacetime.

2.2 MODIFICATIONS OF THE ACTION OF GRAVITY

We have seen under which assumptions the equations of GR have been formulated. Moreover we were interested in the derivation of GR field equations in terms of the action variation, since modified gravity theories are commonly represented by introducing changes to the Lagrangians of gravity and matter. In this thesis we are going to address a certain class of modified theories of gravity and will start first with a brief review of how these changes can be made and which theoretical and experimental conditions they have to fulfil. We will review theories with additional fields, theories that modify the way the scalar field enters the action of gravity and theories with more dimensions.

2.2.1 *Validity of gravitational theories*

Many of the modified theories arise as an attempt to explain some astrophysical phenomena that do not find a simple interpretation in the commonly adopted theories, or to incorporate some theoretical concept (such as quantum-gravitational representation of nature or unification of gravity with the other interactions). In general, many choices of Lagrangians both for *gravity* and for *matter* are possible in the case when the theory that it describes is consistent both in the way it is posed and in the observation.

The alternative theories of gravity are expected to be consistent with the experimental limit of the *Equivalence principle*. There are different formulations of the equivalence principle, with different degrees of strength of their conditions that they impose on the theories [115]:

- *Weak equivalence principle* implies the universality of free fall;
- *Einstein equivalence principle* in addition to the universality of the free fall postulates Lorentz invariance and local position invariance;
- *Strong equivalence principle* extends weak equivalence principle to cover gravitating bodies, additionally stating that the outcome of any local test experiment is independent of the velocity of the free falling body and its position.

The degree to which the Equivalence principle is valid can be tested experimentally [114].

EXPERIMENTAL TESTS can be performed for the different regimes of the theories, either by observation of some astrophysical phenomena or by dedicated experiments.

- *Weak field tests*
  For the weak field limit we refer to the Solar System tests. Among these tests are the classical tests of GR: gravitational deflection of light observed near the Sun, anomalous precession of the Mercury's perihelion and gravitational redshift.

  The weak field tests of the validity of the gravitational theories are often interpreted in the framework of the *Parameterised Post-Newtonian Formalism*.

- *Strong field tests*
  Tests of gravity can be performed by observation of the behaviour of matter in the vicinity of compact objects. These tests can be from the observation of gravitational waves or the observations of compact binaries by timing the pulsars or accretion disks that are their components.

We will discuss these tests in both the weak field and the strong field regimes that are within the scope of this thesis in more detail in the Ch. 4.

2.2.2 $f(R)$ *theories of Gravity*

As we have seen in the derivation of the Einstein-Hilbert gravity Lagrangian, the Ricci scalar was taken as the simplest possible suitable choice of the scalar formed from the second derivative of the metric. It is natural therefore that there appeared a class of theories that derive the action from the functional dependency on R or from the higher order derivatives of the metric

$$S = \frac{1}{2k^2}\int f(R)\sqrt{-g}d^4x + S_{\text{matter}}[\Psi; g_{\mu\nu}]. \tag{2.16}$$

A thorough review of such theories is given in [44].

2.2.3 *Theories with additional dimensions – Kaluza-Klein Gravity*

One more way of modifying the Einstein-Hilbert action is to introduce additional dimensions to the metric. This modification of gravity arises from attempts to unify gravitation and electrodynamics [76]. Following [27] let us write the generalised Einstein-Hilbert action for $D = d + 1$ dimensions

$$S[\hat{g}_{AB}]_{\text{gravity}} = \frac{1}{2k^2}\int \hat{R}\sqrt{-\hat{g}}d^DX, \tag{2.17}$$

where $\hat{g}_{AB}$ is the metric, $\hat{R}$ is the Ricci tensor, all in D dimensions and the coordinates are $X^A = (x^\mu, z)$. The idea behind this theory is that gravity is to be considered on a $D = d + 1$ dimensional manifold, where at least one of the spatial dimensions has to be small and compact. To cast the theory into an effective d dimensional theory, we can compactify one of the coordinates z on a circle of radius $L/2\pi$. This can be done by the harmonic expansion of the fields of the theory along the extra dimension. This is the same idea that stands behind compactification of string theory. Following very closely [27] we can write the d-dimensional effective action. We will start with the Fourier expansion of the metric

$$\hat{g}_{AB}(x,z) = \sum_{n} g^{(n)}_{AB}(x) e^{inz/L}. \tag{2.18}$$

The modes that have $n \neq 0$ are associated with the massive fields with the mass $|n|/L$. Since L is very small and the masses are thus very big, they can be neglected at large distances. Thus what we actually do, is compactify and truncate up to the zero mode. The zero modes of the metric $\hat{g}^{(0)}_{\mu\nu}$, $\hat{g}^{(0)}_{\mu z}$ and $\hat{g}^{(0)}_{zz}$ can be redefined in terms of the d-dimensional fields: metric $g_{\mu\nu}$, gauge field A_μ and dilation ϕ. It is possible to choose the following parameterisation

$$\begin{aligned} \hat{g}^{(0)}_{\mu\nu} &= e^{2\alpha\phi} g_{\mu\nu} + e^{2\beta\phi} A_\mu A_\nu \\ \hat{g}^{(0)}_{\mu z} &= e^{2\beta\phi} A_\mu \\ \hat{g}^{(0)}_{zz} &= e^{2\beta\phi}, \end{aligned} \tag{2.19}$$

where $\alpha^2 = 1/2(d-1)(d-2)$ and $\beta = -(d-2)\alpha$. We can now finally write the d-dimensional effective action after integrating out the z component

$$S_{\text{eff}}[g, A, \phi] = \frac{L}{2k^2} \int \left(R - \frac{1}{2}(\nabla\phi)^2 - \frac{1}{4} e^{-2(d-1)\alpha\phi} F^2 \right) \sqrt{-g}\, d^d X, \tag{2.20}$$

where $F^2 = F_{\mu\nu}F^{\mu\nu}$ and $F_{\mu\nu} = \nabla_\mu A_\nu - \nabla_\nu A_\mu$.

2.2.4 *Theories with the additional fields*

These are the theories that in addition to the metric $g_{\mu\nu}$ have extra scalar, vector or tensor fields. In principle, the theories that have been considered so far can also be recast as these kind of theories. Some of these theories can be constructed in a way that they modify the Newtonian dynamics in the non-relativistic limit.

scalar-tensor theories generically have in addition to the metric $g_{\mu\nu}$ a scalar field φ, potential function $V(\varphi)$ and a coupling function $A(\phi)$ [33]. The action can be written in a form

$$S = \frac{1}{2k^2} \int \left[\phi R - \frac{\omega(\phi)}{\phi} g^{\mu\nu} \nabla_\mu \phi \nabla_\nu \phi - \phi^2 V \right] \sqrt{-g} d^4x + S_{\text{matter}}(\Psi, g_{\mu\nu}), \tag{2.21}$$

where *Einstein's* metric was rewritten in terms of the *physical* metric $g_{\mu\nu} \equiv A^2(\varphi) g^*_{\mu\nu}$ which exempts from direct interaction between the scalar and matter fields. In the expression for the action $\phi \equiv A(\varphi)^{-2}$ is a function of a scalar field φ, $\omega(\phi)$ is an arbitrary function defined as $3 + 2\omega(\phi) \equiv \alpha(\varphi)^{-2}$ and $\alpha(\varphi) \equiv d(\ln A(\varphi))/d\varphi$.

These theories are very important for our investigation because they are the most studied ones. For them often the restrictions on the modified theories of gravity are written. They are going to be discussed later in the Ch. 4.

vector-tensor theories – einstein-æther theories have an additional vector field and are known for their violation of Lorentz invariance. For this vector field A^μ is defined to have a preferred time-like direction. The action for these kind of theories can be written in a form

$$S = \int \left[\frac{1}{2k^2} R + \mathcal{L}(g^{\mu\nu}, A^\nu) \right] \sqrt{-g} d^4x + S_{\text{matter}}[\Psi; g^{\mu\nu}], \tag{2.22}$$

where the expression for additional Lagrangian can be found from [65, 66].

tensor-tensor theories – bimetric theories are theories that accommodate two rank-2 tensors [84]. There is a version of bimetric gravity that is interesting in the scope of this thesis, which reduces to MOdified Newtonian Dynamics (MOND) in the non-relativistic limit. An action for a Bimetric MOND [72] can be written as follows

$$S = \frac{1}{2k^2} \int \left[\beta \sqrt{-g} R + \alpha \sqrt{-\tilde{g}} \tilde{R} - 2(g\tilde{g})^{1/4} f(k) l^{-2} \mathcal{M} \right] d^4x - \tilde{S}_{\text{matter}}[\psi; \tilde{g}_{\mu\nu}] - S_{\text{matter}}[\chi; g_{\mu\nu}], \tag{2.23}$$

with the parameters $l \equiv 1/a_0$, $k \equiv (g/\tilde{g})^{-1/4}$, $f(1) = 1$ and $\mathcal{M}$ called the interaction term.

TENSOR-VECTOR-SCALAR THEORIES include scalar and vector fields additionally beyond the metric. The action for tensor-vector-scalar theories is split into the action for different components – metric, vector, scalar and matter [16]

$$S = S_{\tilde{g}} + S_A + S_\phi + S_m. \tag{2.24}$$

All components of this theory will be discussed in more detail in Ch. 4 since the solutions for this theory will be used in the data analysis to produce example signals near the SP.

3

LISA PATHFINDER

3.1 LISA PATHFINDER – TECHNOLOGY DEMONSTRATION FOR LISA

LPF is a compact version of one arm of LISA, designed to verify the ability to place test masses in free fall with the required sensitivity level at a frequency around 1 mHz. It consists of two equal test masses that are accommodated within a drag-free spacecraft. To make the motion of the test masses solely influenced by the curvature of the space-time, the control systems are used to actuate on one of the test masses and on the spacecraft outside of the instruments sensitivity range. The second test mass is controlled by means of the capacitive actuator and the spacecraft is kept drag-free with the help of the µNewton thrusters (see Fig. 16) [83]. The instrument measures the relative position of two free-falling test masses with picometer precision around its maximum sensitivity frequency. The overview of the technological implementations of the spacecraft can be found, for example, in [13].

The system of the two test masses and the spacecraft has 18 degrees of freedom. Three of these are measured by the spacecraft tracking, and the others either by the OMS, Inertial Sensor (IS) or star trackers on board of the LPF.

We are interested in the main scientific measurement, the variation in distance between the test masses, which is equivalent to the measurement of the differential gradient of the gravitational potential. The OMS consists of four Mach-Zender interferometers implemented on its optical bench: one that measures the relative distance between two free-falling test masses, one that measures the position of one of the test masses relative to the Optical Bench (OB) (see Fig. 18) and the other two that are responsible for reduction of the common mode noise and laser frequency noise.

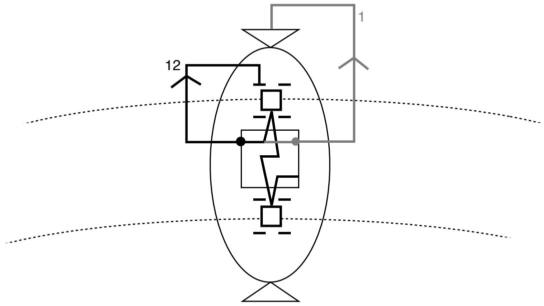

Figure 16: Two test masses following geodesics. Path *1* represents the interferometer readout that measures the position of the first test mass relative to the spacecraft. Path *12* represents the output of the differential interferometer.

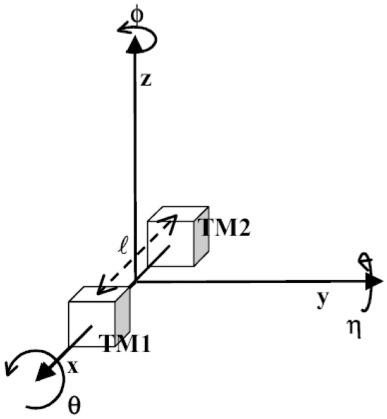

Figure 17: Definition of the LPF coordinates. The system's degrees of freedom that are measured by the interferometer

3.2 MISSION TIMELINE

The spacecraft will be launched from Kourou, French Guiana, by a VEGA launcher. It is composed of two elements: the science spacecraft and the propulsion module. The spacecraft will be transferred to

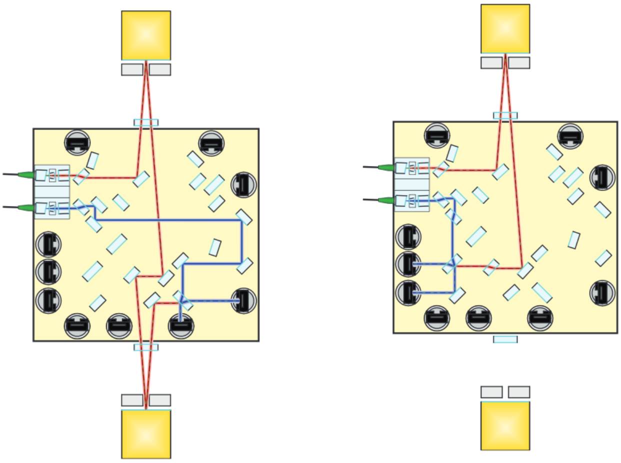

(a) IFO x12 (b) IFO x1

Figure 18: The scheme of the LPF interferometers outlined on the optical bench. The Figures are taken from [48].

the L1 point via a series of apogee raising manoeuvres (see Fig. 20a). The apogee raising manoeuvres will take approximately 2 weeks prior to the transition from Earth to L1, which will take slightly less than three months. At the approach of the spacecraft to L1, the science spacecraft will be separated from the propulsion module. On the operational orbit LPF will go into the calibration and commissioning phase which will be followed by six months (of which 3 months for LISA Technology Package (LTP) and 3 for Disturbance Reduction System (DRS) of experiments performed to verify the on-board technologies and performance of the satellite (see Fig. 19)) [108].

The Lagrange point L1 is a point of dynamically unstable equilibrium between the Sun and the Earth, where the gravitational forces and the centrifugal force cancel out in the non-inertial rotating reference frame. LPF is going to be at L1 because of the stable environment, smooth gravity gradient and the convenience of transport. An example orbit is plotted in Fig. 20b (taken from [83]). While the spacecraft is in that orbit it can maintain a stable environment.

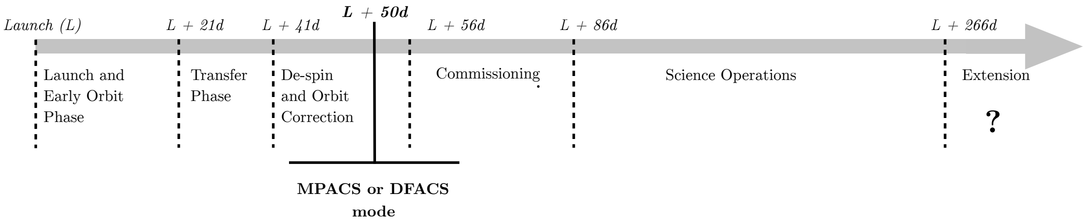
Launch (L)
L + 21d
L + 41d
L + 50d
L + 56d
L + 86d
L + 266d
Launch and Early Orbit Phase
Transfer Phase
De-spin and Orbit Correction
Commissioning
Science Operations
Extension
?
MPACS or DFACS mode

Figure 19: Timeline of the LPF mission.

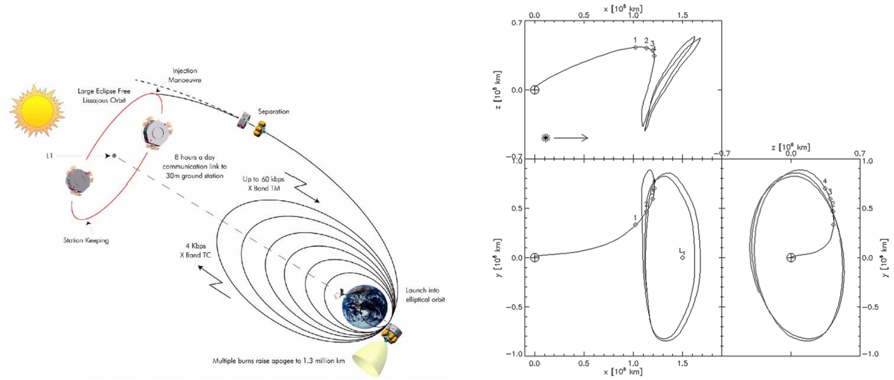
Injection Manoeuvre
Large Eclipse Free Lissajous Orbit
Separation
L1
8 hours a day communication link to 30m ground station
Up to 60 kbps X Band TM
Station Keeping
4 Kbps X Band TC
Launch into elliptical orbit
Multiple burns raise apogee to 1.3 million km
x [10⁶ km]
z [10⁶ km]
y [10⁶ km]
1
2
3
4

(a) The transit of LPF to L1.

(b) Lissajous orbits around L1.

Figure 20: The transit of the spacecraft to L1 and Lissajous orbits around L1.

The in-orbit lifetime of the spacecraft after the separation is 11 months. This thesis is dedicated to what might follow after the main mission time, which would be a mission extension that would imply the transition of the spacecraft to the Sun-Earth saddle point, which will be discussed in Ch. 4.

At present the spacecraft is fully assembled and is already shipped to Kourou.

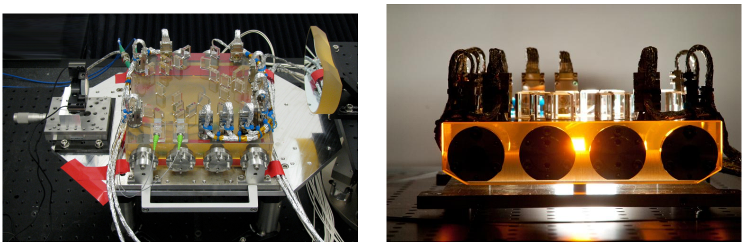

(a) Optical bench. Front view. (b) Oprical bench. Side view.

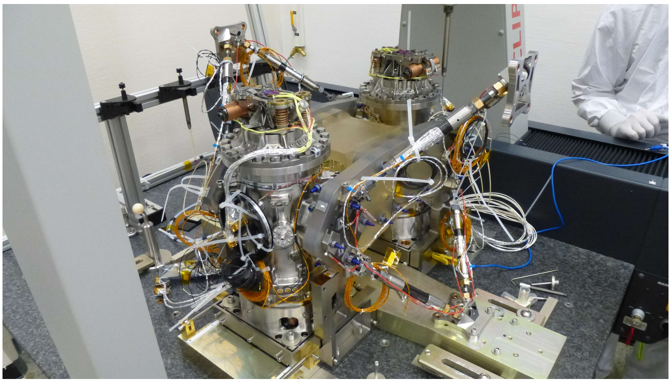

(c) LPF payload.

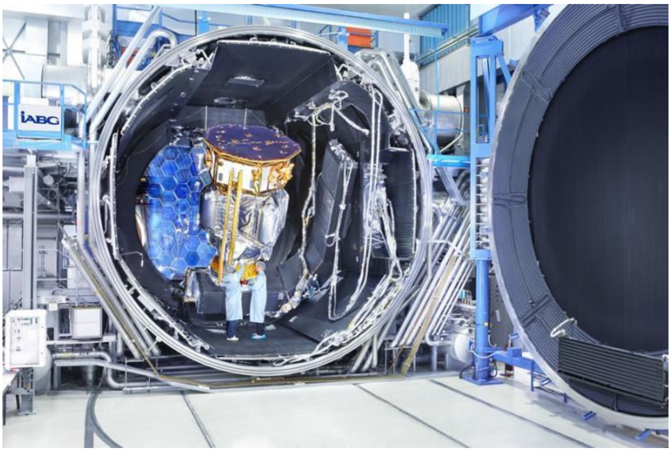

(d) LPF spacecraft in test facility.

Figure 21: LPF flight hardware and preparations for the flight.

Part II

MISSION EXTENSION

4

TESTING GRAVITY IN THE WEAK FIELD LIMIT

4.1 GRAVITY THEORIES WITH AN ADDITIONAL SCALAR FIELD

We have seen the variety of theories that suggest a modifications to gravity in Sec. 2.2 trying to address different theoretical and observational problems. Based on the study of such theories we can conclude that the most common way to introduce the modification to gravity is by means of an additional scalar field.

LPF measures how two test masses follow the curvature of spacetime by monitoring the distance between these masses. Therefore the effect of the additional scalar field can be observed through a coupling of the additional scalar field to the metric. The most general representation [17] in which the additional scalar field can couple to the metric is

$$\tilde{g}_{\mu\nu} = e^{-2\phi}(A(X)g_{\mu\nu} + B(X)\partial_\mu\phi\partial_\nu\phi), \tag{4.1}$$

where $g_{\mu\nu}$ is the gravitational metric, $\tilde{g}_{\mu\nu}$ is the physical metric, ϕ is the scalar field and $X = g^{\mu\nu}\partial_\mu\phi\partial_\nu\phi$ is an invariant. The first term in this equation is known as *conformal* coupling and the second one as the *disformal* coupling. The conformal coupling means that the interval stays invariant under these transformations. The disformal coupling would imply the alteration of the interval. The theories that try to avoid incorporation of dark matter by introduction of the additional scalar field can, in principle, benefit from the disformal coupling. The reason is that it can potentially solve the problem with *gravitational lensing* and account for the required deflection of light by galaxies [18]. However causality requires the factor B to be $B(X)<0$, which means for that kind of coupling of the scalar field to the metric that light will be even less deflected. The problem of the disformal coupling can be overcome with an additional vector field [90] that can be introduced to account for the problem of the gravitational lensing

$$\tilde{g}_{\mu\nu} = u(\phi) g_{\mu\nu} - w(\phi) A_\mu A_\nu, \tag{4.2}$$

where $u(\phi)$ and $w(\phi)$ are arbitrary functions of the scalar field ϕ and $g_{\mu\nu}$ is derived from the Einstein-Hilbert action. The variable A^μ was defined as a non-dynamical vector field and $g^{\mu\nu} A_\mu A_\mu = -1$. This introduces the existence of a preferred reference frame. This coupling now becomes very similar to the TeVeS one. It will be discussed later in 4.3.

4.2 OBJECTIVES FOR MODIFICATIONS OF GRAVITY

There are multiple observational discrepancies from observing the motion of stars and gas in spiral galaxies. According to observations of the surface brightness distribution of galaxies at large distances from the galactic centre the gravitational potential should be like it is produced by the central point mass. However, observed spiral galaxy rotation curves do not match these predictions (see Fig. 22). The observations show that the rotational curves of galaxies stay constant and do not depend on the distance from the galactic centre, as expected in Newtonian gravity [77, 88, 78, 24, 89, 116].

For illustrative purposes we can roughly estimate the radial velocity to be

$$\left.\begin{aligned} \nabla\phi &= G\frac{M}{R^2} \\ \nabla\phi &= \frac{v^2(R)}{R} \end{aligned}\right\} \quad v \propto R^{-1/2}. \tag{4.3}$$

Instead observations show that $v \propto \text{const}$.

There are two proposed solutions to this problem. The first, and commonly accepted one, is that the mass distribution in spiral galaxies does not follow the distribution of visible matter, and instead the visible (flat) galactic disk is embedded in a quasi-spherical potential well produced by dark matter [50].

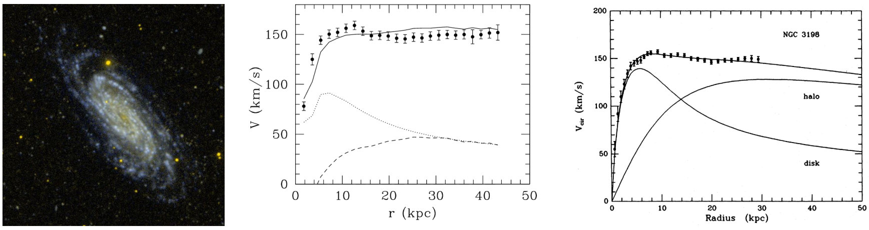

(a) Galaxy NGC 3198 image. The image is taken from the NASA database.

(b) Galaxy NGC 3198 rotational curves. The plot is taken from [54]. The observations of the HI dynamics is plotted along with the various fits. The dotted line is the Newtonian contribution of the stellar disk. The dashed line is the Newtonian contribution of the gaseous disk. The solid line is the MONDian fit.

(c) Galaxy NGC 3198 rotational curves. The plot is taken from [106]. The fit to the observations is done accounting for the bright disk and dark halo.

Figure 22: Galaxy NGC 3198.

Another possible way to explain the observations of rotational curves of spiral galaxies is to modify the equations of gravity. MOND (originally proposed by Milgrom [71]) is a possible heuristic solution to this problem, in contrast to the introduction of hidden mass (i.e., dark matter). At the core of the theory is a characteristic acceleration $a_0 \approx 10^{-10}\text{m/s}^2$ at which a transition occurs, from the regime accurately described by the Newtonian field equation, to one in which the gravitational dynamics is better described by the equation

$$\mu(a/a_0)a = MGr^{-2} = a_N, \tag{4.4}$$

where $\mu(x)$ is an interpolating function that has an arbitrary form but has to satisfy the following conditions

$$\begin{cases} \mu(x) \approx 1 & \text{if} \quad x \gg 1 \\ \mu(x) \approx x & \text{if} \quad x \ll 1. \end{cases} \tag{4.5}$$

Each theory that is suggested as the solution for the discrepancy in the rotational curves of the galaxies has to pass observational astrophysical and cosmological tests such as gravitational lensing, formation of galactic structure. For example, dark matter could explain the dynamics of clusters of galaxies, whereas MOND is not able to explain it without the involvement of at least non-luminous baryonic matter.

4.3 T*e*V*e*S THEORY AS AN EXAMPLE

T*e*V*e*S [16] was the first consistent relativistic theory of gravity reducing to MOND in the non-relativistic limit. It is built upon a non-dynamical gravitational scalar field σ and three dynamical gravitational fields, namely, the Einstein metric tensor $g_{\alpha\beta}$, a timelike 4-vector field $\mathfrak{U}^{\beta}$, and a scalar field ϕ. Accordingly, it was dubbed Tensor-Vector-Scalar theory. The 4-vector is defined in such a way that $g^{\alpha\beta}\mathfrak{U}_{\alpha}\mathfrak{U}_{\beta} = -1$. The physical metric may be obtained from the dynamical fields via the relation

$$\begin{aligned} \tilde{g}_{\alpha\beta} &= e^{-2\phi}(g_{\alpha\beta} + \mathfrak{U}_{\alpha}\mathfrak{U}_{\beta}) - e^{2\phi}\mathfrak{U}_{\alpha}\mathfrak{U}_{\beta} \\ &= e^{-2\phi}g_{\alpha\beta} - 2\mathfrak{U}_{\alpha}\mathfrak{U}_{\beta}\sinh(2\phi), \end{aligned} \tag{4.6}$$

thus stretching Einstein's metric in the direction of $\mathfrak{U}^{\alpha} = g^{\alpha\beta}\mathfrak{U}_{\beta}$.

Within this theory, the total action takes the form

$$S = S_g + S_v + S_s + S_m, \tag{4.7}$$

where S_g is the Einstein-Hilbert action for the metric tensor, S_v is the action governing the timelike vector field

$$S_v = -\frac{K}{32\pi G}\int [g^{\alpha\beta}g^{\mu\nu}\mathfrak{U}_{[\alpha,\mu]}\mathfrak{U}_{[\beta,\nu]} - 2(\lambda/K)(g^{\mu\nu}\mathfrak{U}_{\mu}\mathfrak{U}_{\nu} + 1)](-g)^{1/2}d^4x, \tag{4.8}$$

where λ is a Lagrange multiplier and K is a dimensionless constant. S_s is the action for the dynamical and the non-dynamical scalar fields

$$S_s = -\frac{1}{2}\int [\sigma^2 h^{\alpha\beta}\phi_{,\alpha}\phi_{,\beta} + \frac{1}{2}Gl^{-2}\sigma^4 F(kG\sigma^2)]\sqrt{-g}d^4x, \tag{4.9}$$

where $h^{\alpha\beta} \equiv g^{\alpha\beta} - \mathfrak{U}^{\alpha}\mathfrak{U}^{\beta}$, G is the gravitational constant, k is a dimensionless constant, l is a constant length, and F is a free dimensionless function. Lastly, S_m is the action for the matter fields

$$S_m = \int \mathcal{L}(\tilde{g}_{\mu\nu}, f^{\alpha}, f^{\alpha}_{;\mu}, \ldots)(-\tilde{g})^{1/2} d^4x, \tag{4.10}$$

where $\mathcal{L}$ is the flat space-time Lagrangian for fields f^{α} and $(-\tilde{g})^{1/2} = e^{-2\phi}(-g)^{1/2}$.

The equation for the dynamical gravitational scalar field may be derived by varying S_s with respect to the two scalar fields σ and ϕ, using the equation for the variation of matter part of the action, S_m, for the dynamical scalar field enters there through the physical metric $\tilde{g}^{\mu\nu}$. As a result, one can obtain a relation solely for ϕ expressed in terms of $\tilde{T}_{\alpha\beta}$ [16]

$$\begin{aligned} &[\mu(kl^2 h^{\mu\nu}\phi_{,\mu}\phi_{,\nu})h^{\alpha\beta}\phi_{,\alpha}]_{;\beta} = \\ &kG[g^{\alpha\beta} + (1 + e^{-4\phi})\mathfrak{U}^{\alpha}\mathfrak{U}^{\beta}]\tilde{T}_{\alpha\beta}, \end{aligned} \tag{4.11}$$

where $\tilde{T}_{\alpha\beta}$ is the physical energy-momentum tensor, i.e., built upon the physical metric $\tilde{g}_{\alpha\beta}$, and the function $\mu(y)$ obeys

$$-\mu F(\mu) - \frac{1}{2}\mu^2 \frac{dF(\mu)}{d\mu} = y. \tag{4.12}$$

THE PARAMETERS OF THE THEORY are thus k, K, l and a free function $F(\mu)$. Conditions on these parameters can give different limits of the theories. The GR limit of the theory can be acquired by setting $k \to 0$, $l \propto k^{-3/2}$, $K \propto k$ and μ being any arbitrary function or rather $K \to 0$, k arbitrary and $l \to \infty$, in which case the scalar action S_s will disappear, which means that the scalar field will decouple from the metric. There is no restriction on the choice of the $F(\mu)$ function.

4.4 NON-RELATIVISTIC LIMITS OF TeVeS

As we are going to perform the experiment in the Solar System, we must consider the quasi-static, weak potential, and slow motion limit of TeVeS [16]. We may thus take the metric to be time-independent. Additionally, as we work in a neighbourhood of the Sun – Earth SP, far enough from both bodies, we may set the metric to be flat. Moreover we assume $|\phi| \ll 1$. In the non-relativistic limit $\tilde{g}_{tt} = -(1+\Phi_N+\phi)$, thus the full physical potential that determines the test particle acceleration within TeVeS, $\vec{a} = -\nabla\Phi$, is given by the sum of the Newtonian vector potential Φ_N and the scalar potential ϕ, i.e.,

$$\Phi = \Phi_N + \phi + \mathcal{O}(\Phi_N^2) \,. \tag{4.13}$$

The Newtonian potential is given by the familiar Poisson equation

$$\nabla^2 \Phi_N = 4\pi G \tilde{\rho} \,, \tag{4.14}$$

where $\tilde{\rho}$ is the baryonic mass density, whereas the scalar potential ϕ is determined by the non-linear Poisson equation

$$\nabla \cdot \left[\mu\left(kl^2(\nabla\phi)^2\right)\nabla\phi\right] = kG\tilde{\rho} \,, \tag{4.15}$$

where k is a dimensionless constant and l is a constant length.

The μ function appearing in the last equation is a free function that governs the transition from the Newtonian regime to the MONDian one (see Eq. 4.11). We can reparametrise its dimensionless argument $y \equiv kl^2(\nabla\phi)^2$ in terms of an acceleration parameter

$$a_0 \equiv \frac{(3k)^{1/2}}{4\pi l} \,, \tag{4.16}$$

thus obtaining:

$$y = 3\left(\frac{k}{4\pi}\right)^2 \left(\frac{\nabla\phi}{a_0}\right)^2 \,, \tag{4.17}$$

where the ratio between the MONDian acceleration and the acceleration parameter is now manifest. The asymptotic limits of the μ function must therefore obey the following requirements

$$\begin{cases} \mu(y) \to 1, & \text{for } y \to \infty \\ \mu(y) \approx \sqrt{y/3}, & \text{for } y \ll 1 \end{cases} \,, \tag{4.18}$$

where the first condition leads to the Newtonian regime. The second condition ensures that in the low acceleration regime, i.e. $|\nabla\Phi| \ll a_0$, the MOND modification originally proposed by Milgrom [71] generates a different dynamic, recovering, for example, the one exhibited by rotational curves of galaxies.

4.5 PARAMETERS OF THE THEORIES

All theories that have a conformally coupled scalar field in their action, and that in the non-relativistic limit reduce to theories that predict deviation from Newtonian dynamics have two parameters in the non-relativistic regime

- k – coupling of the additional scalar field,
- a_0 – characteristic acceleration.

Moreover the transition to the regime of low accelerations is described by the interpolating function μ. The various forms of this function were originally acquired from fits to the rotational curves of galaxies.

5

LISA PATHFINDER MEASUREMENT

5.1 NEWTONIAN LIMIT OF GR

In our Solar System we will be working in the weak field limit of gravity. Therefore let us understand the meaning of the curvature tensor in this limit and the form of the geodesic. This then allows us to write the expression for the geodesic deviation in Newtonian space-time, the quantity that will be measured by LPF.

The Newtonian limit of GR is the limit in which gravity is so weak $\Phi \ll 1$ that the velocities are very small compared to the speed of light $v \ll 1$ (in geometrised units). This would also imply that the stress energy-tensor is dominated by the mass-energy density $|T^{ij}|/\rho \ll 1$ and that space-time is asymptotically flat. Moreover we can neglect the time derivatives because velocities are very small $dx^i/d\tau \ll dt/d\tau \approx 1$.

Thus, for the metric in the weak field limit $g_{\mu\nu} = \eta_{\mu\nu} + h_{\mu\nu}$, the conditions $|h_{\mu\nu}| \ll 1$ and $|v^j| = |dx^j/dt| \ll 1$ have to be fulfilled [74].

Let us first consider how gravity influences the motion of a freely falling particle. We write down the geodesic equation and reduce it to the equation for the Newtonian world line

$$\frac{d^2x^i}{dt^2} = \frac{d^2x^i}{d\tau^2} = -\Gamma^i{}_{\alpha\beta}\frac{dx^\alpha}{d\tau}\frac{x^\beta}{d\tau}. \tag{5.1}$$

The right hand side of Eq. 5.1 in the weak field limit becomes [74]

$$-\Gamma^i{}_{00} = -\Gamma_{i00} = \frac{1}{2}h_{00,i} - h_{0i,0} = \frac{1}{2}h_{00,i}. \tag{5.2}$$

If we define

$$-\frac{1}{2}h_{00,i} = \Phi_{,i} \tag{5.3}$$

the geodesic equation becomes

$$\frac{d^2x^i}{dt^2} = -\frac{\partial\Phi}{\partial x^i}. \tag{5.4}$$

Moreover taking into account the boundary conditions

$$\begin{cases} \Phi(r=\infty)=0 \\ h_{\mu\nu}(r=\infty)=0 \end{cases} \tag{5.5}$$

we obtain the following relation

$$h_{00} - 2\Phi, \tag{5.6}$$

which implies that

$$g_{00} = -1 - 2\Phi. \tag{5.7}$$

This is the equation that determines the Newtonian limit of GR. It will also follow that

$$R^i{}_{0j0} = \frac{\partial^2\Phi}{\partial x^i \partial x^j}. \tag{5.8}$$

The interval will then be

$$ds^2 = -(1+2\Phi)dt^2 + (1-2\Phi)(dx^2+dy^2+dz^2). \tag{5.9}$$

Finally, the linearised Einstein's equation

$$\bar{h}_{\mu\nu} = -16\pi T_{\mu\nu} \tag{5.10}$$

becomes the Poisson equation

$$\nabla^2\Phi = 4\pi\rho. \tag{5.11}$$

5.2 MEASUREMENTS OF THE GRAVITY STRESS TENSOR

LPF measures differential displacements between two free falling test masses and is thus sensitive to their differential acceleration [107]. Consider the relative motion of two masses that follow the geodesics of the gravitational field and let the vector ξ denote the separation between the two test masses. The components of this vector may be expressed as $\xi^i = x_1^i - x_2^i$, where $x^i_{\{1,2\}}$ are the coordinates of the two test masses. Working in Cartesian coordinates, the equations of motion for the test masses are

$$\frac{d^2 x_1^i}{dt^2} = -\frac{\partial \phi(x_1, t)}{\partial x^i} \tag{5.12}$$

and

$$\frac{d^2 x_2^i}{dt^2} = -\frac{\partial \phi(\mathbf{x}_2, t)}{\partial x^i} \,. \tag{5.13}$$

The relative acceleration is thus given by

$$\begin{aligned} \frac{d^2 \xi^i}{dt^2} &= \frac{d^2 x_1^i}{dt^2} - \frac{d^2 x_2^i}{dt^2} = \\ &= -\xi^j \frac{\partial^2 \phi}{\partial x^i \partial x^j} + o(\xi^i \xi_i) = -\mathcal{E}^i_j \xi^j + o(\xi^i \xi_i) \,, \end{aligned} \tag{5.14}$$

where summation over repeated indices is implied, the gravitational potential is expanded in terms of the separation vector up to the first order, and $\mathcal{E}_{ij} = \partial^2 \phi / \partial x^i \partial x^j$ is the gravitational tidal field in Cartesian coordinates [74].

LPF has one sensitive axis that is oriented along the line joining the two free falling test masses. By projecting Eq. (5.14) along this axis, one obtains

$$\frac{d^2 \xi_i}{dt^2} \hat{\xi}^i = -\hat{\xi}^i \xi^j \frac{\partial^2 \phi(\vec{x}, t)}{\partial x^i \partial x^j} \,, \tag{5.15}$$

where $\hat{\xi}^i = \xi^i / \|\boldsymbol{\xi}\|$ is the i-th component of the unit vector in the $\boldsymbol{\xi}$ direction. The diagonal components of $\mathcal{E}_{ij}$ contribute to the relative acceleration of the test masses, whereas the remaining components contribute to their tilts. The diagonal components of the stress tensors are larger than the non-diagonal ones, therefore we will consider only the relative acceleration contribution.

5.3 NOISE SOURCES IN THE LISA PATHFINDER MEASUREMENT

LPF measurements are contaminated by the system noise. The main noise contributions come from the measurement subsystems:

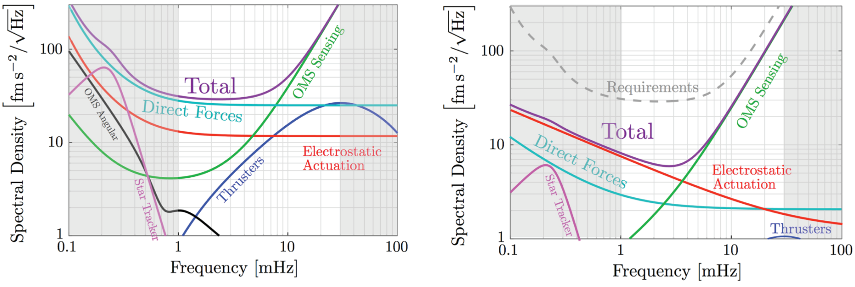

(a) Requirements noise

(b) Current best noise estimate

Figure 23: Contribution to the overall noise from the different noise sources. The figures are taken from [12].

- OMS sensing,
- OMS angular sensing,
- star trackers;

systems utilised in the actuation on the spacecraft:

- thrusters;

and on the test masses:

- electrostatic actuators;

and

- residual forces

that it is not possible to account for with the control systems. The contributions to the total noise can be seen in Fig. 23. The design of LPF is such that the sensitivity of the instrument is expected to be limited by the interferometer readout noise at high frequencies and by force noise on the test masses at low frequencies, which is similar to the limiting noises of the space gravitational wave detector design (see Sec. 1.3). Various tests of the flight hardware, however, show that the real sensitivity of LPF is expected to exceed the design requirements [12], as shown in Fig. 24. The current best estimate noise for LPF is limited by the electrostatic actuation noise on the second test mass at low frequencies.

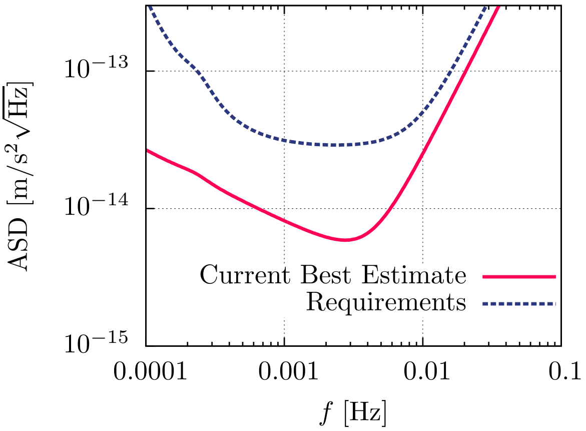

Figure 24: LPF sensitivity. Amplitude spectral densities of the requirements and the current best estimate noise.

Therefore, in the analysis that will follow, we will be using both sensitivities, one that we refer to as *requirements sensitivity* and one that we refer to as *current best noise estimate*.

5.4 EXTENDED MISSION TRAJECTORIES

The spacecraft will be sent to the Sun–Earth SP to measure the low gravity gradient. The location of the SP (see Fig. 25) can be calculated from the condition that the Newtonian gravitational forces from the Sun and the Earth have to cancel out. In general, we have to take into account the influence of other bodies in the Solar System, but an approximate estimate can be computed as follows

$$r_{SP} = \frac{r_{SE}}{\sqrt{\frac{M_S}{M_E}} + 1} \approx 259000\,\text{km}, \tag{5.16}$$

where r_{SE} is the distance from the Sun to the Earth, M_S is the mass of the Sun and M_E is the mass of the Earth.

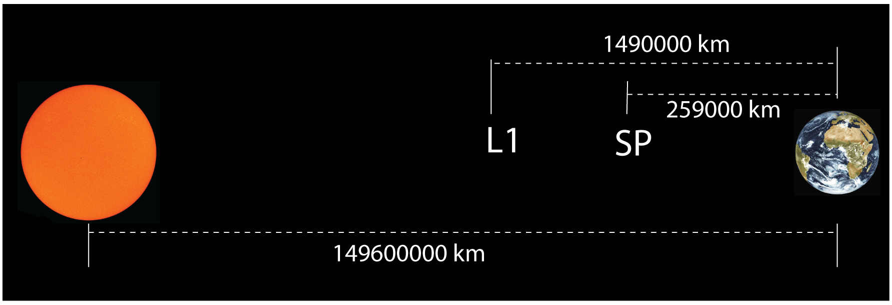

Figure 25: Location of the SP relative to the Sun, Earth and L_1. The Figure is not to scale (Pictures of the Earth and the Sun courtesy of ESA).

The spacecraft will be operating at the Lissajous orbit around the Lagrange point L_1. To leave the Lissajous orbit only a small increase in the velocity has to be applied. This will bring LPF into an unstable orbit and it's trajectory will exponentially diverge from the original Lissajous orbit [41] around L_1. This trajectory will depend on the date of the departure from the orbit, but can be measured very precisely once the spacecraft is following this path.

In the study of the trajectories performed by ASTRIUM [41] is was stated that it should be possible to cross the SP once or twice. The An example of the trajectory from this study is presented in Fig. 26, in which case it will take 250 days for LPF to get from the Lissajous orbit to the first SP flyby and 65 days more for the second flyby.

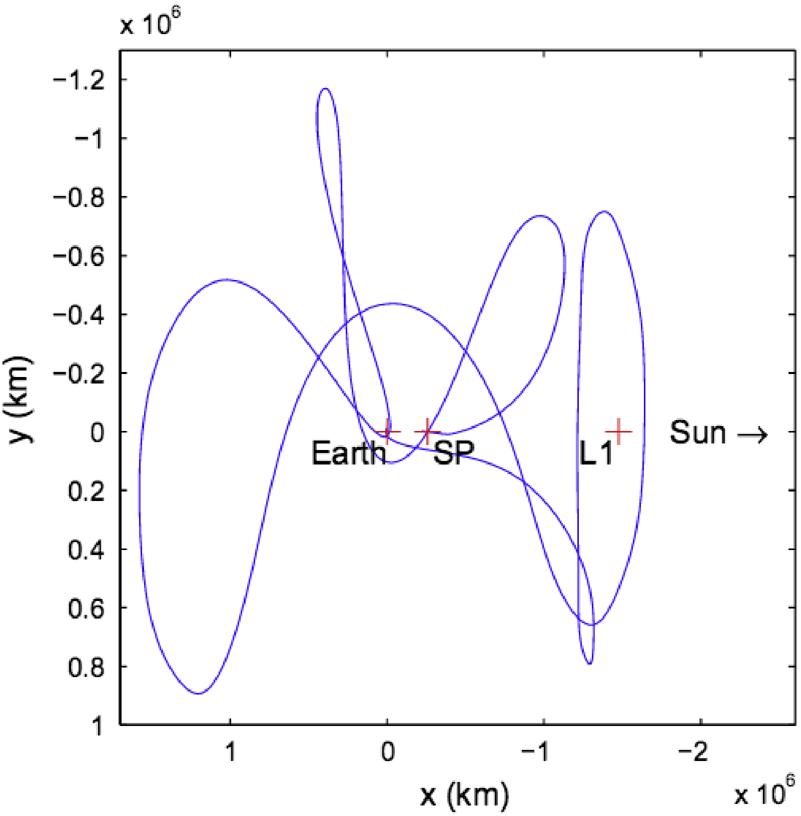

Figure 26: Trajectories of the double SP flyby. The figure is taken from [41].

5.5 SPACECRAFT NAVIGATION AND PARAMETERISATION OF THE TRAJECTORY

5.5.1 *Parameterisation of the trajectory*

In order to parametrise the signals measured by LPF, we must begin by defining a method to determine the spacecraft trajectory uniquely. Let us fix a right-handed Cartesian coordinate system with its origin in the Sun – Earth SP, its x-axis aligned with the line connecting the Earth and the Sun, and its z-axis perpendicular to the ecliptic (see

Fig. 27). The trajectory of LPF in the neighbourhood of the SP can be approximated as a straight line. The direction of the trajectory will be determined by two angles: η, the angle between the z-axis and the direction of the spacecraft velocity, and φ, the angle between the x-axis and the projection of the velocity vector on the ecliptic. The unit vector along the trajectory of the spacecraft in the direction of motion is, therefore

$$(\hat{e}_x, \hat{e}_y, \hat{e}_z) = (\sin\eta\cos\varphi, \sin\eta\sin\varphi, \cos\eta)\,. \tag{5.17}$$

The point of the closest approach of the trajectory to the SP, (ξ_x, ξ_y, ξ_z), determines the impact parameter, i.e., the distance of the fly-by, which is the length of the perpendicular dropped from the SP onto the trajectory. The position of the spacecraft may thus be written as

$$(x, y, z) = (\xi_x, \xi_y, \xi_z) + (\hat{e}_x, \hat{e}_y, \hat{e}_z)r\,, \tag{5.18}$$

where r is the distance from the point of closest approach.

Given the distance to the saddle point, the position of the closest approach becomes redundant. Therefore, to avoid the uncertainty the two angles $\eta_\perp$ and $\varphi_\perp$ that define the position of the perpendicular to the trajectory are introduced

$$\begin{aligned}&(\xi_x, \xi_y, \xi_z) = \\ &\|\boldsymbol{\xi}\|(\sin\eta_\perp\cos\varphi_\perp, \sin\eta_\perp\sin\varphi_\perp, \cos\eta_\perp)\,,\end{aligned} \tag{5.19}$$

where $\|\boldsymbol{\xi}\|$ is the length of the vector (ξ_x, ξ_y, ξ_z). Similarly to the (η, φ) notation previously introduced, $\eta_\perp$ denotes the angle between the perpendicular and the ecliptic, while $\varphi_\perp$ denotes the angle between the x-axis and the projection of the perpendicular on the ecliptic. Notice that the additional condition

$$\begin{aligned}&\sin\eta\sin\eta_\perp(\cos\varphi\cos\varphi_\perp + \sin\varphi\sin\varphi_\perp) + \\ &\cos\eta\cos\eta_\perp = 0\end{aligned} \tag{5.20}$$

holds for the four angles η, φ, $\eta_\perp$, and $\varphi_\perp$ as a consequence of the orthogonality between the satellite trajectory and the line of closest approach. This allows us to further reduce the parameters that

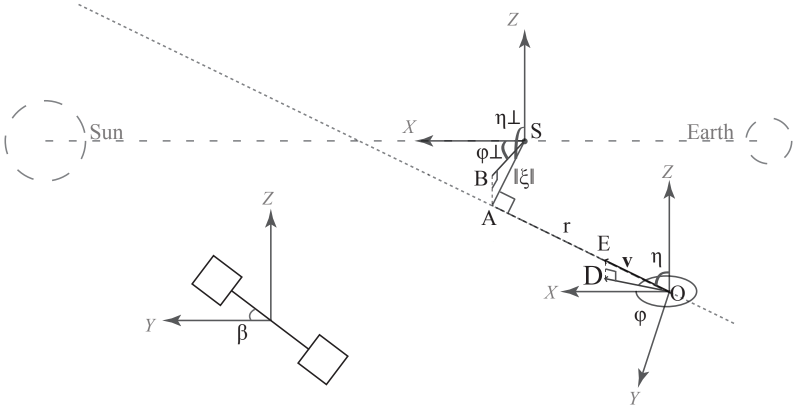

Figure 27: Schematic of the trajectory parameters. The coordinate system has its origin in the SP (S) and the x-axis is parallel to the line joining the Sun and the Earth and pointing in the direction of the Sun. The z-axis is perpendicular to the ecliptic and the spacecraft velocity **v** is aligned with the trajectory. The direction of the trajectory is defined by the two angles η (the angle between the z-axis and **v**) and φ (the angle between x-axis and projection of **v** on the (x, y) plane, shown as the segment OD). The position of the spacecraft along the trajectory is determined by the variable r, the distance to the point A where the perpendicular dropped on the trajectory intersects with it. The length of the perpendicular is given by the parameter $||\xi||$. The position of the perpendicular is given by two angles, $\eta_\perp$ (the angle between the z-axis and the perpendicular) and $\varphi_\perp$ (the angle between the x-axis and the projection of the perpendicular on the (x, y) plane, segment BS).

determine the perpendicular to the trajectory of the satellite in the neighbourhood of the SP down to $\eta_\perp$ and $\mathrm{sign}(\sin\varphi_\perp)$. The latter determines whether $\varphi_\perp \in (0,\pi)$ or $\varphi_\perp \in (\pi,2\pi)$.

The signal measured by LPF can be simulated by sampling the stress tensor along the trajectory with velocity ν and the instrument sampling frequency of 10 Hz. The velocity of the spacecraft and the sampling frequency determine the resolution at which the gravity stress tensor is being sampled.

As a final step, we must define the projection of the stress tensor on the sensitive axis of LPF. The projection is determined by the two angles α and β that the sensitive axis forms with the x-axis and y-axis of the coordinate system, respectively. However, since LPF is held oriented so that its solar panel faces the Sun, and since we are considering a neighbourhood of the Sun – Earth SP, and because the sensitive axis of LPF is parallel to the solar panel, α can be fixed to $\alpha = 90°$. The projection of the stress tensor on the sensitive axis is thus determined only by the angle β, making LPF sensitive to the linear combination of the two diagonal components of the stress tensor:

$$\frac{d^2\xi_i}{dt^2}\hat{\xi}^i = \mathcal{E}_{yy}\sin^2(\beta) + \mathcal{E}_{zz}\cos^2(\beta)\,. \tag{5.21}$$

All in all, the signal can be fully described in terms of the following set of mission parameters:

$$\lambda_0^m = \{\|\xi\|,\eta,\varphi,\eta_\perp,\mathrm{sign}(\sin\varphi_\perp),\|\mathbf{v}\|,\beta\}, \tag{5.22}$$

which are depicted in Fig. 27.

Table 2: This table lists the seven mission parameters also shown graphically in Fig. 27 and provides estimates for their uncertainties. These parameters can be determined from measurements of the spacecraft position which are based on the spacecraft navigation system without involving the LPF optical readout [41, 1]. The uncertainties on the navigation parameter values before the flight, i.e., before the trajectory for the transition from L1 to SP is chosen, and those determined during the flight are provided in columns three and four, respectively. The errors on the angle, α, that defines the orientation of the solar panel are below 1°: as explained in Sec. 5.5.1, we set $\alpha = 90^\circ$ and the error may be neglected within the scope of this thesis. Additionally, the time of closest approach to the SP is not included in the parameter list as it is of the order of several seconds and can be neglected with respect to the signal length.

Parameter	Description	Uncertainty before flight	Uncertainty after flight
$\|\|\xi\|\|$	Fly-by distance	$5\,\mathrm{km}$	$5\,\mathrm{km}$
φ	Trajectory polar angle	30°	$\ll 1^\circ$
η	Trajectory azimuthal angle	30°	$\ll 1^\circ$
$\eta_\perp$	Polar angle of the position of closest approach	uniform	$\|\|\xi\|\|$ -dependent
$\mathrm{sign}(\sin\varphi_\perp)$	Hemisphere of the position of closest approach	$\{-1, 1\}$	–
$\|\|\mathbf{v}\|\|$	Spacecraft velocity	$0.1\,\mathrm{km/s}$	$1\,\mathrm{cm/s}$
β	Orientation of the LPF sensitive axis	$30'$	$30'$

6

SIGNAL TEMPLATES

To extract meaningful information from the data, we develop a data analysis framework for the parameter estimation and model selection. In order to test this framework on artificial data, we must come up with the estimates of the signals that can be possibly observed.

6.1 NUMERICAL SOLUTIONS FOR NON-RELATIVISTIC LIMIT OF TeVeS

In order to test the data analysis framework on artificial data, we must choose a model to produce signal templates. Let us consider the stress tensor predictions obtained within the non-relativistic limit of Bekenstein's TeVeS theory of gravity. This theory embeds the heuristic description of the dynamics of galaxies provided by MOND into a consistent relativistic theory.

As shown by Eqs. (4.15)-(4.17), the signal models will be determined by two parameters k and a_0, and a free function, μ. For the moment, we fix the μ function to the form that was proposed in [16]. In terms of the notation introduced in Eq. (7.1), therefore, $\lambda_0^t = \{k, a_0\}$. The non-linear elliptical differential equation which determines the scalar potential ϕ and hence the tidal stress tensor, Eq. (4.15), can be solved numerically [20, 69, 70] (the code that implements the numerical solution was kindly provided by Imperial College London). While in [16] the μ function definition is

$$y = \frac{3}{4}\frac{\mu^2(\mu-2)^2}{1-\mu}, \tag{6.1}$$

the interpolating function μ in our numerical calculations is fixed via the relation

$$\frac{\hat{\mu}}{\sqrt{1-\hat{\mu}^4}} = \frac{k}{4\pi}\frac{|\nabla\phi|}{a_0}, \tag{6.2}$$

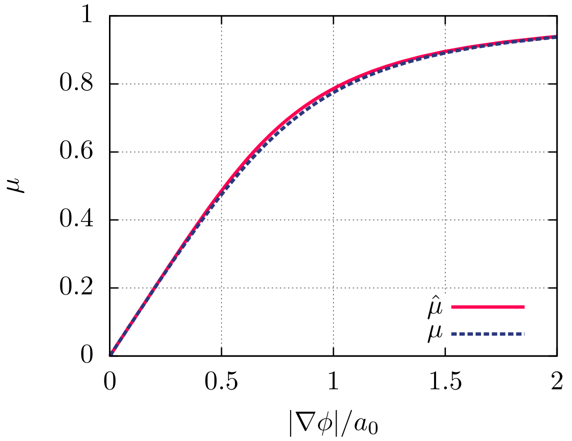

Figure 28: Comparison between the interpolating function used for the numerical calculations and the one originally proposed in [16].

where we used the notation $\hat{\mu}$ to explicitly distinguish this function from the one appearing in Eq. (6.1). As shown in Fig. 28, the two functions are in a good agreement. The advantage of $\hat{\mu}$ is that it may be written out analytically as

$$\hat{\mu} = \sqrt{\frac{-1+\sqrt{1+4x^2}}{2x}}, \tag{6.3}$$

where $x = y/3$. In solving the non-linear Poisson equation numerically, the condition $\mu = \sqrt{x}$ for $x<10^{-5}$ is used [see Eq. (4.18)].

To solve Eq. (4.15) numerically, other than fixing the μ-function, we must prescribe boundary conditions. We use the rescaled Newtonian potential for this purpose. This is readily obtained from Eqs. (4.14)-(4.15) by taking into account that $\mu \to 1$ as $|\nabla\phi|/a_0 \to \infty$ and by applying Gauss's theorem. This yields

$$\nabla\phi = \frac{k}{4\pi}\nabla\Phi_N, \tag{6.4}$$

so that the gradient of the physical potential Φ reduces to the usual Newtonian form with a renormalised gravitational constant given by

$$G_N = \left(1 + \frac{k}{4\pi}\right) G \,. \tag{6.5}$$

6.2 GENERATION OF TEMPLATES

In order to produce signal templates for LPF, as a first step we compute the spatial derivatives of $\nabla\phi$ at each grid point. This provides the nine stress tensor components, namely, $\partial^2\phi/\partial x_i \partial x_j$, where $x_{i,j} = x, y, z$, at each point of the lattice. Once this is done, we must prescribe values for the set of mission parameters listed in Eq. (5.22) and sample the stress tensor along the LPF trajectory [Eq. (5.18)]. The sampling points are determined by the the spacings $\|(\Delta x, \Delta y, \Delta z)\| = \|\mathbf{v}\| \Delta t$, with time step $\Delta t = 1/f_{\text{samp}}$, $f_{\text{samp}} = 10\,\text{Hz}$ being the LPF sampling frequency. The stress tensor components are calculated at each sampling point by performing a trilinear interpolation on a 3-dimensional irregular grid. The interpolation procedure starts with a linear interpolation in the x-axis direction. This is followed by a linear interpolation along the y-axis employing the x-interpolated values. Finally, both the x- and y-interpolated values are used to perform a linear interpolation along the z direction.

Our goals are (1) to see how the signal templates change when varying the two theory parameters k and a_0, and (2) to study their detectability in the noise. The value of the dimensionless coupling constant k should be of the order 10^{-2} to be consistent with cosmological expansion; $k = 0.03$ is chosen in [16]. The characteristic acceleration is usually set to $a_0 \approx 10^{-10}\,\text{m/s}^2$, in accordance with observations of rotational curves of galaxies [43]. We vary both parameters within reasonable ranges around their "original" values, so that $k \in [0; 0.12]$ and $a_0 \in [0; 4 \cdot 10^{-10}]\,\text{m/s}^2$. We cover this two dimensional space of theory parameters with a 9×9 uniform grid (see Fig. 39) and solve Eq. (4.15) numerically in the neighbourhood of the Sun – Earth SP for all choices of (k, a_0).[1] We then fix a set of trajectory parameters

---

[1] Calculations were performed using [2].

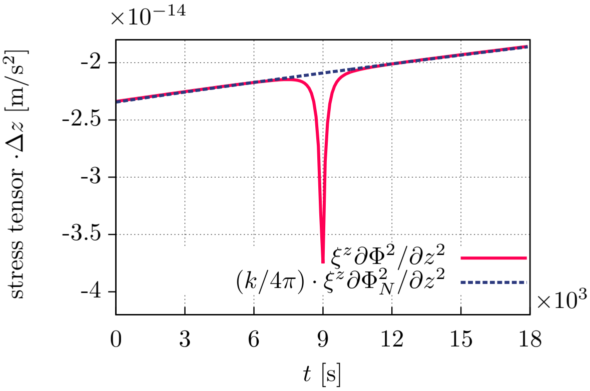

Figure 29: Comparison between a template produced with a numerical calculation and the rescaled Newtonian background analytically estimated using Eq. (6.11). In this example, $k = 0.03$ and $a_0 = 10^{-10}\,\mathrm{m/s^2}$. The $\partial\Phi^2/\partial z^2$ and $\partial\Phi_N^2/\partial z^2$ components of the MONDian and Newtonian stress tensors are plotted. This means that the sensitive axis is parallel to the z-axis of the coordinate system and, therefore, that $\beta = 0$.

and produce LPF signal templates by projecting the computed stress tensor as in Eq. (5.21), at all points in the (k, a_0) parameter space. Additionally, we set $\partial\phi^2/\partial x_i \partial x_j = 0$ along $k = 0$ and $a_0 = 0\ \mathrm{m/s^2}$, as proposed in [16]. In order to obtain signal templates for generic values of k and a_0, we use a bicubic interpolation along both directions. We interpolate the signal templates from the knows solutions for the stress tensor on the two-dimensional parameter space. The interpolation is performed for each sample in the template time series. This is possible since, for a given set of trajectory parameters, a sample in the template time series represents the same position in time and in space for a particular choice of a_0 and k.

As a final remark, we note that in some instances the choice of the theory parameters requires us to extend the templates outside the lattice where the MONDian stress tensor is calculated. As this extension must be performed in a Newtonian limit regime, we exploit the scaling relation between the Newtonian stress tensor (analytically computed, see Sec. 6.3) and the MONDdian one: these are related by a factor $k/4\pi$ [see Eqs. (6.4)-(6.5)], so that projecting the rescaled Newtonian stress tensor along the LPF sensitive axis allows us to extend the MONDian template. An example of this is shown in Fig. 29.

6.3 NEWTONIAN STRESS TENSOR

The expression of the Newtonian potential Φ_N for the Sun – Earth two-body system is

$$\Phi_N = -G\left[M_e\frac{r_0 - d_e}{d_e r_0} + M_s\frac{r_{se} - r_0 - d_s}{d_s(r - r_{se} - r_0)}\right], \tag{6.6}$$

where G is Newton's gravitational constant, M_s (M_e) is the mass of the Sun (Earth), r_{se} is the Sun – Earth separation,

$$r_0 = \frac{r_{se}\sqrt{M_e/M_s}}{\sqrt{M_e/M_s}+1} = \frac{r_{se}}{\sqrt{M_s/M_e}+1} \tag{6.7}$$

is the distance from the Earth to the SP, and d_s (d_e) is the distance from the point where the potential is calculated to the Sun (Earth) respectively, i.e.,

$$d_e = \sqrt{(x_1 + r_0)^2 + x_2^2 + x_3^2}, \tag{6.8}$$

$$d_s = \sqrt{((r_{se} - r_0) - x_1)^2 + x_2^2 + x_3^2}. \tag{6.9}$$

The gradient of the Newtonian potential is therefore

$$\begin{aligned}\frac{\partial\Phi_N}{\partial x_i} &= \frac{GM_e[x_i - r_0 c_i]}{d_e^3}\\ &\quad+\frac{GM_s[x_i - (r_{se} - r_0)c_i]}{d_s^3},\end{aligned} \tag{6.10}$$

where $\hat{\mathbf{e}}_{x_i}(i=1..3)$ is the orthonormal unit vectors set of the reference system and $c_i=\hat{\mathbf{e}}_{x_1}\cdot\hat{\mathbf{e}}_{x_i}$. The Newtonian stress tensor reads

$$\begin{aligned}
\frac{\partial^2\Phi_N}{\partial x_i^2} =& GM_e\left\{\frac{1}{d_e^3}-\frac{3[x_i+r_0c_i]^2}{d_e^5}\right\}\\
&+GM_s\left\{\frac{1}{d_s^3}-\frac{3[x_i-(r_{se}-r_0)c_i]^2}{d_s^5}\right\}\\
\frac{\partial^2\Phi_N}{\partial x_i\partial x_j}\Big|_{i\neq j} =& -\frac{3GM_e}{d_e^5}[x_i+r_0c_i][x_j+r_0c_j]\\
&-\frac{3GM_s}{d_s^5}[x_i-(r_{se}-r_0)c_i][x_j-(r_{se}-r_0)c_j]\,.
\end{aligned}\tag{6.11}$$

Part III

DATA ANALYSIS

7

MISSION PARAMETERS ANALYSIS

We now introduce the approach to the analysis of the data that will be acquired with LPF in the vicinity of the Sun – Earth SP. We describe the model of the data and the derivation of a matched filter which will be designed to study the mission parameters. Thereafter, we develop a Bayesian approach to the analysis of the theory parameters.

7.1 DATA MODEL

The detector noise is modelled as having a frequency dependent spectrum (see Fig. 24), hence it is more natural to carry out the analysis in the frequency domain. We write the measured data as

$$\tilde{x}(f,\lambda_0) = \tilde{h}(f,\lambda_0^m,\lambda_0^t) + \tilde{n}(f)\,, \tag{7.1}$$

where $\tilde{h}(f,\lambda_0^m,\lambda_0^t)$ and $\tilde{n}(f)$ are the Fourier transforms of the signal and the detector noise, respectively. $\vec{\lambda}_0 = (\lambda_0^m,\lambda_0^t)$, where λ_0^m and λ_0^t denote the mission and the theory parameters that govern the signal: the former are listed in Eq. (5.22), whereas the latter will be discussed in the course of the thesis. We model the noise as Gaussian, with zero mean and two-sided noise power spectral density

$$S(f) \approx \langle|\tilde{n}(f)|^2\rangle/\Delta f\,, \tag{7.2}$$

where Δf is the frequency resolution of the data. It is defined as $\Delta f = 1/T = 1/(\Delta t N)$. The noise models we use are defined by the theoretical ASD shown in Fig. 24.

7.2 MISSION PARAMETERS ANALYSIS

In this section we study how the template of the predicted signal changes when varying the mission parameters. This knowledge will validate our choice in studying the theory and the mission parameters independently. This greatly simplifies the study of theories that predict signals that can be measured with LPF. To investigate the mission parameter space we fix the theory parameters to $k = 0.03$ and $a_0 = 10^{-10}\,\mathrm{m/s^2}$, following [16]. In this Section, for the sake of simplicity, we also remove references to the theory parameters from the notation.

We begin by introducing the concept of a linear filter. In terms of our problem, it is a signal template with a certain set of parameters. Its construction is based on the "true" signal that has a fixed set of (mission) parameters λ_0^m. In order to quantitatively assess the influence of parameter variations, we estimate the response of the filter to "data" generated using mission parameters λ_v^m that have an offset $\Delta\lambda^m = \lambda_v^m - \lambda_0^m$ within the range of spacecraft navigation errors reported in Table 3. This table provides the accuracy with which each parameter can be determined from navigation system measurements. We report both the errors on the mission parameters assigned before the flight (*Uncertainty before the flight*) and the precision attainable during the flight by spacecraft navigation system measurements (*Uncertainty after the flight*) [41, 1]. Notice that the low precision on the angles φ and η before the flight follows from the uncertainty on the trajectory which depends on the departure conditions from the Lissajous orbit around L1 [41] and they will be known better once the trajectory is chosen.

The correlation between the data, $\tilde{x}$, and a signal template, $\tilde{q}$, can be calculated as the output of a matched filter via

$$C(\tau, \Delta\lambda^m) = \int_{-\infty}^{\infty} \tilde{x}(f, \lambda_v^m)\tilde{q}^*(f, \lambda_0^m)e^{-2\pi i f\tau}df. \tag{7.3}$$

The signal at the output of the matched filter is the averaged correlation function, for which $\langle\tilde{x}(f,\lambda_v^m)\rangle = \langle\tilde{h}(f,\lambda_v^m)\rangle$ since $\langle\tilde{n}(f)\rangle = 0$. We do not take into account the time delay τ of the signal arrival. We assume that the expected time of the signal arrival, which is the time when the spacecraft has its closest approach to the SP is known. The error on the time of the signal arrival is embedded in the parameter that defines the distance from the SP to the point where the measurement is made. The mean of the correlation function between the data on the output of the instrument and the linear filter $\tilde{q}$ [37] thus reads

$$\hat{C}(\Delta\lambda^m) = \int_{-\infty}^{\infty} \tilde{h}(f,\lambda_v^m)\tilde{q}^*(f,\lambda_0^m)df. \tag{7.4}$$

By setting the linear filter to the "true" template weighted by the noise power spectral density, i.e.,

$$\tilde{q}^*(f,\lambda_0^m) = \frac{\tilde{h}^*(f,\lambda_0^m)}{S(f)}, \tag{7.5}$$

the filter becomes optimal [91]. An optimal matched filter is one that maximises the SNR

$$\rho^2 = \hat{C}(\Delta\lambda^m = 0) = \int_{-\infty}^{\infty} \frac{\tilde{h}(f,\lambda_0^m)\tilde{h}^*(f,\lambda_0^m)}{S(f)}df. \tag{7.6}$$

In the case of optimal filtering, one searches for the filter that best fits the data. This provides a way to estimate the "true" signal template. In our study, fixing the "true" signal template a priori and building a filter upon it allows us to determine the dependency of the magnitude of the matched filter response to a signal with its parameters offset by $\Delta\lambda^m$. This is the measure generally used to quantify the resolution with which we can distinguish one template from another. With this in mind, we rewrite the filter in discrete form

$$c(\Delta\lambda^m) = c(\lambda_0^m,\lambda_v^m) = \sum_{j=1}^{N} \frac{\tilde{h}(f_j,\lambda_v^m)\tilde{h}^*(f_j,\lambda_0^m)}{S(f_j)}\Delta f_j, \tag{7.7}$$

where frequency indices cover the instrument frequency range and $\Delta f_j = f_{j+1} - f_j$, and we consider the ambiguity function built upon the linear filter as follows:

$$\hat{c}(\lambda_0^m,\lambda_v^m) = \frac{c(\lambda_0^m,\lambda_v^m)}{\sqrt{c(\lambda_0^m,\lambda_0^m)c(\lambda_v^m,\lambda_v^m)}}. \tag{7.8}$$

The ambiguity function is normalised to yield unity when the template matches the input signal and less than unity otherwise.

7.2.1 *SNR as a function of mission parameters*

Estimating the SNR as a function of the mission parameters provides insight into the optimal values these should take and allows us to identify any peculiar behaviour of the templates over the parameter space. In turn, if no peculiarities emerge, we assume that this allows us to investigate the behaviour of the signal in the neighbourhood of a single, representative point of our choice in the parameter space and to extrapolate results over the whole range of parameter values. At this location of our choice, we investigate the behaviour of the ambiguity function, as this allows us to assess how much reduction in SNR would be caused by deviations from the nominal mission parameter values.

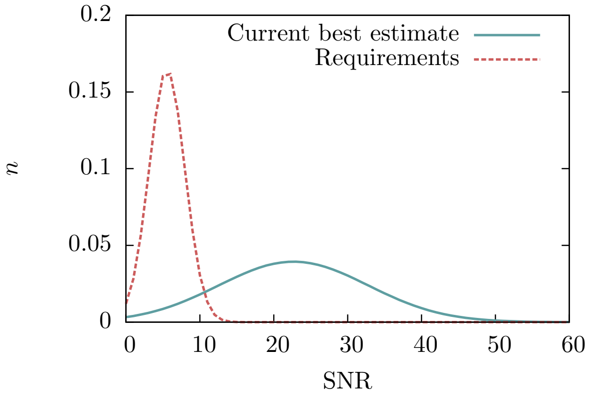

Figure 30: Fraction of trajectories n with SNR value specified on the horizontal axis. The SNR was calculated using 1000 trajectories with randomly varied parameters for both the current best noise estimate and the requirements noise. The parameter values were uniformly sampled over the ranges given in the last column of Table 3. The curves are the Gaussian fits to the discrete distributions that were obtained.

We now compute the expected SNR for the two noise models – current best noise estimate and requirements noise – discussed in Sec. 5.3. The SNR values are calculated using Eq. (7.6) for 1000 differ-

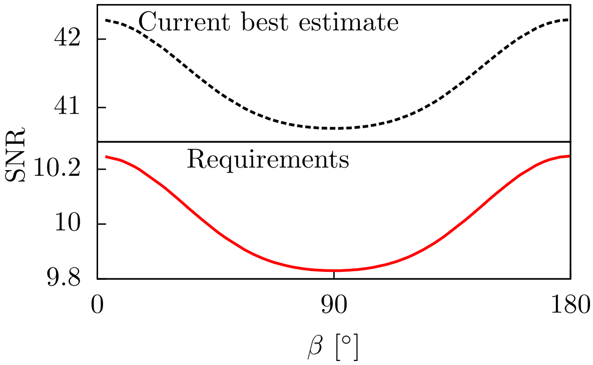

Figure 31: SNR as a function of the orientation angle of the sensitive axis β for the two noise realizations. The remaining mission parameters are fixed according to the set of values given in the last column of Table 3.

ent trajectories each with random parameter values uniformly sampled within the ranges given in the last column of Table 3. As shown in Fig. 30, the Gaussian fits to the histograms of the SNR values peak at $\rho \simeq 23$ and $\rho \simeq 5$ for the current best noise estimate and the requirements estimate, respectively.

When varying the mission parameters sequentially within the predefined ranges, the remaining parameters are fixed to the values given in the last column of Table 3.

The first parameter we vary is the sensitive axis orientation angle β. As seen in Fig. 31, the SNR is not very sensitive to the choice of β and that the optimal value for β for both noise realisations is $\beta = 0°$ or $\beta = 180°$. We will thus fix $\beta = 0°$ for the analysis and for the experiment planning.

The SNR exhibits a smooth behaviour also when the fly-by distance and the spacecraft velocity are varied, as shown in Figs. 32 and 33, respectively. We notice that, as is to be expected, the closer LPF flies to the SP, the higher the SNR is, because tidal stress deviations are

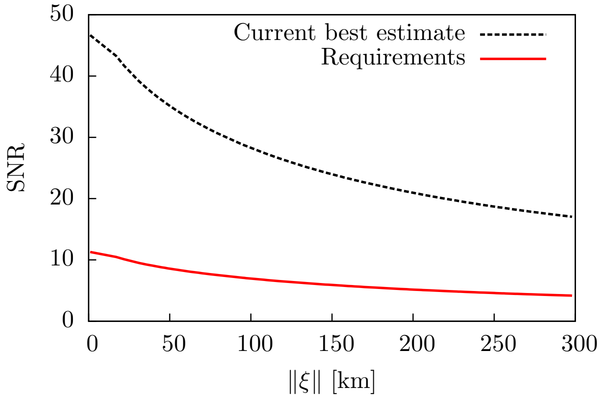

Figure 32: SNR as a function of the distance from the SP $\|\xi\|$ for the two noise realizations. The remaining parameters are fixed according to the set of values given in the last column of Table 3.

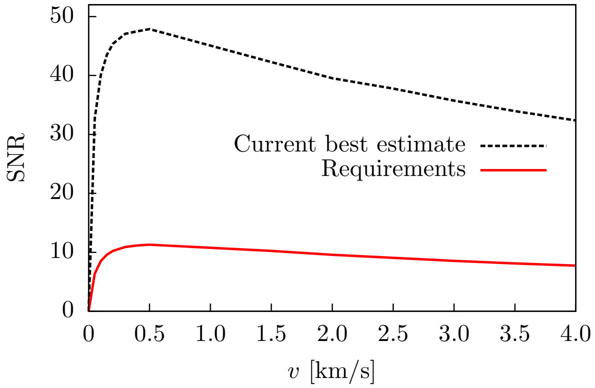

Figure 33: SNR as a function of the spacecraft velocity v for the two noise realizations. The remaining parameters are fixed according to the set of values given in the last column of Table 3. We vary the values of velocity within the larger range than given in the Table 2, i.e. from 0 to 4 km/s, to observe the maximum of SNR.

stronger, whereas the specific value of the spacecraft velocity is not very crucial in the interval reported in Table 3.

Similarly, the SNR is smooth in the φ-η subspace, as shown in Fig. 34. These are the two angles that define the orientation of the spacecraft trajectory. While the SNR is flat in φ, it is maximum for $\eta = \{90°, 270°\}$. In these specific cases we see that more SNR is accumulated if LPF flies within the Ecliptic plane and that the direction of flight within this plane has minimal influence.

As the range of values covered by $\eta_\perp$ depends on the combination of other parameter values via Eq. (5.20), $\eta_\perp$ cannot span the whole interval $[0, 180]°$ for a specific choice of η and φ. Therefore, we do not present SNR estimates as a function of $\eta_\perp$. We note, however, that in the cases we considered the dependence of the SNR on $\eta_\perp$ is weak.

7.2.2 *SNR loss due to mismatched mission parameters*

Having established the dependence of the SNR on the mission parameter space, we may now study the loss of SNR as a function of parameter mismatch within the known navigation uncertainties on the mission parameters. As discussed previously, we fix $\beta = 0°$. At the same time, even though η has its highest SNR estimate for $\eta = 90°$, we will choose it to be $\eta = 70°$ in order to avoid performing our analyses in the best case scenario. Contrary to the alignment of the LPF sensitive axis, the value of η depends on the manoeuvres that are necessary for LPF to leave the Lissajous orbit around the first Lagrangian point. Further, the option of multiple fly-bys [41] implies different estimates for the angle values. We therefore keep this parameter away from its optimal value during our analyses and avoid choosing a trajectory within the Ecliptic plane.

Hereafter, we proceed by taking one dimensional slices through the parameter space, fixing six parameters out of seven to the values listed in the last column of Table 3. The parameters are varied only around their true values, i.e. the values listed in Table 3, that we treat as the parameters of the signal buried in the data. All parameters are varied within intervals that include the spacecraft navigation errors

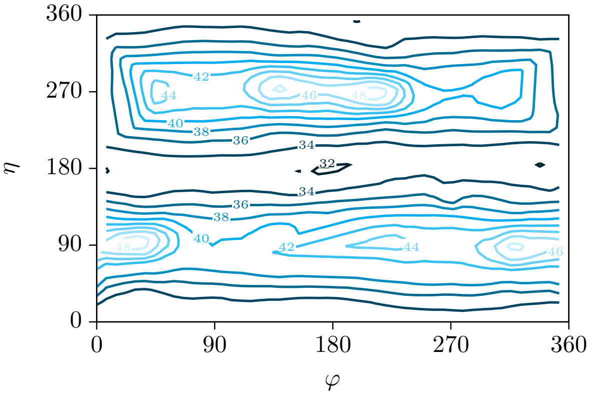

Figure 34: SNR as a function of the angles φ and η that determine the direction of the trajectory. The SNR estimates are plotted for the current best noise estimate. The behaviour for the requirements noise is similar, but with magnitudes in the range [8; 12]. The remaining parameters are fixed to the set of values given in the last column of Table 3.

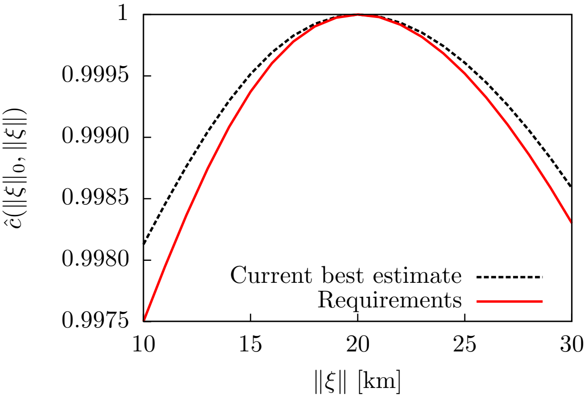

Figure 35: Ambiguity function for the fly-by distance $\|\xi\|$ for the two noise realizations. The true value of the parameter is $\|\xi\|_0 = 20\,\text{km}$. The remaining parameters are fixed according to the set of values given in the last column of Table 3.

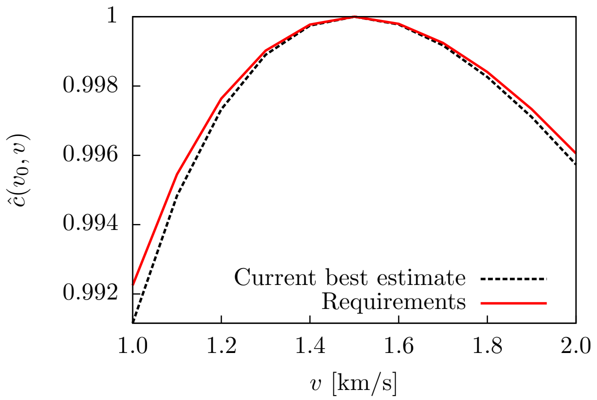

Figure 36: Ambiguity function for the spacecraft velocity v for the two noise realizations. The true value of the parameter is $v_0 = 1.5\,\mathrm{km/s}$. The remaining parameters are fixed according to the set of values given in the last column of Table 3.

listed in Table 3. Similarly to what we did for SNRs, we estimate the ambiguity function [Eq. (7.8)] between templates with varied parameter values and the template with all parameters set to the values listed in Table 3. When the ambiguity function varies very little, we can assume the parameters are essentially exactly known and can be fixed during the analysis of the theory parameters.

Our results for the fly-by distance $\|\xi\|$ are shown in Fig. 35. The true values of the mission parameters follow Table 3, so that $\|\xi\|_0 = 20\,\mathrm{km}$. Templates were evaluated between $\|\xi\| = 10\,\mathrm{km}$ and $\|\xi\| = 30\,\mathrm{km}$ every $1\,\mathrm{km}$ and the ambiguity function $\hat{c}(\|\xi\|_0, \|\xi\|)$ was calculated correspondingly, using both LPF noise curves. We find that if the fly-by distance is mismatched by less then $5\,\mathrm{km}$, i.e., the navigation error before the flight reported in Table 2, the ambiguity function is greater than 0.999. We conclude that we can fix this parameter to $20\,\mathrm{km}$ for future analyses and that it does not need to be estimated from the LPF measurement, but can instead be determined via the spacecraft navigation system.

The same conclusion holds for the spacecraft velocity v. We set $v_0 = 1.5\,\mathrm{km/s}$ to be the true value of the parameter and calculate the

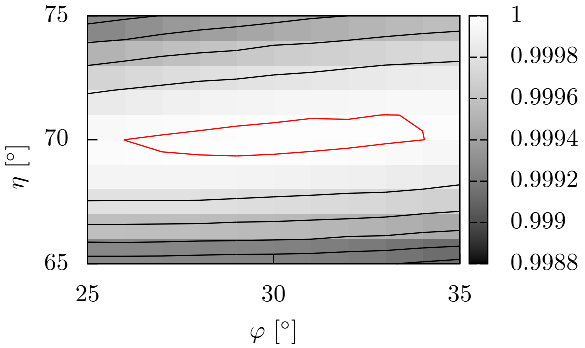

Figure 37: Two-dimensional ambiguity function for the angles φ and η that determine the direction of the spacecraft trajectory. The results are obtained with the current best noise estimate model. The true values of the parameters are set to $\varphi_0 = 30°$ and $\eta_0 = 70°$ and the remaining parameters are fixed according to the set of values given in the last column of Table 3. Both angles are varied with steps of 1°. The closed contour indicates the location of $\hat{c} = 0.99998$.

ambiguity function $\hat{c}(\nu_0,\nu)$ varying ν between 1.0 km/s and 2 km/s and sampling it every 0.1 km/s. The results are shown in Fig. 36 for both LPF noise realizations. As is evident, templates are more sensitive to velocity uncertainties and variations. However, $\hat{c}(\nu_0,\nu)\ 0.998$ for velocity variations within 0.1 km/s, which is the value reported in Table 2 for the uncertainty before the flight. Further, ν may be determined during the flight with an uncertainty of 1 cm/s, so we assume this parameter to be fixed at 1.5 km/s during future analyses.

Next, we vary the angles φ and η that determine the orientation of the spacecraft trajectory. Our results for the ambiguity function are presented in Fig. 37. The true parameter values are $\varphi_0 = 30^\circ$ and $\eta_0 = 70^\circ$. We consider an interval of 10° around both values and sample each interval every 1°. The contours shown in the figure are for the current best noise estimate. The elongation relative to the ecliptic changes the template more than the angle that defines the inclination to the line connecting the Earth and the Sun. Despite the big uncertainty in these parameters before the experiment (see Table 2), the errors on the determination of these parameters during flight are very small ($\ll 1^\circ$), so that they, too, may be assumed to be fixed to their true values for future analyses. The result for the requirements noise is very similar to the result for the current best noise estimate, therefore we will not display them here.

Finally we consider the position of the perpendicular to the trajectory determined by $\mathrm{sign}(\sin\varphi_\perp)$ and $\eta_\perp$. For $\mathrm{sign}(\sin\varphi_\perp)$ there will be no uncertainty after the flight and for the $\eta_\perp$ the results are presented in Fig. 38. They show that the signal templates are not sensitive to variations of this angle.

To summarise, we picked a specific location in the mission and theory parameter space and investigated the behaviour of the ambiguity function. Within the predicted uncertainties on the mission parameters reported in Table 3, the ambiguity function drops minimally compared to the case of exactly matching templates. By assuming that this is the case for all other possible parameters space locations, we make the accurate approximation that the mission parameters can be assumed to be "known" without any loss of generality. They are no longer search parameters, which leaves only the theory parame-

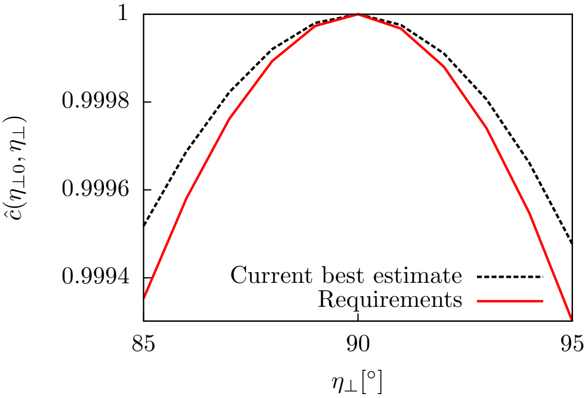

Figure 38: Ambiguity function for the angle $\eta_{\perp}$ which defines the position of the perpendicular to the trajectory for the two noise realizations. The true value of the parameter is $\eta_{\perp} = 90°$ The remaining parameters are fixed according to the set of values given in the last column of Table 3.

ters as unknowns and as the sole target of the search. The analysis of the theory parameters will therefore not require the mission parameters to be measured, nor will it need them to be considered during parameter estimation and model selection. In other words, we can factor the mission parameters out of the theory parameter analyses.

Additionally, we were able to determine the optimal values of β – the LPF sensitive axis orientation – and η – the angle between the spacecraft trajectory and the perpendicular to the Ecliptic plane. In the latter case, we showed that the optical trajectory lies in the plane of the Ecliptic.

Table 3: This table lists the seven mission parameters also shown graphically in Fig. 27 and provides the ranges in which their values are varied to produce Fig. 30, and the values assigned to them during our parameter estimation analyses. The values reported in the last column are those used for the analysis of the theory parameters. These numbers are based on [105] and [41]. While, recent investigations show that it may be possible to realise a trajectory directly through the SP, we have conservatively set $||\xi|| = 20\,\text{km}$.

Parameter	Description	Range	Value	
$\|\|\xi\|\|$	Fly-by distance	$[0;300]\,\text{km}$	$20\,\text{km}$	
φ	Trajectory polar angle	$[0;360]^\circ$	30°	
η	Trajectory azimuthal angle	$[0;180]^\circ$	70°	
$\eta_\perp$	Polar angle of the position of closest approach	uniform	$[0;180]^\circ$	90°
$\text{sign}(\sin\varphi_\perp)$	Hemisphere of the position of closest approach	$\{-1,1\}$	$+1$	
$\|\|\mathbf{v}\|\|$	Spacecraft velocity	$[1;2]\,\text{km/s}$	$1.5\,\text{km/s}$	
β	Orientation of the LPF sensitive axis	$[0;360]^\circ$	0°	

8

DATA ANALYSIS FOR THEORETICAL PARAMETERS

8.1 BAYESIAN APPROACH TO DATA ANALYSIS

8.1.1 *Analysis of the theory parameters*

We now discuss the data analysis framework to study the signal predicted by various alternative theories of gravity. We apply this framework to the case of the TeVeS theory. More specifically, having fixed an interpolating function μ, we study the (k, a_0) parameter space, where k is a dimensionless coupling parameter and a_0 is a characteristic acceleration scale (see Sec. 6.1). We introduce a parameter estimation method based on a Bayesian approach. With this method, information regarding the parameters of the theory can be extracted from the data. Further, we exploit Bayes' theorem to perform model selection, choosing between the hypothesis of having a signal in the noise and the null hypothesis according to which the data consists of noise only.

We discuss how parameter estimation results can be assessed in the case of absence of a signal and how this allows us to rule out portions of the parameter space. Finally, we show how model selection can be applied to realistic data that contains noise artefacts. The results of this study will show whether a glitch in the data can be misinterpreted as a signal and where this will be localised in the parameter space.

8.1.2 *Bayesian parameter estimation*

Following Bayes' theorem, the posterior distribution $p(k, a_0|\{\tilde{x}\}, I)$ of k and a_0 given the data $\{\tilde{x}\}$ and the relevant background information I reads

$$p(k, a_0|\{\tilde{x}\}, I) = \frac{p(\{\tilde{x}\}|k, a_0, I)p(k, a_0|I)}{p(\{\tilde{x}\}|I)}, \tag{8.1}$$

where $p(k, a_0|I)$ is the prior distribution on the parameters, $p(\{\tilde{x}\}|k, a_0, I)$ is the likelihood, and $p(\{\tilde{x}\}|I)$ is the Bayesian evidence, which is the marginal probability density of the data and normalises the posterior. The data model is the sum of a deterministic signal and Gaussian noise and is computed in the frequency domain, as described in Sec. 7.1. We therefore write the likelihood of the Fourier transformed data $\{\tilde{x}\}$ as

$$p(\{\tilde{x}\}|k, a_0, I) = \prod_{j=1}^{N} \frac{1}{\sigma_j^2 2\pi} \exp\left(-\frac{|\tilde{x}_j - \tilde{h}_j(k, a_0)|^2}{2\sigma_j^2}\right). \tag{8.2}$$

In this expression, the variance of the noise σ_j^2 is calculated from the Power Spectral Density (PSD) normalised by the width of the frequency bin, therefore $\sigma_j^2 = S(f_j)\Delta f$ [see Eq. (7.2)]. The noise model is based on the theoretical estimates of the noise for LPF (see Fig. 24). In writing the expression for the likelihood, we assumed that each frequency bin is statistically independent, so that the likelihood can be written as the product of bivariate Gaussian probability density functions.

As a result of the parameter estimation, we shall obtain a joint posterior distribution for parameters k and a_0. However, we are also interested in estimating each parameter separately after performing the experiment. To obtain the posterior distribution of each parameter separately, we marginalise the joint distribution for the two parameters over the other parameter, i.e.

$$p(k|\{\tilde{x}\}, I) = \int_{-\infty}^{\infty} p(k, a_0|\{\tilde{x}\}, I) da_0 \tag{8.3a}$$

$$p(a_0|\{\tilde{x}\}, I) = \int_{-\infty}^{\infty} p(k, a_0|\{\tilde{x}\}, I) dk. \tag{8.3b}$$

These marginal distributions represent our belief in a specific value of one of the two parameters and yield the uncertainty on the parameter estimate following the experiment.

8.1.3 *Prior space*

As a first step to set priors in the (k, a_0) parameter space, we restrict it using the following considerations. We assume that, within some precision, the gradient of the gravitational potential is Newtonian in the non-relativistic limit at a distance from the SP equal to the distance from the SP to the Earth. The gradient of the non-Newtonian potential at this distance depends on the parameters k and a_0 and allows us, therefore, to impose restrictions on the combination of these parameters. Eq. (4.15), which governs the non-Newtonian potential ϕ, depends on the μ-function, which goes to unity in the Newtonian limit, when its argument becomes sufficiently large. Taking the definition[1] of the interpolating function μ given in Eq. (6.1) and expanding it in the $|\nabla\Phi|/a_0 \gg 1$ limit, when $\mu \to 1$, we obtain

$$y = \frac{3}{4(1-\mu)} + \mathcal{O}(1-\mu). \tag{8.4}$$

Eqs. (4.13) and (6.4) can then be used to express the argument of the μ-function as

$$y \equiv kl^2|\nabla\phi|^2 = \frac{k^3 l^2}{16\pi^2}|\nabla\Phi|^2, \tag{8.5}$$

---

[1] We remark that the interpolating function used in the numerical calculations defined in Eq. (6.2) and the one expanded here correspond in the limit we consider, as shown in Fig. 28.

where higher order corrections in $(k/4\pi)$ are neglected. Combing the last two results and expressing l in terms of a_0 as in Eq. (4.16) yield

$$\mu \approx 1 - \frac{64\pi^4}{k^4}\frac{a_0^2}{|\nabla\Phi|^2} + \mathcal{O}\left(y^{-2}\right) . \tag{8.6}$$

If we fix an admissible error ε^2 on deviations of μ from unity, we readily obtain the constraint

$$\frac{a_0}{|\nabla\Phi|} \quad \frac{k^2}{8\pi^2}\varepsilon . \tag{8.7}$$

Imposing this restriction allows one to exclude certain combinations of k and a_0.

In our analysis, we set $\varepsilon = 10^{-5}$, and the resulting, restricted parameter space is shown in Fig. 39. This is a conservative value compared to the latest boundaries imposed on the precision of the additional acceleration allowed in the Solar System [47]. We do not take into account such stringent requirements, as we want to develop and illustrate a data analysis scheme that does not automatically depend on other astronomical restrictions of the parameter space.

We consider a uniform prior parameter distribution (known as flat or constant prior) for the theory parameters. We thus set the prior for a_0 and k to be flat in the admissible portion of the parameter space $\mathcal{P}$, the area of which is given by

$$\mathcal{A} = \int_0^{k^{\min}} a_0'(k)dk + (k^{\max} - k^{\min})(a_0^{\max} - a_0^{\min}), \tag{8.8}$$

where $k^{\min}$ is the value for which $a_0'(k^{\min}) = a_0^{\max} = 4 \cdot 10^{-10}\mathrm{m/s}^2$ and $a_0'(k)$ is a solution of Eq. (8.7). Moreover the values of the modified stress tensor are set at the lower boundary of the parameter space $a_0^{\min} = 0$ to $\partial^2\phi/\partial x^i\partial x^j = 0$. It reflects the GR limit of TeVeS that can be obtained when $l \to \infty$ [16]. Eq. (4.16) shows that this corresponds to $a_0 \to 0$. We therefore have

$$p(k, a_0|I) = \begin{cases} 1/\mathcal{A} & (k, a_0) \in \mathcal{P} \\ 0, & \text{otherwise.} \end{cases} \tag{8.9}$$

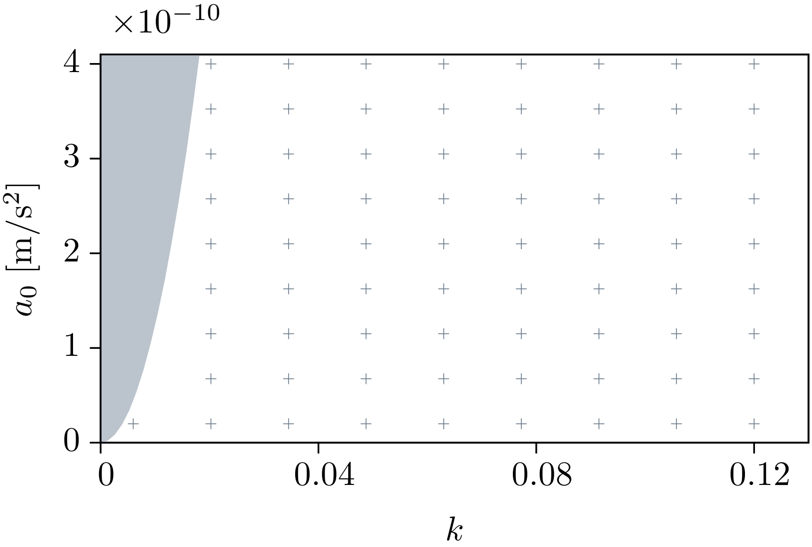

Figure 39: The (k, a_0) parameter space. The shaded area represents the part of the parameter space ruled out by Eq. (8.7). Crosses indicate points where Eq. (4.15) was solved numerically. Signal templates are built upon these solutions and are used, in turn, to determine signal templates at a generic point (k, a_0) via bicubic interpolation.

Flat priors depend on no underlying knowledge on the parameters, except the assumptions made on their span. As discussed in Sec. 6.1, the ranges for the theory parameters is chosen here on the basis of astrophysical observations [43] and in order to keep the theory consistent [16].

As we consider a constant prior, with the exception of the prior boundary constraints, the shape of the posterior parameter distributions will be dictated only by the likelihood function. We note that our Bayesian analysis scheme allows for more physically realistic priors which opens a way for the future analyses of different theoretical models.

8.2 MODEL SELECTION

The framework for model selection that we develop here is based on the Bayesian approach to model selection and can be applied to a variety of hypotheses. For example, we can test a model that assumes the data is the sum of a signal and Gaussian noise, a model that assumes that the data is Gaussian noise only, a model that assumes the data is non-Gaussian noise, a model that assumes Gaussian noise with glitches, and so forth.

Any number of models $\mathcal{M}_i$ can be defined and Bayes' theorem [see Eq. (8.1)] can be directly applied as follows:

$$p(\mathcal{M}_i|\{\tilde{x}\},I) = \frac{p(\{\tilde{x}\}|\mathcal{M}_i,I)p(\mathcal{M}_i|I)}{p(\{\tilde{x}\}|I)}. \tag{8.10}$$

This expression tells us how to determine the posterior probability $p(\mathcal{M}_i|\{\tilde{x}\},I)$, which is the probability of the i-th model $\mathcal{M}_i$ being correct, given the data $\{\tilde{x}\}$ and the background information I. The denominator is the Bayesian evidence, a normalisation term that reads

$$p(\{\tilde{x}\}|I) = \sum_i p(\{\tilde{x}\}|\mathcal{M}_i,I)p(\mathcal{M}_i|I), \tag{8.11}$$

where $p(\{\tilde{x}\}|\mathcal{M}_i,I)$ is the evidence for the model $\mathcal{M}_i$ and $p(\mathcal{M}_i|I)$ is the model prior.

To properly normalise the model posterior distribution, however, one must know all possible models in order to compute Eq. (8.11) and hence Eq. (8.10). This may be avoided by considering the ratio between model posteriors, usually referred to as posterior odds ratio. For two models $\mathcal{M}_1$ and $\mathcal{M}_2$, this reads

$$\frac{p(\mathcal{M}_1|\{\tilde{x}\},I)}{p(\mathcal{M}_2|\{\tilde{x}\},I)} = \frac{p(\{\tilde{x}\}|\mathcal{M}_1,I)}{p(\{\tilde{x}\}|\mathcal{M}_2,I)}\frac{p(\mathcal{M}_1|I)}{p(\mathcal{M}_2|I)}. \tag{8.12}$$

The ratio between the evidences for the two models appearing on the right hand side of the equation is called the Bayes factor. The second fraction on the same side of the equation, $p(\mathcal{M}_1|I)/p(\mathcal{M}_2|I)$, is the prior model odds. The posterior odds ratio represents our confidence in one model against the other, based on the data and the background information I. Here $p(\{\tilde{x}\}|\mathcal{M},I)$ is the likelihood marginalised over its entire parameter space for each model.

As our goal is to quantify our confidence in signal detection, we introduce two ways to model the measured data. The first model, labelled $\mathcal{S}$, describes the data as the sum of a signal and of Gaussian noise, i.e.,

$$\tilde{x}_j = \tilde{h}_j + \tilde{n}_j \,. \tag{8.13}$$

The second model, with label $\mathcal{N}$, describes the data as Gaussian noise only, that is,

$$\tilde{x}_j = \tilde{n}_j \,. \tag{8.14}$$

The ratio between the $\mathcal{S}$ and $\mathcal{N}$ model posteriors is thus

$$\frac{p(\mathcal{S}|\{\tilde{x}\},I)}{p(\mathcal{N}|\{\tilde{x}\},I)} = \frac{p(\{\tilde{x}\}|\mathcal{S},I)}{p(\{\tilde{x}\}|\mathcal{N},I)}\frac{p(\mathcal{S}|I)}{p(\mathcal{N}|I)} \,. \tag{8.15}$$

The Bayesian evidence for a model is calculated by integrating the joint probability density for the data and parameters over the parameter space of the model. In our MOND example, the evidence for the $\mathcal{S}$ model reads

$$\begin{aligned} p(\{\tilde{x}\}|\mathcal{S},I) &= \iint_{\mathcal{P}} p(\{\tilde{x}\},k,a_0|\mathcal{S},I)\,dk\,da_0 \\ &= \iint_{\mathcal{P}} p(\{\tilde{x}\}|k,a_0,\mathcal{S},I)p(k,a_0|\mathcal{S},I)\,dk\,da_0 \,. \end{aligned} \tag{8.16}$$

This is a weighted integral of the likelihood, $p(\{\tilde{x}\}|\lambda_0^t,\mathcal{S},I)$ [see Eq. (8.16)], over the space of unknown parameters, where the weights are set by the prior distributions of the theory parameters, k and a_0 in this case. The Bayesian evidence thus depends on the volume of the parameter space and on the priors. If the dimensionality of the parameter space is large, or if the likelihood and/or the prior are strongly localised, calculating this integral on a uniform grid in the parameter space can become computationally costly. A more practical solution to the problem is to randomly sample the parameter space. To compute the integral in Eq. (8.16), we use the Nested Sampling algorithm, which was specifically designed to calculate evidence values [98].

For the $\mathcal{N}$ model, there are no theory parameters to marginalise over, i.e. the theory parameter space is dimensionless ($\lambda_0^t = \{\emptyset\}$). The evidence is thus simply the noise likelihood

$$p(\{\tilde{x}\}|\mathcal{N}, I) = \prod_{j=1}^{N} \frac{1}{\sigma_j^2 2\pi} \exp\left[-\frac{|\tilde{x}_j|^2}{2\sigma_j^2}\right] . \tag{8.17}$$

The difference between the likelihoods for models $\mathcal{S}$ and $\mathcal{N}$, Eqs. (8.16) and (8.17), respectively, is that in the latter the Gaussian noise is expressed as $\tilde{n}_j = \tilde{x}_j$, while in the former $\tilde{n}_j = \tilde{x}_j - \tilde{h}_j$. The likelihood for model $\mathcal{N}$ can thus be viewed as the likelihood for model $\mathcal{S}$ with the signal amplitude set to zero. For the Bayes factor in Eq. (8.15), the likelihood normalisation terms in cancel out, which simplifies the calculations, leaving only the exponentials of the likelihoods and the normalisation due to the model priors. The ratio of the model priors represents our confidence in one model against the other, based on the background information I. In the absence of preference for either model, this ratio is set to unity, while if background information is available, it can be included in the prior odds ratio accordingly. We will not prioritise a model over the other, so that the posterior odds ratio is simply equal to the Bayes factor.

The posterior odds ratio discussed in this section can be used to decide whether there was a signal buried in the data gathered during the SP fly-by and to provide a quantitative measure of our confidence in a signal detection.

8.3 RESULTS

We test our data analysis method on artificially simulated data to assess the performance of the framework and inspect the various possible outcomes of the experiment. In order to justify the experiment feasibility, it is important to establish what conclusions can be made on the basis of data acquired during the LPF flight. More specifically, we check the implementation of the parameter estimation and model selection, and determine how well the parameters values may be inferred and what choices about the model that best describes the data may be made.

The artificial data is generated following the model defined in Eq. (7.1) and consists of the signal with additive Gaussian noise characterised by the known ASD of the instrument noise (see Fig. 24). The real and imaginary parts of the noise $\tilde{n}(f)$ are treated as statistically independent and drawn from a Gaussian distribution with the given ASD $\sigma(f)$ providing

$$\begin{aligned} p(\tilde{n}(f)) &= p\left(\Re[\tilde{n}(f)]\right) p\left(\Im[\tilde{n}(f)]\right) \\ &= \frac{1}{2\pi\sigma^2(f)} \exp\left(-\frac{\Re[\tilde{n}(f)]^2 + \Im[\tilde{n}(f)]^2}{2\sigma^2(f)}\right). \end{aligned} \tag{8.18}$$

For the signal model $\tilde{h}(\lambda_0^m, \lambda_0^t)$ we chose a particular theoretical prediction for the deviations of the gravity stress tensor from the Newtonian case, as discussed in Sec. 4.4. We test our data analysis setup on TeVeS, but we wish to emphasise that this analysis framework is general and can be used for any signal predictions.

As shown in Sec. 7.2, the mission parameters can be fixed and do not cause the signal to vary significantly once they are defined and measured. Throughout the analysis of the theory parameters, we fix a specific set of mission parameters values in accordance with Table 2. We may thus write

$$\tilde{h}(f_j, \lambda_0^m, \lambda_0^t) = \tilde{h}(f_j, \lambda_0^m, k, a_0) = \tilde{h}(f_j, k, a_0). \tag{8.19}$$

The theory parameter space (k, a_0) was discussed in Sec. 6.1 and SNRs are calculated following Eq. (7.6). Figure 40 shows the SNRs for the chosen LPF trajectory as a function of (k, a_0). For large values of both k and a_0 the SNR reaches values of ~ 100 for the current best estimate and ~ 20 for the requirements noise. This implies that the posterior distributions for the parameter estimates will be reasonably narrow in those high SNR regions. Conversely, we expect signals residing in low SNR areas to have correspondingly broader posterior probabilities.

Given the SNR estimates shown in Fig. 40, we choose a number of representative points in the parameter space with high, intermediate,

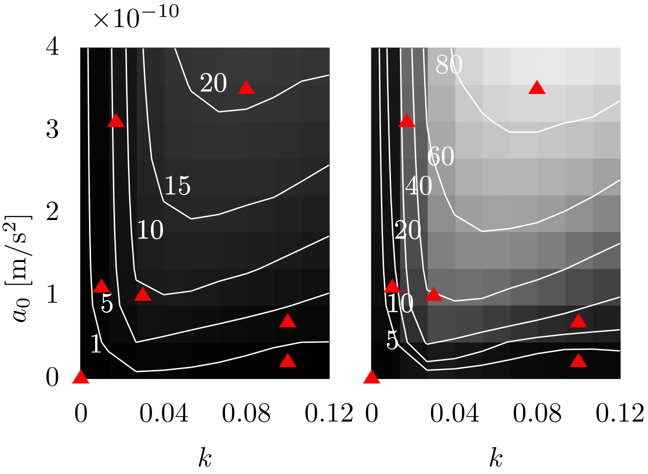

Figure 40: SNR estimates for the current best noise estimate (right panel) and the requirements noise (left panel). The SNRs are calculated at the points in parameter space where the TeVeS numerical calculations were performed. The triangles correspond to the values of k and a_0 for which the signal templates were injected into the data (see Table 4).

Table 4: Values of k and a_0 for which the signal template was injected in the data to probe parameter estimation.

Number	k	a_0 $[10^{-10}\,\mathrm{m/s^2}]$
1	0.030	1.00
2	0.080	3.50
3	0.010	1.10
4	0.017	3.10
5	0.100	0.20
6	0.100	0.68
7	0	0

and low SNR values, and estimate their posterior probabilities. These points are listed in Table 4. We start with *point 1*, for which k and a_0 take their "standard" values [20]. This point belongs to the high SNR region. To test the area with the loudest SNRs, we probe *point 2*. A third interesting region, where the performance of our interpolation must be checked, is the area near the boundary that was imposed on the prior parameter space [Eq. (8.7)]. We chose two points here: *point 3* and *point 4* for low and high SNRs, respectively. Further, we consider two points with low SNRs: *point 5* and *point 6*. They are chosen relatively close to each other in order to assess the area where the transition from the detectable to non-detectable signal might occur. Finally, we consider *point 7*, where the Newtonian limit of the theory lies and we expect to find no signal in the data. For each chosen point on the parameter space we perform 200 simulations with different noise realisations.

8.3.1 *Parameter estimation*

The experiment can give us insight into how well the parameters of the theory can be recovered and constrained from the data. This can be achieved by calculating the posterior probability distribution for the parameters. We have an initial prior assumption for the parameter values, which in our case is a simple uniform distribution over the predefined parameter space discussed in Sec. 6.1. We compute evidence values using a random sampling algorithm (Nested Sampling [97, 99]) as a mean to overcome potential issues due to the sampling of the theory parameter space, or to its high dimensionality. While the theory parameter space is two-dimensional in our example, we must be ready to consider theories with a higher number of parameters. The algorithm and its specific implementation we used, `MultiNest` [45], are designed to efficiently sample a parameter space and to output the samples from the joint posterior parameter distribution and the Bayesian evidence.

To quantitatively summarise the information on the posterior distributions of the parameters, it is natural to use confidence intervals.

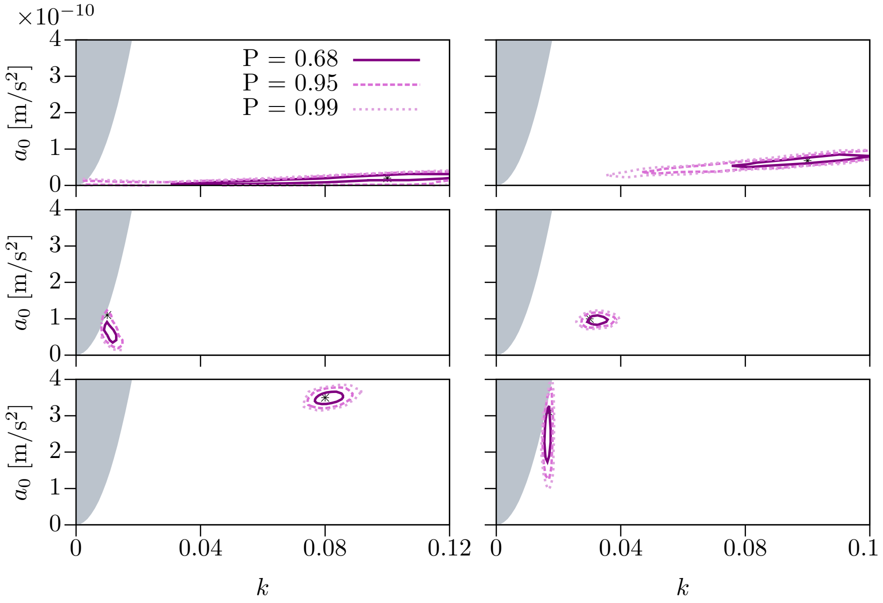

Figure 41: Joint posterior probability distribution for the parameters k and a_0 using the current best estimate noise model. Contours represent lines of constant probability density defining regions that enclose 68%, 95%, and 99% of the probability. The panels represent 6 signal injections at the first 6 points in the parameter space listed in Table 5.

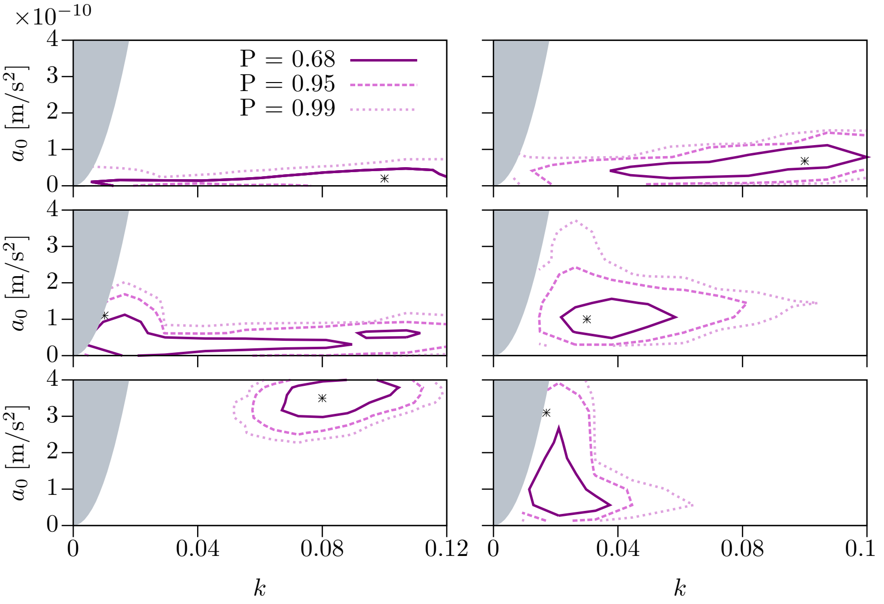

Figure 42: Same as Fig. 41 but for the requirements noise model.

These indicate the parameter range within which the area enclosed under the posterior has a certain probability. This provides an estimate on how confident we are that the value of a parameter falls in that range. As is customary, use the confidence interval values 68%, 95%, and 99%, which correspond to 1σ, 2σ, and 3σ deviations of a parameter from its mean value in the special case of a one dimensional Gaussian distribution. Accordingly, we define the confidence contours

$$\begin{aligned} P((k, a_0) \subset S, I) &= \iint_S p(k, a_0|\{x\}, I)\, dk\, da_0 \\ &= (68\%, 95\%, 99\%), \end{aligned} \tag{8.20}$$

where the space S corresponds to the minimal volume underneath the posterior probability that integrates to predefined probability. The resulting contours also represent lines of constant probability density. Figure 41 shows the contour plots of the joint posterior distributions for the parameters k and a_0 for simulated signals located at selected parameter space positions.

The resulting estimates of the posterior probabilities are shown in Figs. 41 and 42 for the current best estimate noise and for the requirements noise, respectively. The results are presented for a single noise realisation. Estimates for the standard deviation of the posterior distributions of k and a_0 averaged over 200 noise realisations for the current best noise estimate and requirements noise are given in Table 5. For signals with high SNRs (see Fig. 40) the posterior likelihoods are narrow and exhibit low correlation between the two parameters. This means that in the case of signal detection it would be possible to estimate them with relatively small uncertainties. For lower SNRs, however, the error on k is much larger then one on a_0. In some cases the error on k is limited only by the range of the parameter prior. This scenario will be considered in more detail in Sec. 8.3.2, which is dedicated to the case of noise-only simulated data.

Using Eqs. (8.3a)-(8.3b) we determine the marginal distributions for the parameters k and a_0 and their expected values. These marginalised posterior distributions allow us to identify three types of results within our 6 signal simulations. As shown in Figs. 43 and 44,

Table 5: Average values of the standard deviations $\overline{\Delta k}$ and $\overline{\Delta a_0}$ of the one dimensional posteriors of the parameters. The values are given for the 6 points in the (k, a_0) parameter space where the *true* signal injections were made. The averages are determined from 200 different noise realisations (using the current best estimate noise) and posterior estimates truncated by our priors are artificially reduced.

		Current best estimate		Requirements noise	
k	a_0 $[10^{-10}\,\mathrm{m/s^2}]$	$\overline{\Delta k}$	$\overline{\Delta a_0}$ $[10^{-10}\,\mathrm{m/s^2}]$	$\overline{\Delta k}$	$\overline{\Delta a_0}$ $[10^{-10}\,\mathrm{m/s^2}]$
0.030	1.00	0.00203	0.096	0.0121	0.687
0.080	3.50	0.00306	0.117	0.0125	0.352
0.010	1.10	0.00087	0.225	0.0295	0.515
0.017	3.10	0.00066	0.422	0.0066	0.907
0.100	0.20	0.03053	0.084	0.0345	0.173
0.100	0.68	0.01838	0.137	0.0295	0.268

for the first type of result the joint posterior distribution is narrow and well localised, especially for the current best estimate noise. In this scenario the marginal distributions of both k and a_0 can be estimated relatively well. Results for the second case can be found in Figs. 45 and 46. This time the posterior is near the boundary of the prior established in Sec. 6.1. The uncertainty on a_0 is much broader than the one on k. Finally, Figs. 47 and 48 show the third kind of result: the marginalised distribution for k is very broad and is determined by the range that was imposed on it as a prior. In this low SNR regime, it will be hard to make estimates for k.

8.3.2 *The no signal injection case*

No deviations from Newtonian gravity potential have been observed so far in the Solar System. Hence, this is a particularly important case for our analysis and corresponds to a dataset containing no signal. We consider this case as a likely outcome of the experiment and wish to assess the impact that a measurement of data with no signal would have on the theory parameter space, i.e. which observation-based restrictions can be placed on the (k, a_0) space.

In Figs. 47 and 48, we already saw the shape of the posterior distribution in the case of low SNRs. We would expect to have somewhat similar results for the case of a noise-only data model, i.e. when we set $\tilde{h}(f_j, \lambda_0^m, \lambda_0^t) = 0$ in Eq. (7.1). On the basis of the theory proposed in [16], we place the Newtonian limit of the theory at $a_0 = 0$, thus setting the gravity stress tensor to be equal to the Newtonian stress tensor for all templates on the k-axis.

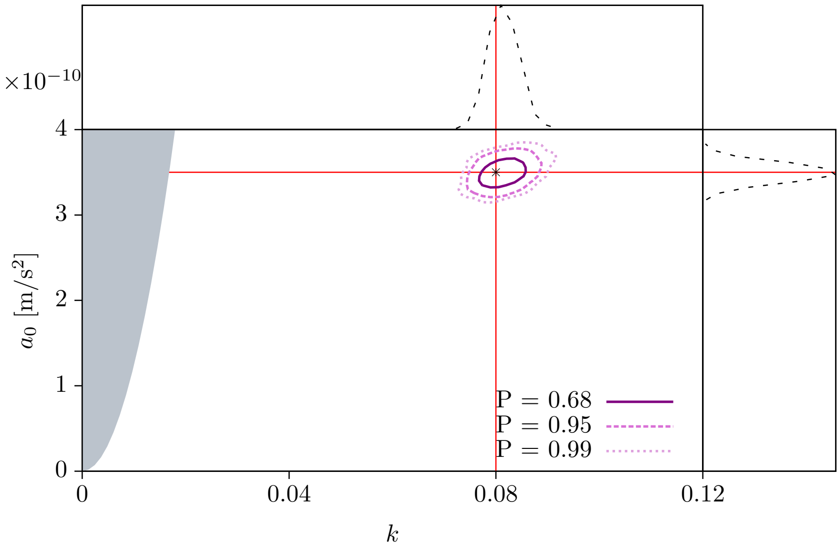

Figure 43: Posterior probability distributions and marginalised posterior distributions for the current best noise estimate for the parameters of the injected signal at $k = 0.08$ and $a_0 = 3.5 \cdot 10^{-10} \text{m/s}^2$. The red lines indicate the true values at which the simulated signal was injected.

We perform 200 simulations, each with a different noise realisation, for both the current best estimate and requirements noise models. We determine 68%, 95%, and 99% confidence interval for both of them. To visualise the restriction on the parameter space that follows, we chose a representative noise realisation. The results in Figs. 49 and 50 show uncertainty on the determination of the parameter k, meaning that a null measurement would not help us constrain k at all, whereas a_0 would be tightly bounded. The average error on the marginalised posterior distribution of a_0 for the current best noise estimate is $\overline{\Delta a_0} = 0.055 \cdot 10^{-10}\,\mathrm{m/s^2}$, while for the requirements noise it is $\overline{\Delta a_0} = 0.154 \cdot 10^{-10}\,\mathrm{m/s^2}$

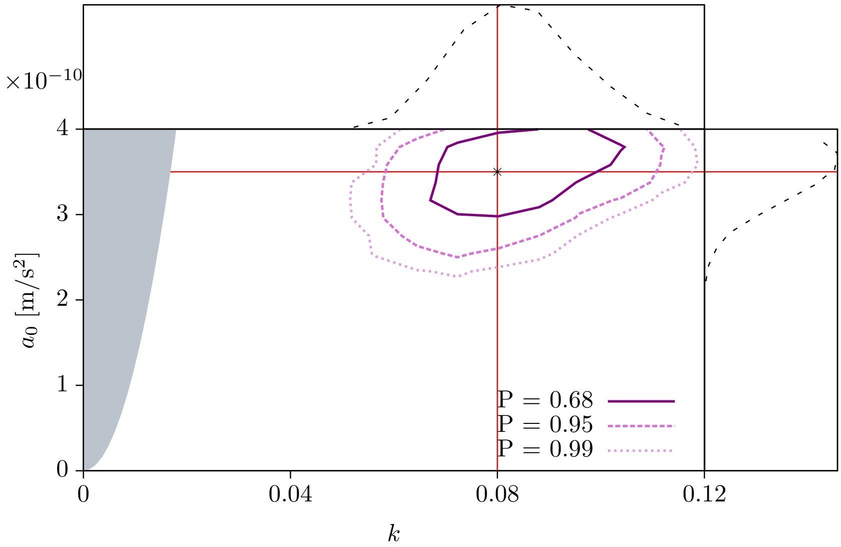

Figure 44: Posterior probability and marginalised posterior distributions for requirements noise for the parameters of the injected signal at $k = 0.08$ and $a_0 = 3.5 \cdot 10^{-10}\mathrm{m/s^2}$. The red lines indicate the true values at which the simulated signal was injected.

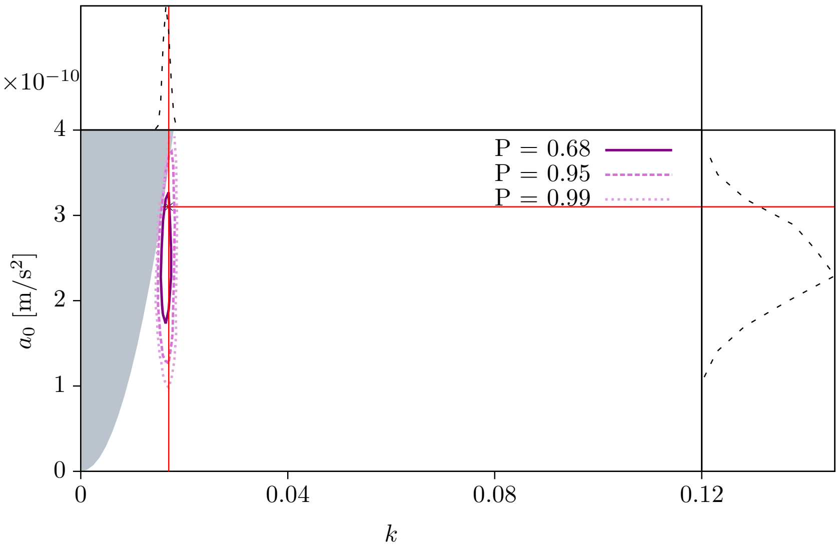

Figure 45: Posterior probability distributions and marginalised posterior distributions for the current best noise estimate for the parameters of the injected signal $k = 0.017$ and $a_0 = 3.1 \cdot 10^{-10}$m/s. The red lines indicate the true values at which the simulated signal was injected.

8.3.3 *Model Selection*

We now follow Eq. (8.15) and compute the Bayes factor[2] between our two candidate models $\mathcal{S}$ and $\mathcal{N}$ using the signals calculated for the sets of parameters listed in Table 4. This gives a measure of the signal detectability in noise, depending on the combination of the theory parameters $\boldsymbol{\lambda}_0^t = \{k, a_0\}$, allowing us to quantify the confidence in one model relative to the other on the basis of the outcome of the experiment. As discussed in Sec. 8.2, the $\mathcal{S}$ hypothesis assumes that the data is the sum of noise and a signal that depends on k and a_0, while the $\mathcal{N}$ hypothesis assumes it to be noise-only and to have no parameter

---

[2] We remind the reader that we set the prior model odds to unity.

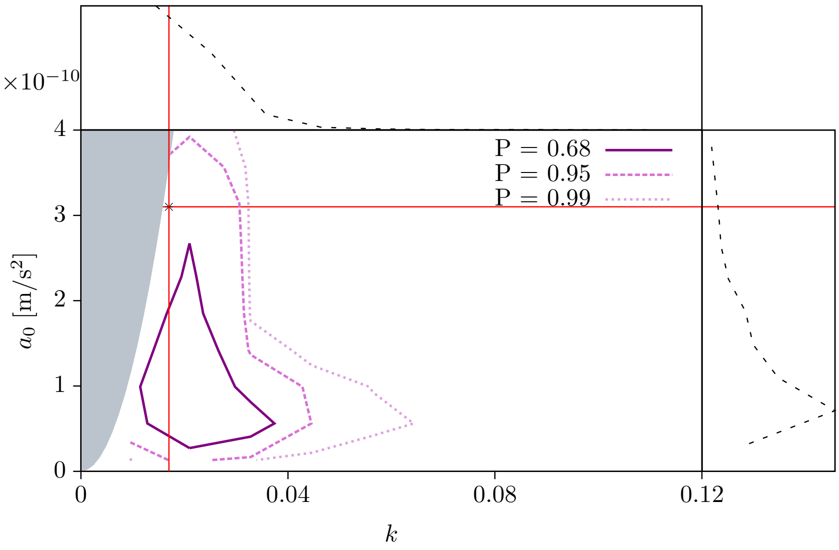

Figure 46: Same as Fig. 45 but for the requirements noise.

dependencies. As indicated in Eq. (8.16), the $\mathcal{S}$ hypothesis requires us to integrate the joint probability $p(\{\tilde{x}\}, k, a_0)$ over the parameter space of the signal (k, a_0), whereas the evidence for the noise-only model is simply given by the likelihood in Eq. (8.17).

In reality, we will have a single measurement yielding one value for the Bayes factor which itself is a random variable subject to variations between noise realisations. By performing an analysis of the artificial data, however, we can study the distribution of the Bayes factor and therefore understand the interpretation of a single value measurement. For the model selection we analysed the same data as for the parameter estimation. The Bayes factors distributions dependence upon the theory parameters is found in Fig. 51 for the current best estimate noise model and in Fig. 52 for the requirements noise. We show the logarithms of the Bayes factor estimates at the 7 representative points in the parameter space collected in Table 4. In 5 cases out of 7 the Bayes factor logarithms all have positive values:

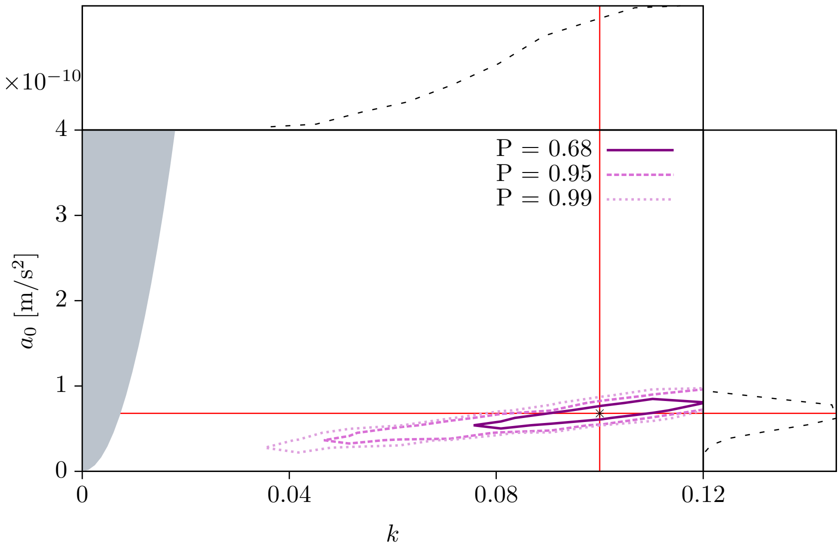

Figure 47: Posterior probability distributions and marginalised posterior distributions for the current best noise estimate for parameters of the signal modelled for $k = 0.1$ and $a_0 = 0.68 \cdot 10^{-10}\mathrm{m/s^2}$. The red lines indicate the true values at which the simulated signal was injected.

this means that the $\mathcal{S}$ hypothesis will be strongly favoured over the $\mathcal{N}$ hypothesis. On the other hand, negative logarithms of the Bayes factor imply that the noise-only model $\mathcal{N}$ is favoured. This occurs in 2 cases out of 7. One of these is the noise-only ($k = 0$, $a_0 = 0\,\mathrm{m/s^2}$) point, where the data only contains noise: this behaviour is therefore expected. The second point is at ($k = 0.1$, $a_0 = 0.2 \cdot 10^{-10}\,\mathrm{m/s^2}$). In this case, noise and signal are mixed, but a rejection of the $\mathcal{S}$ hypothesis is likely.

The analysis just discussed shows a rigorous way of determining the detectability of a signal. While we solely considered a noise-only model and a signal model of MONDian inspiration, we note that our analysis can be extended to include other models, as, for example, models with non-Gaussian noise or ones incorporating glitches that

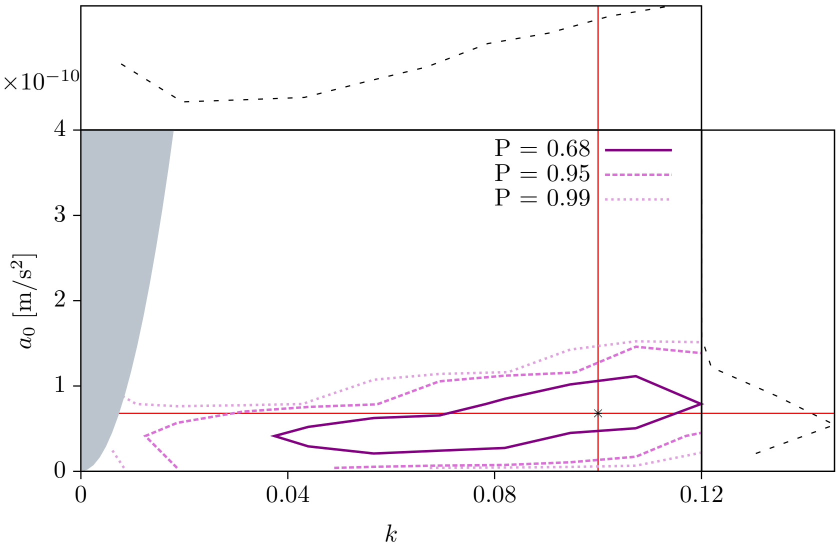

Figure 48: Same as Fig. 47 but for the requirements noise.

could resemble the signal. In addition we can probe whether the data will be best described by one theory or another when it exhibits a deviation from the Newtonian background.

8.4 CONCLUSIONS

As shown in Eq. (5.15), the gravitational stress tensor affects the relative acceleration between the two test masses onboard the spacecraft. The tidal field can be sampled by LPF, allowing us to measure its (dis)agreement with the Newtonian tidal field. The time series that an LPF measurement will provide depends on the trajectory of the spacecraft and on the orientation of its sensitive axis via the seven mission parameters listed in Eq. (5.22). The data analysis framework we built will allow for quantitative statements on measuring the tidal field and posing constraints on alternative theories of gravity.

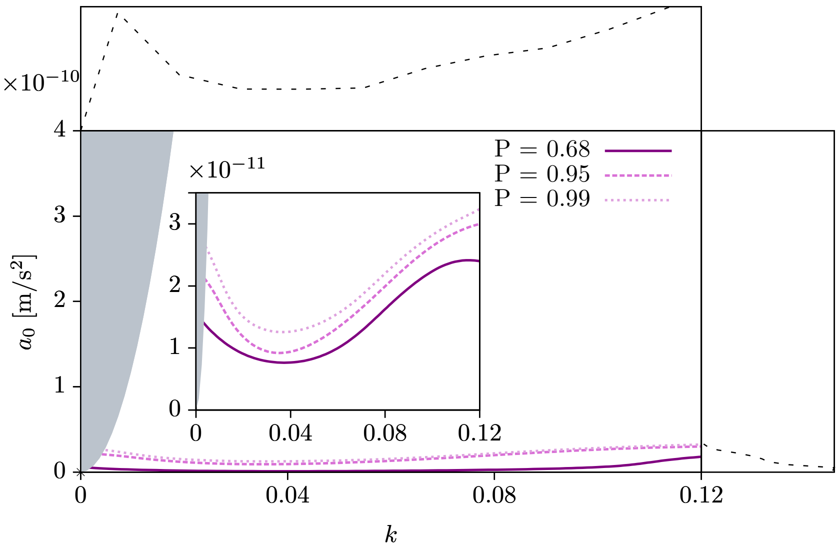

Figure 49: Posterior probability density for the current best estimate noise realisation in the case of no signal injection, i.e. $\tilde{h}(f_j, \lambda_0^m, \lambda_0^t) = 0$.

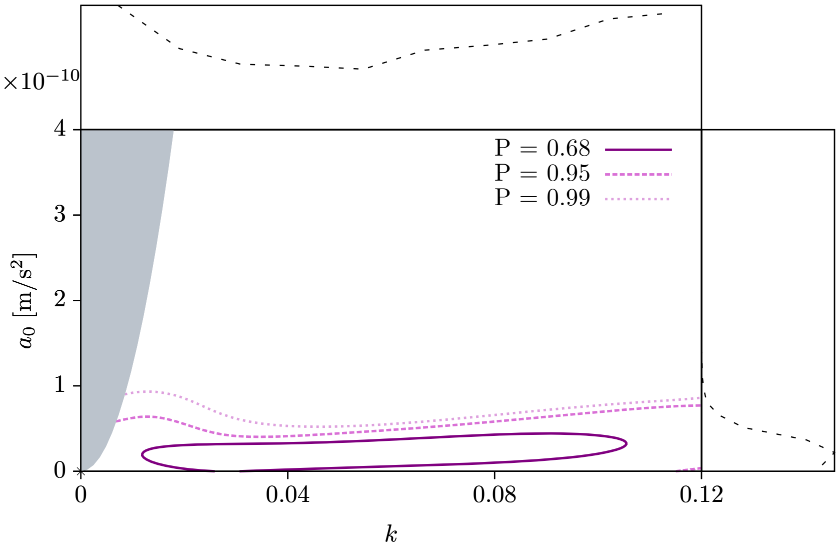

Figure 50: Same as Fig. 49 but for the requirements noise.

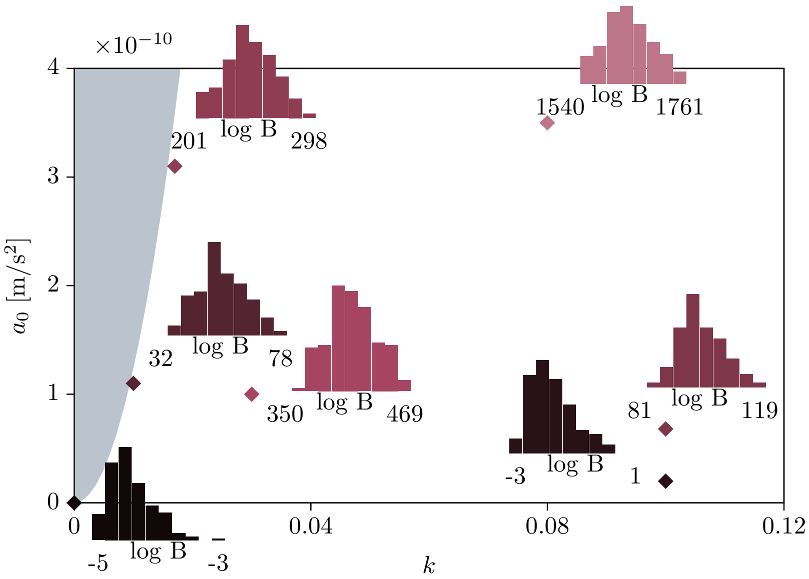

Figure 51: Histograms of the logarithms of the Bayes factor log B for the 200 noise realisations (current best estimate) at the 7 representative points in the parameter space, where the signals were injected. These points are listed in Table 4.

Testing our data analysis approach required picking a theory of gravity that predicts deviations from the Newtonian tidal stresses within the Solar System, where LPF will fly. As discussed in Sec. 4.4, we considered the example of the TeVeS theory. This choice is convenient as we are able to calculate signal templates from it. In the regime of our interest, the signal measured by LPF depends on two theory parameters only, namely, a dimensionless coupling constant k and a characteristic acceleration a_0. Having picked an alternative theory of gravity, we were able to quantify how the signal is influenced by variations of each of the mission parameters. We concluded that, within the errors on the measurement of the position of the spacecraft, the variations of the signal will be negligible. This is a crucial result as it allows us to fix the values of the mission parameters when building signal templates in order to carry out a Bayesian analysis of

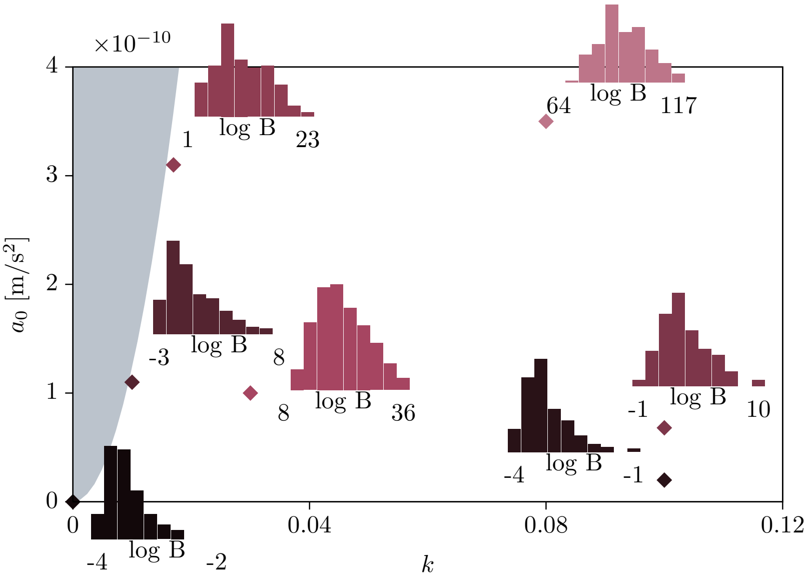

Figure 52: Same as Fig. 51 but for the requirements noise.

the theory parameter estimation and a model selection. However, the impact of possible correlations between the mission and the theory parameters on the conclusions drawn so far in our study was not assessed. Nevertheless, we expect this correlation to be insignificant and leave this investigation for the future work.

The results of our Bayesian analysis are presented in Sec. 8.3 in the form of posterior distributions for the two theory parameters that determine the signal. These are obtained by considering 200 different noise realisations. Some combinations of the parameters (*point* 1 and *point* 2 in Table 4) yield a sharp and narrow joint posterior distribution, indicating that it will be possible to estimate the theory parameters with high precision in case of high SNRs. For weak signals with low SNRs (*point* 5 and *point* 6 in Table 4) the parameter k can only be poorly estimated from the posterior probability. The results for the current best estimate of the noise systematically exhibit better parameter estimation and better distinction between the noise and the signal hypotheses (see Figs. 51 and 52) than the requirements noise. As the former model was built upon the estimates of the noise from the flight hardware test campaigns (see Sec. 5.3), it is a good approximation of the noise during flight.

We also considered the special case in which the data consists of noise only, i.e. a modified gravity signal is absent. This is a very important case as it is a priori the most likely possible outcome of the experiment. In this scenario, the parameter space outside the confidence area of the posterior distribution can be ruled out. In the case of no signal injection, we obtained an average error on the determination of a_0 which is $\overline{\Delta a_0} = 0.055 \cdot 10^{-10}\,\mathrm{m/s^2}$ for the current best estimate noise model and $\overline{\Delta a_0} = 0.154 \cdot 10^{-10}\,\mathrm{m/s^2}$ for the requirements noise. This rules out most values of a_0 except those that are close to $0\,\mathrm{m/s^2}$. At the same time, there is a complete uncertainty on k, which means that we will not be unable to draw any conclusions on this parameter in case of no signal detection.

In order to distinguish between signal detection and no signal detection, we used the Bayesian approach to model selection. We limited the choice to two models: one is the sum of noise and signal (signal hypotheses), while the other consists of noise only (noise hypothesis). We computed the ratio of the probabilities for these two hypotheses given the data and based on this number drew a conclusion on which model is preferable. We estimated the expectation for a signal in the artificial data by calculating Bayes factors for 200 different noise realisation for several points in the parameter space listed in Table 4. On the basis of these estimates, we were able to allocate areas in the parameter space where the signal hypothesis could be strongly prioritised over the noise hypothesis and areas where even in presence of a signal a confident statement on its detection cannot be made. Notice that for a single fly-by the experiment will provide us only with a single measured dataset and a single deduced Bayes factor. The estimates of the Bayes factors for the artificial data gives a way to compare the single Bayes factor estimated from the real data to the expected values and judge the outcome of the experiment on the basis of this comparison.

Finally, we studied the data from one of the test campaigns for LPF. The importance of this study lies in the fact that in reality the noise may have glitches and non-Gaussianities (see Fig. 53). When applied to this data, our Bayesian model selection can prefer the signal hypothesis over the noise hypothesis because neither of them describes the data with the glitch correctly. In order to adequately address the problem of glitches, a separate model to be fed to the Bayesian hypothesis selection approach must be developed.

In our analysis we investigated the influence of the parameters k and a_0 on the template, but we kept the interpolating function fixed. As the interpolating function is heuristically designed on the basis of astrophysical observations, it is not a smoothly varying parameter but a point model. In the next Chapter, we would like to apply the data analysis framework we built to study a generalised, phenomenological model of the interpolating function that uses a finite set of parameters. This would allow us to assess different theories that have MOND as their non-relativistic limit. Ultimately, the more general goal is to consider other theories that yield a phenomenology detectable with LPF and to be able to perform a model selection among different models of gravity.

The significant issue that has to be assessed in the future work is the influence of the mission design and the mission time-line on the experiment. We will have to study the influence of the accuracy of the acceleration recovery from the measurement of the displacement on the parameter estimation. Finally, the question of how much data before and after the SP fly-by needs to be gathered to perform an accurate estimation of the acceleration and the rate of the outliers in the data is left for the future work.

Part IV

MODEL SELECTION

9

DETECTOR NOISE ARTEFACTS. MODEL SELECTION BETWEEN GLITCHES AND SIGNALS

9.1 THE GLITCH PROBLEM

So far we analysed the simulated LPF data with noise taken to be Gaussian and the ASD defined by the theoretical amplitude spectral density of LPF. In reality, however, non-Gaussian glitches might appear in the noise as shown in the measurement of the differential displacements from the test campaigns for LPF [1] [56, 57, 49]. We now examine the response of our data analysis framework to glitches by performing parameter estimation and model selection on the OSTT data. We keep working in the *TeVeS* (k, a_0) parameter space and use the signal templates produced within this theory.

We shift the test campaign data so that a glitch occurs at the expected signal arrival time, as shown in Fig. 53. We then estimate the posterior probability distribution for k and a_0 for this dataset. Results are presented in Fig. 54. The posterior probability peaks at $(k = 0.12, a_0 = 1.34 \cdot 10^{-10}\ \mathrm{m/s^2})$. The standard deviations for the two parameters are given by $\Delta k = 0.001$ and $\Delta a_0 = 0.07 \cdot 10^{-10}\ \mathrm{m/s^2}$, respectively. The recovered parameter values are in the parameter space region that is inconsistent with the noise-only model. Additionally, the estimated value of the parameter k is on the boundary of the parameter range defined by the parameter priors. The logarithm of the Bayes factor is

$$\log p(\mathcal{S}|\{\tilde{x}\}, I)/p(\mathcal{N}|\{\tilde{x}\}, I) = 199, \qquad (9.1)$$

---

[1] The LPF spacecraft is already being prepared for launch and is undergoing several instrumental tests. To assess the impact of noise artifacts, we took the data available from the LPF On-Station Thermal Tests (OSTT) performed by Astrium Ltd., Astrium Satellite GmbH (Astrium Deutschland (ASD)) extensively testing the end-to-end performance of the OMS. However, we would like to point out that the noise artifacts might have been artificially caused by the test environment.

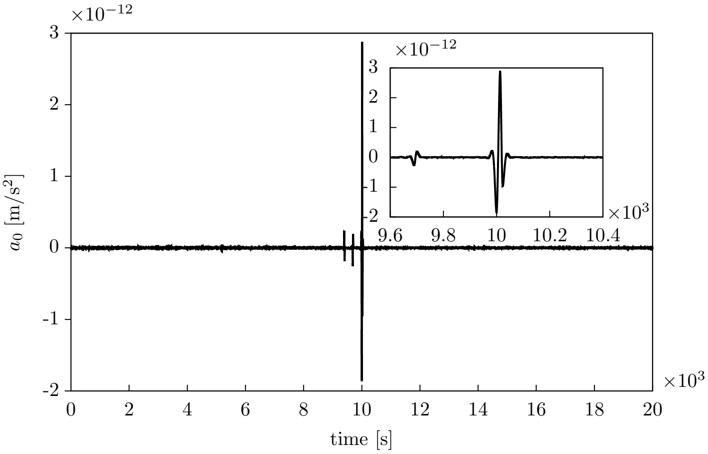

Figure 53: Data from the test campaign with a glitch of unknown origin bandpass filtered in the sensitive frequency band of LPF.

so that the $\mathcal{S}$ hypothesis is prioritised over the $\mathcal{N}$ one.

This can happen if the characteristic frequency of the glitch is similar to the characteristic frequency of the signal and highlights that, in order to achieve confident signal detection, we must introduce more realistic noise models. In particular, these should describe non-Gaussianities in the noise, such as glitches. With such noise models it would be possible to extend the model selection described in Sec. 8.2 and distinguish between noise artifacts and authentic signals. The question of the non-stationarities and glitches in the data is particularly important in the setup of this experiment because our measurement relies on one or two repetitions at the most (one or two SP fly-by's). Multiple SP fly-by's can significantly increase our confidence in signal detection against glitches in the data. However, distinguishing between noise glitches and signal, and characterising glitches are very important topics that are going to be discussed in this Chapter.

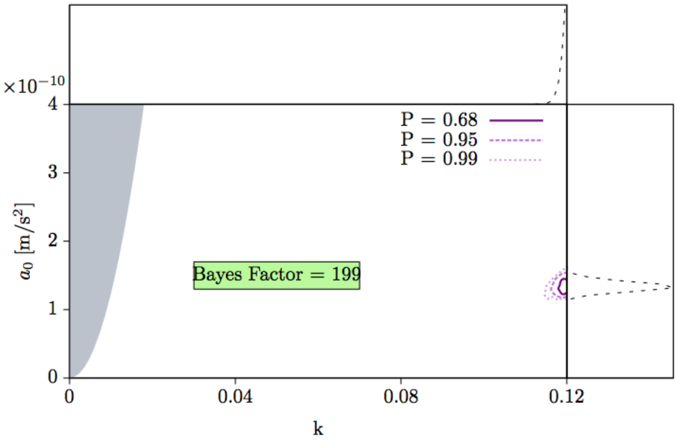

Figure 54: Resulting posterior probability density for the parameter estimation in case of the realistic data of Fig. 53.

9.2 REAL OPTICAL METROLOGY SYSTEM NOISE FROM THE TEST CAMPAIGN

9.2.1 *Non-Gaussianities in interferometric measurements*

In Chapter 8 we developed a scheme for analysing the data from the saddle point fly-by experiment. The analysis was applied to artificially simulated data containing noise generated by drawing random samples from the Gaussian distribution with the known noise ASD. The spectral density was constructed based on the noise contributions from different components of the instrument, such as OMS, IS, direct forces on the Spacecraft, electrostatic actuation system and others [12]. In the case when the noise in the data can be sufficiently described by the Gaussian noise, then parameter estimation and model selection given in Chapter 8 would be enough to perform data analysis for the experiment. However, experience with ground based interferometers designed to detect gravitational waves shows that the noise is not always Gaussian [29]. Further the test campaign data from Section 9.1 shows that there might be glitches in the data that regardless of their influence on the overall performance of the instrument might be important for our experiment. As it was pointed out in Section 9.1 the experiment will be carried out only once or twice, therefore it is important to extract the maximum amount of information and have a rigorous way to distinguish parts of the parameter space that can be contaminated by glitches. Consequently we have to take into account the non-Gaussianities and noise artefacts that can be the source of confusion for the outcome of our experiment. The common departures from the Gaussianity appear in the outliers present in the data and the overall *heavier tails* of the data's probability density. Thus, the non-Gaussianities that might appear in the data can be taken into account in two steps. First of all we will make a separate model for the glitches in the data. This would be an analytically parameterised model. The purpose of modelling the glitch is to have a way of distinguishing between signals and noise artefacts. The second component of modelling the non-Gaussianities is assuming *Student's t* distribution for the data which is better for incorporating the outliers and has parameters that can be adjusted according to the data [87, 86]. This approach of assuming a *Student's t* likelihood not only incorporates 'heavier tails' to the distribution but also accounts for insufficient prior knowledge of the noise ASD. Since the glitches that occur in the data do not allow to choose an appropriately long piece of data to make a robust estimate of the ASD. Thus marginalising out the noise variance from the likelihood function solves the problem of having an accurate ASD estimate.

9.2.2 *Test campaign data for LPF*

The most realistic data for LPF that we have available are the data that were produced with the flight hardware [49, 56, 57] during the test campaign performed by Astrium (Airbus Space and defence) on the Industrieanlagen-Betriebsgesellschaft mbH (iABG) facility near München in 2011. The data that we have used are the performance measurements of the fully assembled OMS with its control loops being locked and with the noise level reaching the required performance. To perform these measurements free-falling test masses were replaced with fixed mirrors, that were aligned with 1 μrad precision.

During this test campaign various measurements with different configurations and scenarios were conducted. We are interested in two data sets from that test campaign. These are the performance measurements that were made with the two different temperature regimes and were named *Hot Performance Measurement* and *Cold Performance Measurement*. Both sets of measurements were made after an adequate level of thermal stability was achieved and the relevant control loops were locked to bring the OMS into performance mode.

9.3 LISA PATHFINDER SOFTWARE SIMULATOR

The data from the test campaign represents realistic OMS noise. Consequently we need to take the other noise sources into account by modelling their contributions to the overall instrument's noise.

LPF can be schematically represented as a set of subsystems plotted in Fig. 55. Each subsystem can be represented as matrix of coefficients which embody processes that happen in the system while the signal propagates through it. The set of sensors – OMS, IS and Star Tracker (ST) – measures the positions of the test masses and the spacecraft. We are interested in the measurements made with OMS, which measures 6 degrees of freedom for the two test masses – 4 angles ϕ_1, η_1, ϕ_2, η_2, the position of the first test mass x_1, and the distance between two test masses x_{12}, that is the observable that we are interested in. We will call the direction along the x_{12} measurement the sensitive axis. The On-board Computer (OBC) has Drag-Free Attitude Control System (DFACS) as its subcomponent that propagates the signal to the controllers, namely *Capacitive actuators* and μ*N-thrusters* that maintain the spacecraft in a free fall. This is represented in the *Dynamics* of the spacecraft. Thereafter the motion of the spacecraft and the test masses are measured with the sensors.

The simulator implemented in LISA Technology Package Data Analysis (LTPDA) [3] uses a *state-space model* to represent the dynamics and the feedback of the system

$$\begin{cases} \dot{\mathbf{x}} = \mathbf{A}\mathbf{x} + \mathbf{B}\mathbf{u} \\ \mathbf{y} = \mathbf{C}\mathbf{x} + \mathbf{D}\mathbf{u}, \end{cases} \tag{9.2}$$

where **u** is the vector of inputs, **x** is a vector of *states*, and **y** is a vector of outputs and the matrices that describe the propagation of these vectors through the system.

In the test campaign the test masses are replaced with fixed mirrors, and therefore only the noise is propagated through the system. Therefore the data measured in 6 OMS channels (two displacement and four angles measurements) have to be injected as noise into the simulator. This can be done for each subsystem and in our case it is going to be the *interferometer readout noise* as shown in Fig. 55. The estimates for the remaining noise sources are already modelled in the simulator and will be added to the injected noise. The models of the noise PSDs and couplings for the other subsystems are measured during the flight hardware tests in the ground based laboratories of the Universities and research Institutes involved in LPF study.

The output of this process is a time series of the LPF noise with the OMS noise taken from a test campaign that used the flight hardware.

9.4 CONVERSION OF THE DISPLACEMENT DATA TO ACCELERATION

The primary measurement made by LPF is the variation in the distance between test masses 1.73. However, the cause of these changes is the gravitational tidal force that acts on the test masses as they follow the geodesics in the curved space-time. Thus the task of measuring the residual differential acceleration of two free-falling test masses is one of the main objectives of the LPF mission and, therefore, the conversion from the observed differential displacements to differential accelerations has been analysed in depth [107, 75].

LPF is designed to keep the distance between the two test masses constant at frequencies below 1 mHz by accounting for external forces, whereas at the sensitivity frequencies of $1-30$ mHz the test masses are in free fall. Both test masses are accommodated within one space-

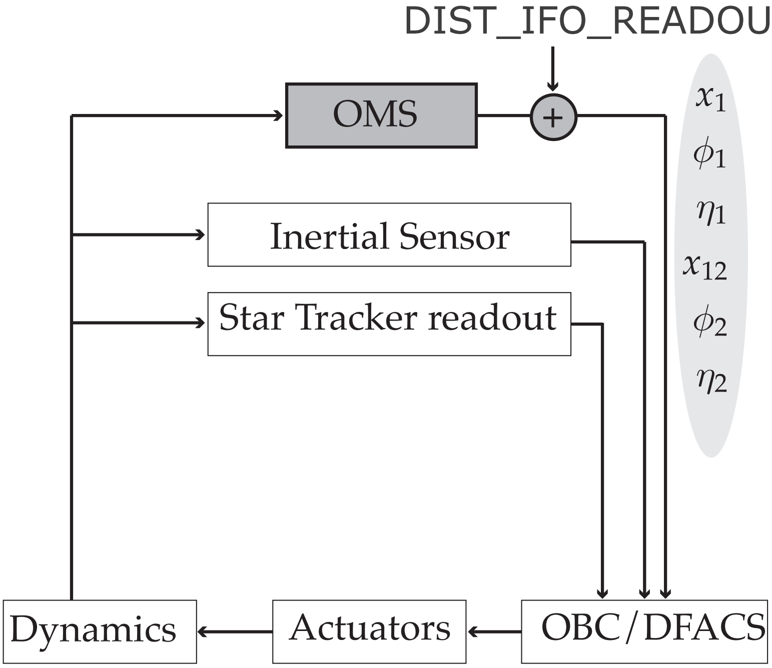
DIST_IFO_READOUT
OMS
+
x_1
ϕ_1
η_1
x_{12}
ϕ_2
η_2
Inertial Sensor
Star Tracker readout
Dynamics
Actuators
OBC/DFACS

Figure 55: LPF simulator

craft and free-fall is achieved by controlling the position of the spacecraft relative to one test mass. The position of the second test mass is then controlled relative to the first outside the LPF sensitive frequency band. The differential gravitational force can thus be recovered from the measurement of the differential displacement. An anomalous stress tensor predicted by an alternative theory of gravity may therefore be sensed by LPF as the differential force acting on the test masses.

We can now write the equation of motion for the two test masses. For simplicity, we can write the equations of motion along only one of the axes

$$L = \frac{m}{2}\dot{x}_1^2 + \frac{m}{2}\dot{x}_2^2 - \frac{k_1}{2}x_1^2 - \frac{k_3}{2}(x_2 - x_1)^2 - \frac{k_3}{2}x_2^2, \tag{9.3}$$

where the terms $k_1 x_1$ and $k_2 x_2$ are the spring couplings between first and second test masses respectively with the spacecraft; and $(k_3/2)(x_2 - x_1)^2$ represents the gravitational coupling between the test masses.

Writing the equations of motion for the test masses using this Lagrangian [75] one can arrive at the equations that describe the force acting on each of the test masses. This includes the forces from the drag-free and the suspension control loops and the couplings between the test masses and the spacecraft.

This is performed by taking into account the models [107] of the LPF subsystems in the equations of motion for the test masses along the sensitive axis, described by

$$\mathbf{a} = [\mathbf{D}^{-1}\mathbf{I}^{-1} + \mathbf{C}]\mathbf{o}, \tag{9.4}$$

where $\mathbf{o} = (o_1, o_\Delta)^T$ is read interferometrically along the sensitive axis of LPF by the two interferometers on board, o_1 is the position of the first test mass relative to the spacecraft, and o_Δ is the position of the second test mass relative to the first. The estimate residual acceleration of the spacecraft and the estimated residual differential acceleration of the two test masses are $\mathbf{a} = (a_1, a_\Delta)^T$, with $a_1 = d^2x_1/dt^2$ and $a_\Delta = d^2\xi/dt^2$, respectively. The matrix $\mathbf{D}$ represents the dynamics of the spacecraft, $\mathbf{I}$ is the interferometer sensing matrix, and $\mathbf{C}$ is the controller transfer functions. More specifically, we can write the dynamics of the spacecraft as

$$\mathbf{D} = \begin{bmatrix} \frac{1}{(s^2 + \omega_1^2)} & 0 \\ -\frac{(\omega_2 - \omega_1)^2}{(s^2 + \omega_1^2)(s^2 + \omega_2^2)} & \frac{1}{(s^2 + \omega_2^2)} \end{bmatrix}, \tag{9.5}$$

where s is a Laplace domain complex variable and $\omega^2_{\{1,2\}} = k_{\{1,2\}}/m$. The mass of the test-mass is m and $k_{\{1,2\}}$ are the spring constants that model the gravitational and electrostatic couplings between the test masses and the spacecraft as it was described in Eq. 9.3. Given the coupling factor δ modelling the degree to which the differential interferometer picks up motion of the spacecraft, the interferometer sensing matrix can be written as

$$\mathbf{I} = \begin{bmatrix} 1 & 0 \\ \delta & 1 \end{bmatrix}. \tag{9.6}$$

Finally, the controller matrix that converts the measured signal into the commanded forces may be written as

$$\mathbf{C} = \begin{bmatrix} H_{\mathrm{df}} & 0 \\ 0 & H_{\mathrm{sus}} \end{bmatrix}, \tag{9.7}$$

where H_{df} and H_{sus} are the gains of the drag-free and suspension control loops along the sensitive axis of LPF, respectively. The drag-free control loop actuates on the spacecraft via micro-Newton thrusters, while the suspension loop actuates on the second test mass by electrostatic actuation.

9.5 TYPICAL NON-GAUSSIANITIES OBSERVED IN THE DATA

Here we present the performance measurements from the test campaign (see Sec. 9.2) converted to the acceleration (see Sec. 9.4) and processed with the LPF simulator (see Sec. 9.3).

The LPF simulator adds the noise contributions from the various subsystems of LPF on top of the interferometer noise measured during the test campaign. In this way we can assess the noise realisation which is closest to the real noise during the flight acquired using the flight hardware measurements on Earth. The data shown in Figures 56 and 57 exhibit outliers that can cause problems in the model selection between the signal model and the noise as was pointed out in the example from the Sec. 9.1. In that example the *glitch* in the data can be more favoured by our analysis as a signal as opposed to noise, therefore, we need to make a separate model for a glitch. Moreover if we compare the distribution of the data with the Gaussian distribution, we can see that the overall data distribution has *heavier tails*. This is shown in Fig. 58, where the ordered values of the data (the dataset presented in Fig. 57a) are plotted against the probabilities from the cumulative distribution function (cdf) of the Normal distribution.

If the data were drawn from the Gaussian distribution, it would be lying on the straight dashed line. However, Fig. 58 displays the tails that do not agree well with the Gaussian distribution. We can see from the plot that the tails of the distribution can be more accurately described by the *Student's t* cdf. Consequently, in this study we will use the *Student's t* likelihood for the parameter estimation and model selection as well as the Gaussian likelihood. We will compare the performance of two likelihoods on the data sampled from the *Student's t* distribution with the parameters that are fitted to the data from the test campaign. The probability density function (pdf) of the *Student's t* distribution is

$$p(\tilde{x}_j|\nu_j, s_j) = \frac{\Gamma\left(\frac{\nu_j+1}{2}\right)}{\Gamma\left(\frac{\nu_j}{2}\right)} \left(\frac{\nu_j s_j^2 + \tilde{x}_j^2}{2}\right)^{-\frac{\nu_j+1}{2}} \left(\frac{\nu_j s_j^2}{2}\right)^{\frac{\nu_j}{2}} . \tag{9.8}$$

This distribution is characterised by three parameters (s, ν): a scale parameter s and a parameter describing the number of degrees-of-freedom μ. The choice for these parameters will be described later in the context of the definition of the *Student's t* likelihood.

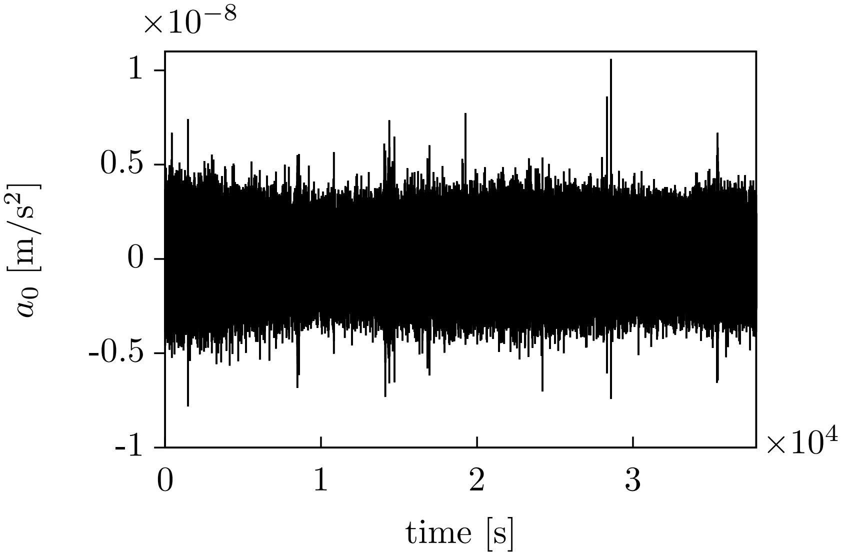

(a) First performance measurement (part 1)

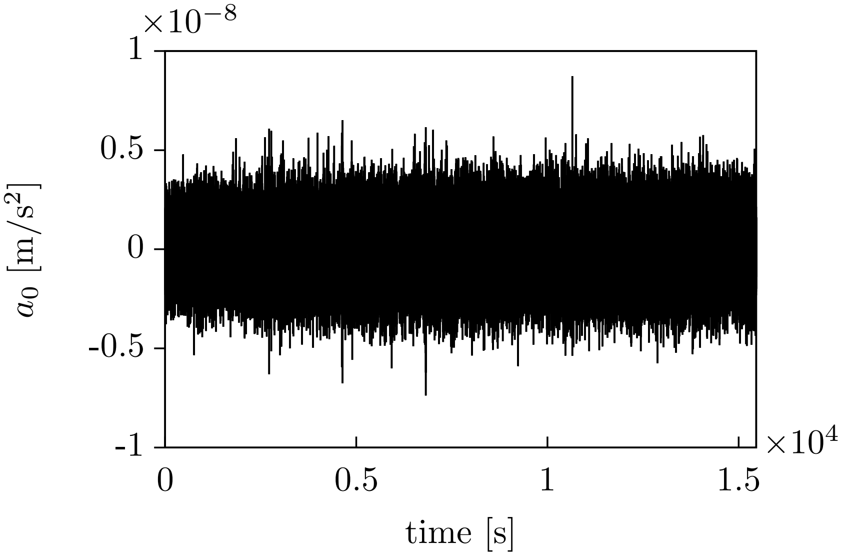

(b) First performance measurement (part 2)

Figure 56: Performance measurements from the test campaign. *Cold* runs.

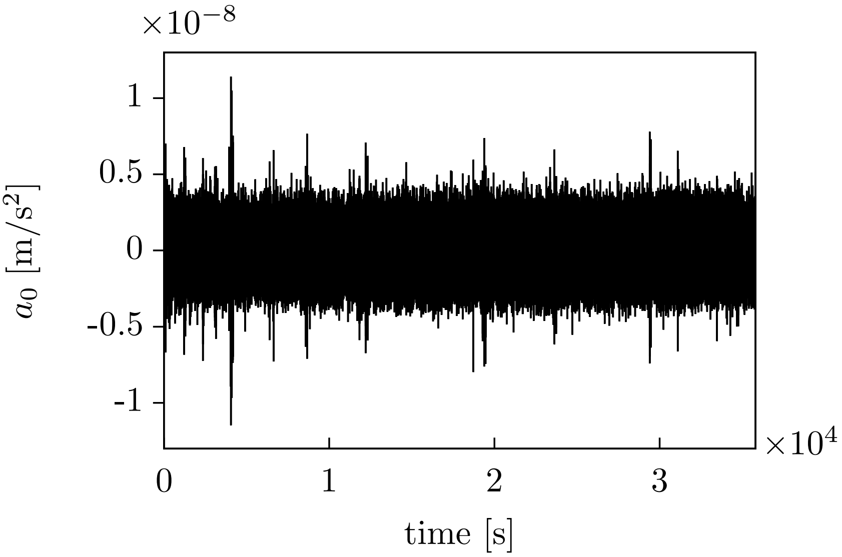

(a) Second performance measurement (part 1)

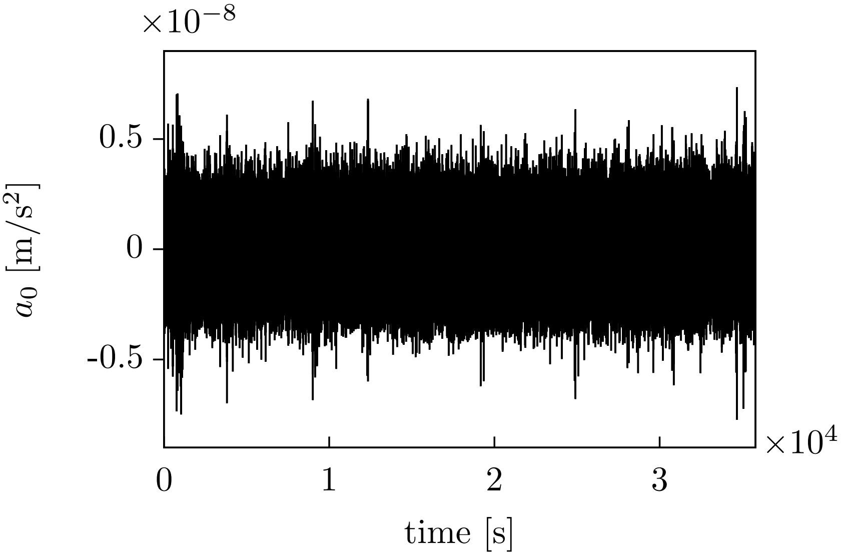

(b) Second performance measurement (part 2)

Figure 57: Performance measurements from the test campaign. *Hot* runs.

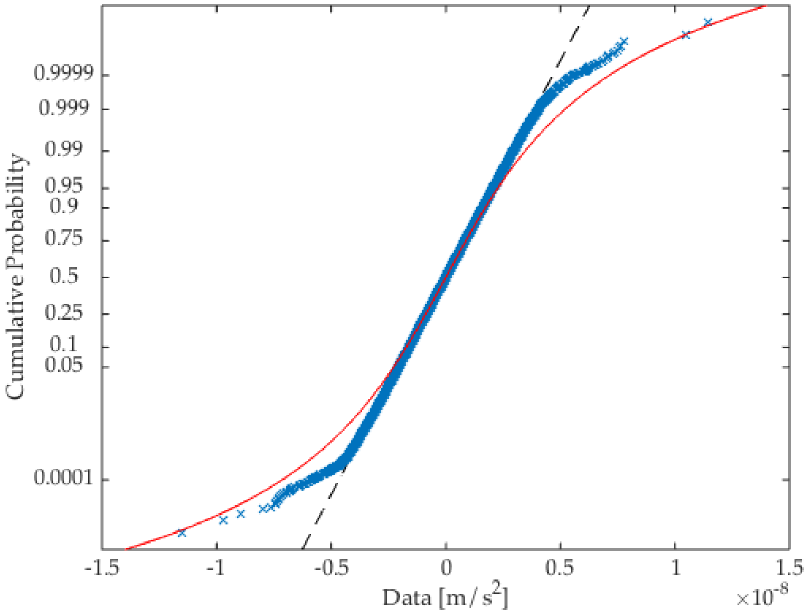

Figure 58: Distribution of the data compared to the *Normal* distribution and to the cdf of the *Student's t* distribution. This is the probability plot that plots the sorted data versus the quantiles of the Gaussian distribution.

9.6 MODELLING NOISE ARTEFACTS

The data from the test campaign exhibit spurious signals of varying durations and amplitudes. Rather than treating them as Gaussian noise, a more generalised way to describe these noise artefacts would be to introduce a parameterised model. The way in which these artefacts appear in the data indicate that they may be described by a deterministic process with a short time duration compared to the overall measurement, with a model similar to the driven harmonic oscillator. Thus a straight-forward approach to modelling the glitches is to use a sine-Gaussian model [32] which describes the glitch as a sine-function with a Gaussian envelope

$$G(t;A,t_0,f_0,\tau,\phi_0) = A\exp\left(-\frac{(t-t_0)^2}{\tau^2}\right)\cos\left(2\pi f_0(t-t_0)+\phi_0\right), \tag{9.9}$$

where $\tau = Q/(2\pi f_0)$ can be interpreted as the duration of the glitch. The glitch is described by the following parameters

A	overall amplitude,
t_0	central time,
f_0	central frequency,
Q	number of cycles,
ϕ_0	central phase.

We take the ranges for the parameters to be

$A \in [0; 2\times 10^{-9}]$ [m/s^2],
$t_0 \in [0; T]$ [s],
$f_0 \in [10^{-5}; 1]$ [Hz],
$Q \in [0.1; 10]$,
$\phi_0 \in [0; 2\pi)$ [rad].

The maximum value of the amplitude is chosen based on the distribution of the noise from the test campaign and the minimum is taken to be zero. The upper limit on t_0 is T, which is the duration of the measurement. The range for the central frequency parameter matches the sensitivity range of the instrument, however, the real minimum frequencies for detectable signals will depend on the length of the measurement. This is due to the frequency resolution $\Delta f = 1/T$, which, for example, for the measurement of the length 1000 s will be equal to 10^{-3} Hz. The phase parameter is uniformly distributed over the interval 0 to 2π. The parameter Q is proportional to the duration of the glitch. The lower boundary describes a single spike glitch and the upper boundary is equivalent to 10 cycles.These choices represent very conservative values based on the test campaign data.

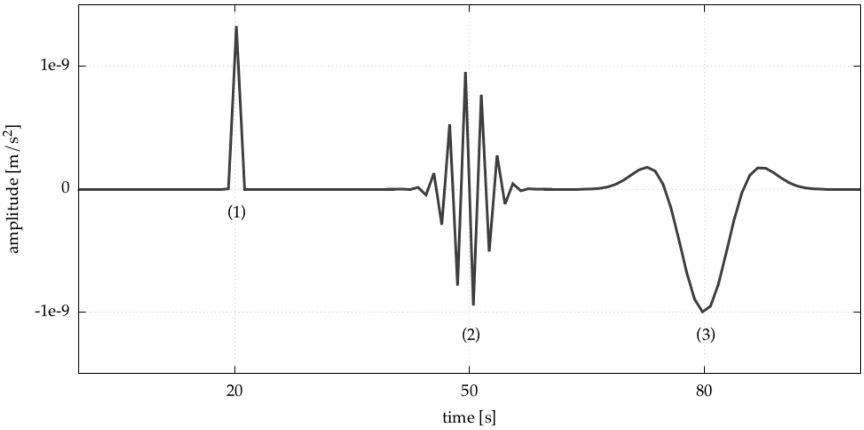

Figure 59: Examples of the sine-Gaussian signals with the following parameters:
(1) $A = 2 \cdot 10^{-9} \mathrm{m/s^2}$, $\varphi = 2\pi n$, $f_0 = 0.1\mathrm{Hz}$, $Q = 0.2$, $t_0 = 20\mathrm{s}$
(2) $A = 10^{-9} \mathrm{m/s^2}$, $\varphi_0 = 1.8 \pm 2\pi n$, $f_0 = 0.5\mathrm{Hz}$, $Q = 10$, $t_0 = 50\mathrm{s}$
(3) $A = 10^{-9} \mathrm{m/s^2}$, $\varphi_0 = \pi \pm 2\phi n$, $f_0 = 0.05\mathrm{Hz}$, $Q = 2$, $t_0 = 80\mathrm{s}$, with $n \in \mathbb{Z}$

In Fig. 59 example time domain plots for some glitches are presented.

9.7 MODEL OF THE SIGNAL

9.7.1 *Two parameter model of the signal*

We want to have a model of the signal that is independent of the chosen modified theory of gravity. However the results of the experiment should be easily interpreted in terms of the existing modified theories. Thus, we want to have a parameterised model, such that the parameters of this generalised model could be easily interpreted and cast into the signal predictions for any chosen alternative theory of gravity. Consequently we will need a parametric model that has parameters that define the amplitude of the signal, the time of its arrival and its width. The Lorentzian function is a good model that suits these purposes, however it is going to be modified in a way that it is no longer normalised as a probability distribution but has an independent parameter that is responsible for the variations of the amplitude:

$$S(t) = -\frac{1}{\pi}\frac{\frac{1}{2}A}{(t-t_0)^2 + (\frac{1}{2}\Gamma)^2}. \tag{9.10}$$

Thus we have a model with three parameters

A amplitude [m],
t_0 central time [s],
Γ width [s].

In Fig. 60 we show the signature of this function for some choices of parameters.

As a result we have a model of the signal with two parameters, amplitude and duration of the signal. The time of the signal arrival is also a parameter but we assume it to be fixed because as was discussed in the previous chapters (see discussion on the trajectory parameters), our knowledge on the position of the saddle point and on the trajectory of the spacecraft would be sufficient enough to assume this parameter to be constant. However, if at some point it is required

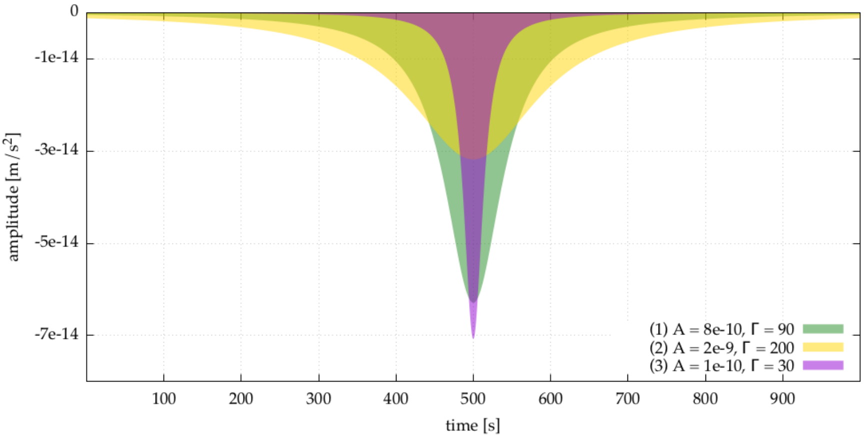

Figure 60: Signal model for several choices of parameters. Functions are plotted on the interval $[0;1000]$ s and in all cases the time of arrival is fixed to the same value $t_0 = 500$ s.

that the time of arrival be made a variable, then our model can be easily extended to have an additional parameter with the appropriate choice of prior.

9.7.2 *Prior ranges on parameters*

We define the prior ranges on this parameter space by estimating the maximum log-likelihood for the parameters of the generalised model, given the data produced from the numerical solutions for one alternative theory of gravity that we have investigated in the previous chapters, namely TeVeS. We find how the TeVeS space maps onto the new parameters by finding locations of best fit defined by maximising the likelihood.

$$\mathcal{L}(\theta) = \prod_{j=0}^{N} p(\tilde{x}_j|\theta) \propto \prod_{j=0}^{N} \exp\left[-\frac{|\tilde{x}_j - \tilde{s}_j(\theta)|^2}{2\tilde{\sigma}_j^2}\right]. \tag{9.11}$$

Here the parameters are $\theta = \{A, \Gamma\}$, and the data in the frequency domain are $\tilde{x}_j = \tilde{h}_j + \tilde{n}_j$. The data will be are noise free templates

($\tilde{n}_j = 0$) drawn from the numerically simulated solutions of TeVeS theory predictions of the gravity stress tensor around the saddle point (see Sec. 6.1). We want to find the parameters $\{A, \Gamma\}$ that maximise the likelihood function. Since the likelihood is a smooth function of its argument we can as well consider the natural logarithm instead and neglect the constant terms that would not displace the position of the function's maximum:

$$\ln \mathcal{L}(A,\Gamma) \propto \sum_{j=0}^{N} -\frac{|\tilde{h} - \tilde{s}(A,\Gamma)|^2}{2\tilde{\sigma}^2} = \sum_{j=0}^{N} -\frac{|\tilde{h}|^2 - 2\tilde{h}\tilde{s}^*(A,\Gamma) + |\tilde{s}(A,\Gamma)|^2}{2\tilde{\sigma}^2}, \tag{9.12}$$

with σ_j – the PSD of the noise normalised by the frequency bin resolution.

The estimated values of the parameters will then be

$$\{\hat{A}, \hat{\Gamma}\} = \underset{A,\Gamma}{\mathrm{argmax}} \ln[\mathcal{L}(A,\Gamma)] = \underset{A,\Gamma}{\mathrm{argmax}} \sum_{j=0}^{N} \frac{1}{\tilde{\sigma}_j^2} \left[\tilde{h}\tilde{s}^*(A,\Gamma) - \frac{1}{2}|\tilde{h}|^2 - \frac{1}{2}|\tilde{s}(A,\Gamma)|^2\right]. \tag{9.13}$$

The templates from the numerical calculations were taken from a 9×9 grid and are described in Sec. 6.1. We have mapped the values of parameters to the new parameter space based on the estimate of the parameters that maximise the likelihood function [see Eq. (9.12)]. The colour of the points for the mapped parameters correspond to the values of the overlap between the template from the numerical simulations of the TeVeS function and template from the proposed generalised function. The overlap is calculated as the scalar product between two templates weighted by the noise and normalised by the length of the vectors $\tilde{h}$ and $\tilde{s}$. The plot shows that the overlap calculation will not be a good measure for finding the best match of one parameter space to another because it cancels out the amplitude parameter and thus does not find the best match. This means that location of maximum overlap won't be the location of maximum likelihood and that parameters that maximise the likelihood function will be a better solution.

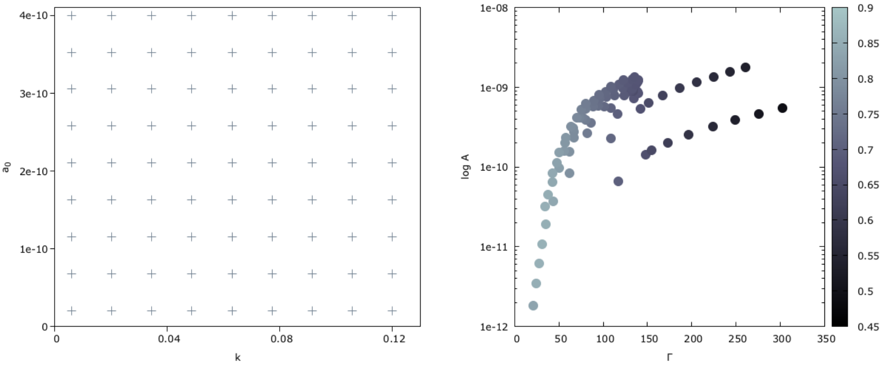

(a) Parameter grid for TeVeS templates.

(b) Corresponding generalised signal parameters. The color scheme corresponds to the values of the overlap, given by Eq. 9.14.

Figure 61: TeVeS parameter space transformed into generalised signal parameter space.

$$C = \frac{(h|s)}{(h|h)(s|s)}, \tag{9.14}$$

where

$$(h|s) = \sum_{j=0}^{N} \frac{\tilde{h}_j(k, a_0)\tilde{s}_j^*(A, \Gamma)}{2\tilde{\sigma}_j}. \tag{9.15}$$

9.8 SIGNAL, NOISE AND GLITCH MODELS

We evaluate which model better describes the data within the framework of Bayesian inference by calculating the posterior probabilities for each one of the proposed models and comparing them with each other. A quantitative way to compare the two models is to look at the ratio of the two posterior probabilities, which gives us the merit to which one model is more probable then the other one

$$\frac{p(\mathcal{M}_\alpha|\{\tilde{x}\}, I)}{p(\mathcal{M}_\beta|\{\tilde{x}\}, I)} = \frac{p(\{\tilde{x}\}|\mathcal{M}_\alpha, I)}{p(\{\tilde{x}\}|\mathcal{M}_\beta, I)} \frac{p(\mathcal{M}_\alpha|I)}{p(\mathcal{M}_\beta|I)}, \tag{9.16}$$

where $\mathcal{M}_\alpha$ and $\mathcal{M}_\beta$ are any two models that are proposed to describe the data. This ratio is often called the Odds ratio. However to estimate the Odds ratio one needs to know the ratio of the prior probabilities for the models. In our analysis we set it to one, therefore assuming that we do not favour one model over the other. This decision is based on the absence of similar experiments, when the gravity is measured directly in the non-relativistic regime with the small gravity gradients. This means that no previous experiments give a sensible way to determine the prior odds. Our results will only represent the information present in the data coupled with our prior beliefs in the model parameters. Therefore, it will say nothing regarding our prior belief in the deviations of the gravity from the Newtonian model. Thus instead of using the Odds ratio, we will use the Bayes Factor estimates

$$B_{\alpha\beta} = \frac{p(\{\tilde{x}\}|\mathcal{M}_\alpha, I)}{p(\{\tilde{x}\}|\mathcal{M}_\beta, I)}. \tag{9.17}$$

The Bayes factor is the ratio of the evidence values for each model. To estimate the evidence we need to integrate out the unknown parameters of the model from the joint probability density function

$$p(\{\tilde{x}\}|\mathcal{M}, I) = \int_\theta p(\{\tilde{x}\}|\theta, \mathcal{M}, I) p(\theta|\mathcal{M}, I) d\theta. \tag{9.18}$$

In Sec. 8.2 it was shown how this approach works for the case of the models described below. According to the first model it is believed that the data consist only of noise

$$\mathcal{N}: \tilde{x}_j = \tilde{n}_j, \tag{9.19}$$

whereas the second model suggests that a signal is present in the noise

$$\mathcal{S}: \tilde{x}_j = \tilde{s}_j + \tilde{n}_j. \tag{9.20}$$

Now we extend this by accounting for non-Gaussian outliers in the data that can be described as high SNR transient signals and, as it was described in the previous section, can be well modelled with sine-Gaussian waveforms.

The most general model for the data based on our current notion of the LPF output is the following one

$$\tilde{x}_j = \tilde{s}_j + \tilde{n}_j + \sum_{i=1}^{m} \tilde{g}_{ij}. \tag{9.21}$$

Here $\tilde{n}_j$ are the noise components that are distributed either according to a Gaussian or *Student's t* distribution. Moreover there may be up to m glitches present in the data. In order to deal with the unknown number of glitches we marginalise over the unknown number m using a Poisson prior distribution on m. This is later estimated from real data obtained prior to the saddle-point fly-by. Therefore taking this into account the evidence can be written as

$$\begin{aligned} p(\{\tilde{x}\}|M_\alpha, I) &= \sum_{i=0}^{\infty} p(\{\tilde{x}\}, m|M_\alpha, I) \\ &= \sum_{i=0}^{\infty} p(\{\tilde{x}\}|m, M_\alpha, I) p(m|M_\alpha, I), \end{aligned} \tag{9.22}$$

where the second term is the prior probability of obtaining m glitches in the data under the model M_α and the first term is the Bayesian evidence for the model assuming m glitches. The number of glitches can be modelled by the Poisson distribution such that

$$p(m|\mathcal{M}_\alpha, I) = \frac{\lambda^m e^{-\lambda}}{m!}. \tag{9.23}$$

However, here we will be testing only the case for $m = 1$. The reason is that at the moment we are more interested in evaluating whether the signal is present in the data and whether the glitch can be misinterpreted as a signal. We want to have a figure of merit that would indicate our ability to recover whether the signal, the glitch, both or none had appeared in the data. This would give us a quantitative measure of the experiment outcome. At the same time we will show that we can infer the parameters of the signal and the glitch simultaneously if both are present. In the future the model can be easily generalised to multiple glitches increasing the computational complexity of the evidence calculation.

In the end, for the general model given by Eq. 9.21 we will be investigating 4 specific cases. First, the noise only model given by Eq. 9.19. Second, the model for the mixture of the noise with the signal specified in Eq. 9.20 Third, the model for the case of having only one glitch present in the data

$$\mathcal{G} : \tilde{x}_j = \tilde{g}_j + \tilde{n}_j. \tag{9.24}$$

And eventually the model for both signal and glitch present in the data

$$\mathcal{S} + \mathcal{G} : \tilde{x}_j = \tilde{s}_j + \tilde{g}_j + \tilde{n}_j. \tag{9.25}$$

We will be testing for all possible combinations of the models to see how in each case we can judge the outcome of the experiment. The Bayes Ratios that we are going to estimate are listed in the Table 6.

9.9 ARTIFICIAL DATA

Here we describe how we test the performance of the model selection on the artificially simulated data. We generate random realisations of data by drawing samples with parameters corresponding to the properties of our data from the Gaussian and *Student's t* distributions.

When the data is simulated as Gaussian noise, the generation of noise samples is done as described in Section 8.3. The only difference is that now the variance for each frequency bin is taken from the fit to the averaged ASD estimate for the OSTT test campaign data (see Fig. 62). The ASD is inferred from the data using the Welch algorithm [113, 81].

In addition to Gaussian noise, we repeat the analysis using *Student's t* distributed noise to test that our methods will perform equally well on this kind of data. The noise in this case is generated with a zero mean, a scale parameter s that equals the ASD for each separate frequency bin and with degrees-of-freedom $\nu = 20$. The value for the

$\frac{p(\{\tilde{x}\}\|\mathcal{S})}{p(\{\tilde{x}\}\|\mathcal{N})}$	$\frac{p(\{\tilde{x}\}\|\mathcal{G})}{p(\{\tilde{x}\}\|\mathcal{N})}$	$\frac{p(\{\tilde{x}\}\|\mathcal{S}+\mathcal{G})}{p(\{\tilde{x}\}\|\mathcal{N})}$
	$\frac{p(\{\tilde{x}\}\|\mathcal{G})}{p(\{\tilde{x}\}\|\mathcal{S})}$	$\frac{p(\{\tilde{x}\}\|\mathcal{S}+\mathcal{G})}{p(\{\tilde{x}\}\|\mathcal{S})}$
		$\frac{p(\{\tilde{x}\}\|\mathcal{S}+\mathcal{G})}{p(\{\tilde{x}\}\|\mathcal{N})}$

Table 6: The list of the Bayes Ratios that represent all possible combinations of the models studied in this work.

degrees-of-freedom is estimated from the fit of the *Student's t* cdf of the data from the test campaign (see Sec. 9.2).

9.10 STUDENT'S T LIKELIHOOD

The test campaign data that we have shows non-Gaussian features in its distribution (see Fig. 58). For this reason and because of the non-stationarities present in the noise, we cannot find a suitably long stretch of data to make an accurate estimate of the PSD. Therefore, we are going to adopt an approach that considers the variance of the noise as one of the parameters of the analysis, along with the signal parameters themselves. In this framework one writes the distribution for the noise variance and analytically integrates it out of the likelihood [87, 86, 85, 109]. The resulting likelihood follows the *Student's t* distribution instead of a Gaussian one. In addition, our knowledge about the noise PSD can be incorporated in the likelihood as a prior

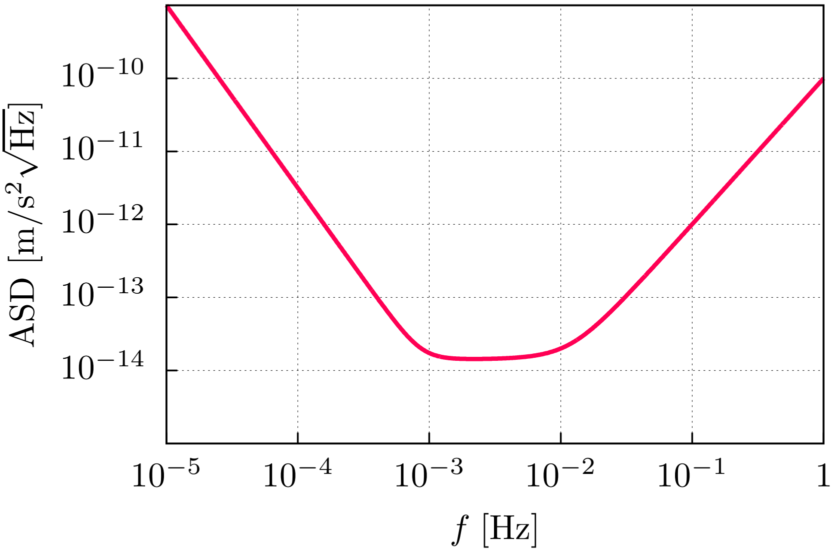

Figure 62: The noise curve estimated from the data from the test campaign, generated by fitting to the averaged ASD estimate

guess for the noise variance by determining its magnitude and the certainty with which we assume this magnitude to be known.

Therefore we treat the variance of the noise as a parameter and get a likelihood that follows a *Student's t* distribution as a result, which is consistent with the previous discussion that the noise of the real data is distributed according to the *Student's t* distribution, rather than to the Gaussian distribution.

9.10.1 *Prior for the variance*

When the noise variance is an unknown, the likelihood for the random variables $\{\tilde{x}\}$ can be written as a function of the variance parameters

$$p(\{\tilde{x}\}|\{\tilde{\sigma}^2\}) \propto \exp\left[-\sum_{j=0}^{N}(2\log(\tilde{\sigma}^2(f_j)) + \frac{|\tilde{x}_j|^2}{2\tilde{\sigma}_j^2})\right]. \tag{9.26}$$

In order for the variance to follow such distribution, the conjugate prior for the variance of each frequency bin has to be a scaled inverse χ^2 distribution [53]:

$$\sigma_j^2 \sim \mathrm{Inv}\chi^2(\nu_j, s_j^2), \tag{9.27}$$

where the parameters of this distribution are ν_j (the number of the degrees-of-freedom) and s_j^2 (the square of the scale parameter s). The expectation value and variance for the σ_j^2's are expressed in terms of the scale parameter and the number of degrees-of-freedom in the following way [87]

$$E[\sigma_j^2] = \frac{\nu_j}{\nu_j - 2} s_j^2 \tag{9.28}$$

and

$$\mathrm{Var}(\sigma_j^2) = \frac{2\nu_j^2}{(\nu_j-2)^2(\nu_j-4)} s_j^4, \tag{9.29}$$

therefore, the number of the degrees-of-freedom parameter has to be $\nu_j{>}4$ for both mean and variance to be finite.

9.10.2 *Marginalised likelihood*

Due to the use of the scaled inverse χ^2 distribution as a prior for σ^2 it is possible to integrate out the variance from the expression for the likelihood

$$p(\{\tilde{x}_j\}|\nu, s^2) = \prod_{j=0}^{N} \int_0^\infty p(\tilde{x}_j|\tilde{\sigma}_j^2) p(\tilde{\sigma}_j^2|\nu_j, s_j^2) d\tilde{\sigma}_j^2. \tag{9.30}$$

Following the derivations in [87] this expression for the likelihoods becomes

$$p(\{\tilde{x}_j\}|\nu, s^2) \propto \exp\left(-\sum_{j=0}^{N} \frac{\nu_j+2}{2} \log\left(1 + \frac{4|\tilde{x}_j|^2}{\nu_j s_j^2}\right)\right), \tag{9.31}$$

which gives us the expression of the product of *Student's t* pdfs. Therefore marginalising out the variance of the noise can be interpreted as assuming the *Student's t* distribution for the noise.

9.10.3 *Choice of the parameter values*

The parameters of the *Student's t* distribution can be expressed in terms of the expectation value and variance of the noise. The scale parameter is proportional to the expectation of the noise

$$s_j^2 = \frac{\nu_j - 2}{\nu_j} E[\sigma_j^2]. \tag{9.32}$$

Whereas the number of the degrees-of-freedom parameter is inversely proportional to the square of the error that we allow on our knowledge on the noise variance (in the limit of ν_j>4).

$$\nu_j = 4 + 2\frac{E[\sigma_j^2]^2}{Var(\sigma_j^2)}. \tag{9.33}$$

Therefore, we can define these parameters based on our prior knowledge about the noise. We will set the value of the scale parameters by taking the value of the PSD estimate in each, distinct frequency bin.

In the limit of $\nu \to \infty$, the marginalised likelihood [see Eq.(9.31)] tends to the Gaussian likelihood. Therefore the choice of the number of the degrees-of-freedom parameter indicates how close our likelihood will be to the Gaussian one. The smaller values of parameter ν mean more uncertainty on the knowledge of the noise PSD.

9.11 PERFORMANCE OF THE MODEL SELECTION

We are interested in testing our model selection approach. To verify its performance we generate data that has characteristics closely matched to the real world measurements from LPF. For this reason the noise will be generated following a *Student's t* distribution with the parameters that best fit the data. We will test whether it can be inferred as to what kind of model is buried in present within the data and how robust our inference is in choosing the relevant model.

For this purpose we generate 4 different data sets:

- $\tilde{d}_j = \tilde{n}_j$,
- $\tilde{d}_j = \tilde{s}_j + \tilde{n}_j$,
- $\tilde{d}_j = \tilde{g}_j + \tilde{n}_j$,
- $\tilde{d}_j = \tilde{s}_j + \tilde{g}_j + \tilde{n}_j$.

The data are constructed based on the set of models described in Sec. 9.8 that according to our current understanding, provide the most simple and interesting set of models for our experiment of the SP flyby. The models are compared to each other in pairs. This is done using Bayes Factors described in Sec. 9.8.

We then investigate how well each model describes each of the predefined datasets with the following set of models:

- $\tilde{h}_j = 0$,
- $\tilde{h}_j = \tilde{s}_j$,
- $\tilde{h}_j = \tilde{g}_j$,
- $\tilde{h}_j = \tilde{s}_j + \tilde{g}_j$.

The Bayes Factor compares two models with each other and evaluates which one of them better describes the data. We will compare each model with the other one, therefore estimating 6 Bayes Factors for one dataset.

For each dataset we will estimate the Bayes Factors based on Gaussian (see Eq. 9.34) and *Student's t* (see Eq. 9.35) log-likelihood functions. The argument of the likelihood function $\tilde{x}_j = \tilde{d}_j - \tilde{h}_j(\theta)$ differs depending on the model that we are testing and the dataset that we are using.

The expression for the Gaussian log-likelihood of the data $\tilde{d}$ and depending on the model $\tilde{h}(\theta)$ is

$$\log L_G \propto -\sum_{j=1}^{N} \frac{|\tilde{d}_j - \tilde{h}_j(\theta)|^2}{2\tilde{\sigma}^2}. \tag{9.34}$$

The expression for the *Student's t* log-likelihood of the data $\tilde{d}$ and depending on the model $\tilde{h}(\theta)$ is

$$\log L_t \propto -\sum_{j=0}^{N} \frac{\nu_j+2}{2} \log\left(1 + \frac{4|\tilde{d}_j - \tilde{h}_j(\theta)|^2}{\nu_j s_j^2}\right). \tag{9.35}$$

The simulated datasets were produced in the following way. For 100 random noise realisations of the *Student's t* distributed noise an instance of the signal, glitch or both were injected in the noise. The values of the parameters for the glitch (see Sec. 9.6) and signal (see Sec. 9.7) models that were injected in the data were generated randomly within their prior ranges. For each of 100 different noise realisations the evidence was calculated by integrating the joint probability over all parameters of the models.

In Table 7 we show all possible combinations of the datasets and models and give reference to the plots that show the resulting distributions of the Bayes Factors for the different datasets.

We estimate the values of the Bayes Factors for each combination of models. This represents a measure of how one model is more plausible than the other without any knowledge on the prior model probabilities. For testing the performance of the model selection on our data we make a distribution of the Bayes Factors for each dataset and each pair of models. In this setup to evaluate which model is preferred to the other one, we calculate the Bayes Factors ratios that are greater than 1 relative to the overall number of simulations. This gives probability with which one model describes data better than the other one. Though the Bayes Factor estimate provides us with a comprehensive information on the comparison between the models, it is sometimes useful to have a definitive threshold that would allow us to say whether one model or another describes the data better. The common approach to answer this question is by using Jeffreys criterion [67], that says, for example, that in the case when B_{12}>10 there is strong confidence that the model $\mathcal{M}_1$ is preferred to the model $\mathcal{M}_2$. This can be used for the data received from experiment, when we have one measurement and will have to make a conclusion based on this measurement. At the same time the distributions of the Bayes Factors and the probabilities that say which model is preferred to the other one give us insight into how the Bayes Factor varies with different realisations.

Table 7: Simulations where run for all possible combinations of data and signal models. The results of the Bayes Factor distributions are presented in the Figures that are given in this table

		Data			
		$\tilde{d}_j = \tilde{n}_j$	$\tilde{d}_j = \tilde{s}_j + \tilde{n}_j$	$\tilde{d}_j = \tilde{g}_j + \tilde{n}_j$	$\tilde{d}_j = \tilde{s}_j + \tilde{g}_j + \tilde{n}_j$
Model	$\tilde{h}_j = 0$	see Fig. 63	see Fig. 64	see Fig. 65	see Fig. 66
	$\tilde{h}_j = \tilde{s}_j$				
	$\tilde{h}_j = \tilde{g}_j$				
	$\tilde{h}_j = \tilde{s}_j + \tilde{g}_j$				

In Figs. 63, 64, 65, 66 the distributions of the log-Bayes Factors are plotted for the different datasets. The threshold based on Jeffreys criterion is plotted vertically as a reference at $\log B_{12} = \log(10)$ to allow comparison with the Bayes Factor distributions.

9.11.1 *Bayes Factor distributions for data with only noise present* $\tilde{d}_j = \tilde{n}_j$

The results are presented for different datasets. Let us start with the $\tilde{d}_j = \tilde{n}_j$, the case when only noise is present in the data. The distributions of the log-Bayes Factors are shown in Fig. 63. These are calculated for both Gaussian and *Student's t* log-likelihoods. Each plot presents a comparison of two models.

On the first panel with the title "S/N" (Fig. 63), the distribution of the Bayes Factors for $B_{\mathcal{S}\mathcal{N}} = p(\{\tilde{x}\}|\mathcal{S})/p(\{\tilde{x}\}|\mathcal{N})$ is plotted. We can see that the span of the Bayes Factors is not very broad and the distributions peak around -3. The plot shows us that in this case the noise model ($\mathcal{N}$) is preferred to the signal model ($\mathcal{S}$). The measure of how much one model is preferred to the other can be described by the fraction of the log-Bayes Factors greater than the threshold (zero in our case), normalised by the overall number of realisations. This can be seen as a probability, marginalised over noise realisations, that the data was generated from the model $\mathcal{M}_1$ rather than the model $\mathcal{M}_2$ if the Bayes Factor is defined as $p(\{\tilde{x}\}|\mathcal{M}_1)/p(\{\tilde{x}\}|\mathcal{M}_2)$. The results are presented in the table 8a. The probability $P(B_{\mathcal{S}\mathcal{N}}>1) \sim 0.03$ means that there is a 3% chance that the data composed from the noise only will be misinterpreted as a signal. At the same time it means that with 97% probability we will be able to say that the noisy data has only noise in it and does not have any signal.

On the next panel, labeled "G/N" (Fig. 63), the results for glitch versus noise models are presented. The probability (see table 8a) that we can misinterpret the data as a glitch when there is only noise present is $P(B_{\mathcal{G}\mathcal{N}}>1) \sim 0.01$. This means that with a probability of 99% we can correctly determine glitch from the noise.

The next panel "S+G/N" (Fig. 63) tells us that in the case that we compare the noise model to the model that suggests that the data is a mixture of the noise, signal and a glitch, all Bayes Factors will be below zero. That defines the probability $P(B_{(\mathcal{S}+\mathcal{G}),\mathcal{N}}>1) \sim 0$ (table 8a), which states that in 100% cases we can conclude that these data favour the noise model as opposed to the signal, glitch, noise mixture model.

Panel "G/S" (Fig. 63) shows the Bayes Factors in the case when one model suggests that there is signal in the data and the other suggests that there is glitch in that data. We can see that the Bayes Factor peaks at a negative values and the probability of the signal model to be preferred over glitch model is $P(B_{\mathcal{G}\mathcal{S}}>1) \sim 0.21$ (table 8a). This is an expected result because the glitch model is parameterised with 5 parameters, whereas the signal model has only 2. The Bayes Factor defined through the integral of the joint probabilities over all parameters will panellise unnecessarily complicated models. It will not be a problem when the model correctly describes the data, however in the case when both models equally well or equally badly describe the data it will prefer the simpler one.

Next panel "S+G/S" (Fig. 63) presents the results for the case when the signal model is compared to the mixture of the signal with the glitch model with $P(B_{(\mathcal{S}+\mathcal{G}),\mathcal{S}}>1) \sim 0.01$ (table 8a). Such a small probability for the signal with glitch model indicates again that the model with less parameters is preferred to more complicated model.

The distribution for the last Bayes Factor computed for this data is shown on the panel "S+G/G" (Fig. 63) and it displays the similar results as the previous case. This time the probability that this type of data is described by signal plus glitch model versus only glitch model is $P(B_{(\mathcal{S}+\mathcal{G}),\mathcal{G}}>1) \sim 0.03$ and the method also prefers simpler model.

Fig. 63 and table 8b provide results for the same data for the Gaussian likelihood (calculated for the *Student's t* noise). When only noise is present in the data the results are almost identical. However for the dataset that we will consider later, when signal, glitch or both were injected, the Bayes Factors for Gaussian likelihood have unexpectedly large outliers. These outliers, however, do not significantly change the fraction of Bayes Factors above the detection threshold. The results are, thus, consistent with the ones from the *Student's t* likelihoods, but are less robust. That is why they are excluded for now from the results of this work.

9.11.2 *Bayes Factor distributions for data with a signal present* $\tilde{d}_j = \tilde{s}_j + \tilde{n}_j$

Let us consider the model for the data, when it is a mixture of noise and signal $\tilde{d}_j = \tilde{s}_j + \tilde{n}_j$. Fig. 64 displays the Bayes Factor distributions for this case. On the first panel with the title "S/N" the results for the signal against noise model are shown. The probability that the data prefers the signal model (see table 9) is $P(B_{\mathcal{S}\mathcal{N}}>1) \sim 0.89$ versus the noise only model. This agrees well with the dataset that was simulated.

On the next panel "G/N" the results are presented for the case of the glitch when compared with the noise model. The probability that the glitch is preferred over noise is $P(B_{\mathcal{G}\mathcal{N}}{>}1) \sim 0.44$ (see table 9) which means that in this case it is more probable that the data is just Gaussian noise, however, this statement is not very strong. Moreover this result indicates that our approach will be rather robust against glitches. Though for some choice of parameters, glitches can be misinterpreted as a signal (see Sec. 9.1), in most cases it can be distinguished from the signal.

When the model where both signal and glitch are present in the data is compared with the noise model, which is shown on a panel "S+G/N", data containing a signal together with a glitch is prioritised over the noise model $P(B_{(\mathcal{S}+\mathcal{G}),\mathcal{N}}{>}1) \sim 0.81$ (table 9).

Nevertheless to see whether the dataset favours the signal or a glitch we have to compare those two models separately, which is shown on the panel "G/S" in Fig. 64. It shows that with 99% probability this was a signal rather then a glitch $P(B_{\mathcal{G}\mathcal{S}}{>}1) \sim 0.01$ (table 9), which is a very encouraging result.

On the next panel "S+G/S" we compare the signal with glitch model to the signal only model (Fig. 64). The signal model is in all realisations preferred to the mixture of the signal with the glitch model (table 9) $P(B_{(\mathcal{S}+\mathcal{G}),\mathcal{S}}{>}1) \sim 0$.

Finally, when the signal plus glitch model is compared to the glitch only model "S+G/G" the mixture of the signal and a glitch is chosen to be a preferable model with a probability $P(B_{(\mathcal{S}+\mathcal{G}),\mathcal{G}}{>}1) \sim 0.89$.

9.11.3 *Bayes Factor distributions for data with a glitch present* $\tilde{d}_j = \tilde{g}_j + \tilde{n}_j$ *and a mixture of signal and glitch* $\tilde{d}_j = \tilde{s}_j + \tilde{g}_j + \tilde{n}_j$.

In the next set of results we are most interested in the comparisons of the signal and glitch, when one of them or both are present in the data. This is the most important question of this study, which should define how well the signal can be distinguished from the instrument's noise artefacts.

In Fig. 65 and the corresponding table 10 the results for the case where the glitch is present in the data are shown. Moreover, we present the results for the case where the mixture of signal and glitch are present in the data. The results for this data are shown in Fig 66 and table 11. The conclusions that we can draw from these Bayes Factor distributions are consistent with the models that are injected in the data and follow the logic described in Secs. 9.11.1, 9.11.2.

$P(B_{\mathcal{S}\mathcal{N}}>1)$	$=0.03$
$P(B_{\mathcal{G}\mathcal{N}}>1)$	$=0.01$
$P(B_{(\mathcal{S}+\mathcal{G}),\mathcal{N}}>1)$	$=0$
$P(B_{\mathcal{G}\mathcal{S}}>1)$	$=0.21$
$P(B_{(\mathcal{S}+\mathcal{G}),\mathcal{S}}>1)$	$=0.01$
$P(B_{(\mathcal{S}+\mathcal{G}),\mathcal{G}}>1)$	$=0.03$

(a) Bayes Factors are calculated with the *Student's t* likelihood.

$P(B_{\mathcal{S}\mathcal{N}}>1)$	$=0.04$
$P(B_{\mathcal{G}\mathcal{N}}>1)$	$=0.01$
$P(B_{(\mathcal{S}+\mathcal{G}),\mathcal{N}}>1)$	$=0$
$P(B_{\mathcal{G}\mathcal{S}}>1)$	$=0.17$
$P(B_{(\mathcal{S}+\mathcal{G}),\mathcal{S}}>1)$	$=0.01$
$P(B_{(\mathcal{S}+\mathcal{G}),\mathcal{G}}>1)$	$=0.04$

(b) Bayes Factors are calculated with the Gaussian likelihood.

Table 8: Probabilities for one model to be preferred over the other one. Results for the data with only noise present $\tilde{x}_j = \tilde{n}_j$.

$P(B_{\mathcal{S}\mathcal{N}}>1)$	$=0.89$
$P(B_{\mathcal{G}\mathcal{N}}>1)$	$=0.44$
$P(B_{(\mathcal{S}+\mathcal{G}),\mathcal{N}}>1)$	$=0.81$
$P(B_{\mathcal{G}\mathcal{S}}>1)$	$=0.01$
$P(B_{(\mathcal{S}+\mathcal{G}),\mathcal{S}}>1)$	$=0$
$P(B_{(\mathcal{S}+\mathcal{G}),\mathcal{G}}>1)$	$=0.89$

Table 9: Probabilities for one model to be preferred over the other one. Results for the data with the signal in noise $\tilde{x}_j = \tilde{s}_j + \tilde{n}_j$. Bayes Factors are calculated with the *Student's t* likelihood.

$P(B_{\mathcal{S}\mathcal{N}}>1)$	$=0.35$
$P(B_{\mathcal{G}\mathcal{N}}>1)$	$=0.91$
$P(B_{(\mathcal{S}+\mathcal{G}),\mathcal{N}}>1)$	$=0.91$
$P(B_{\mathcal{G}\mathcal{S}}>1)$	$=0.93$
$P(B_{(\mathcal{S}+\mathcal{G}),\mathcal{S}}>1)$	$=0.91$
$P(B_{(\mathcal{S}+\mathcal{G}),\mathcal{G}}>1)$	$=0.22$

Table 10: Probabilities for one model to be preferred over the other one. Results for the data with the glitch in noise $\tilde{x}_j = \tilde{g}_j + \tilde{n}_j$. Bayes Factors are calculated with the *Student's t* likelihood.

$P(B_{\mathcal{S}\mathcal{N}}>1)$	$=0.77$
$P(B_{\mathcal{G}\mathcal{N}}>1)$	$=0.98$
$P(B_{(\mathcal{S}+\mathcal{G}),\mathcal{N}}>1)$	$=0.98$
$P(B_{\mathcal{G}\mathcal{S}}>1)$	$=0.85$
$P(B_{(\mathcal{S}+\mathcal{G}),\mathcal{S}}>1)$	$=0.91$
$P(B_{(\mathcal{S}+\mathcal{G}),\mathcal{G}}>1)$	$=0.82$

Table 11: Probabilities for one model to be preferred over the other one. Results for the data with the signal and the glitch in noise $\tilde{x}_j = \tilde{s}_j + \tilde{g}_j + \tilde{n}_j$. Bayes Factors are calculated with the *Student's t* likelihood.

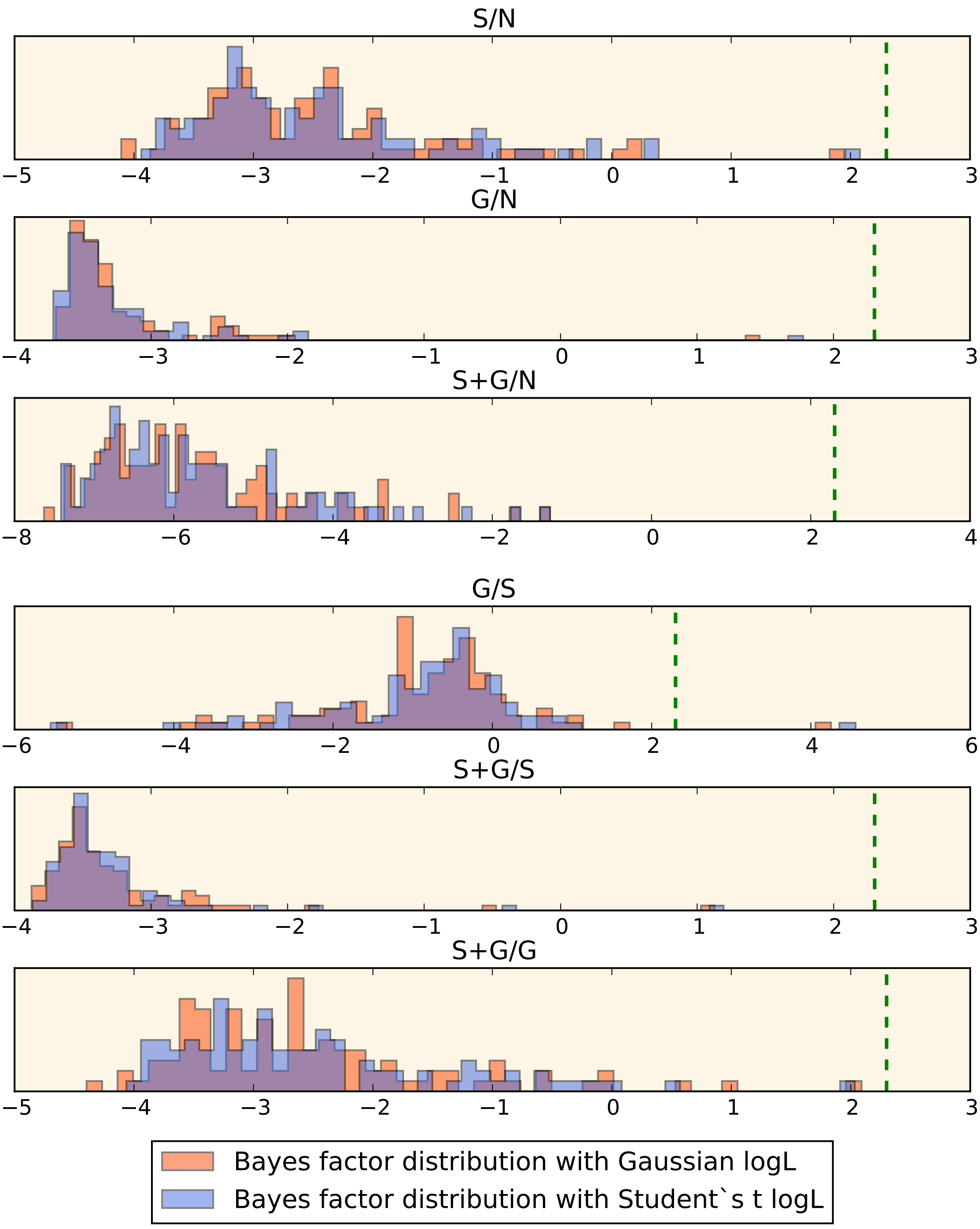

Figure 63: The distribution of the log Bayes factors for the case of the data N.

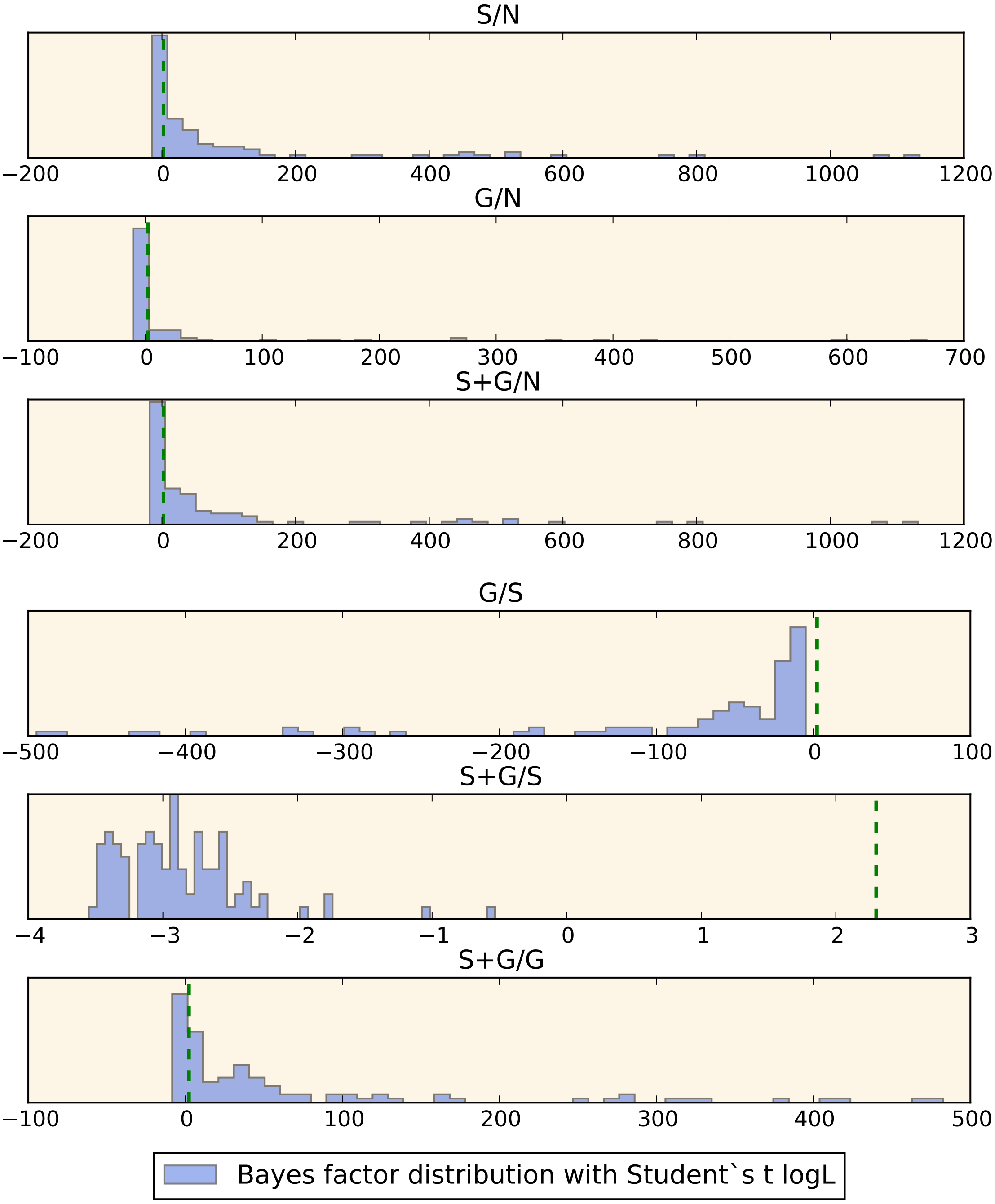

Figure 64: The distribution of the log Bayes factors for the case of the data $S + N$

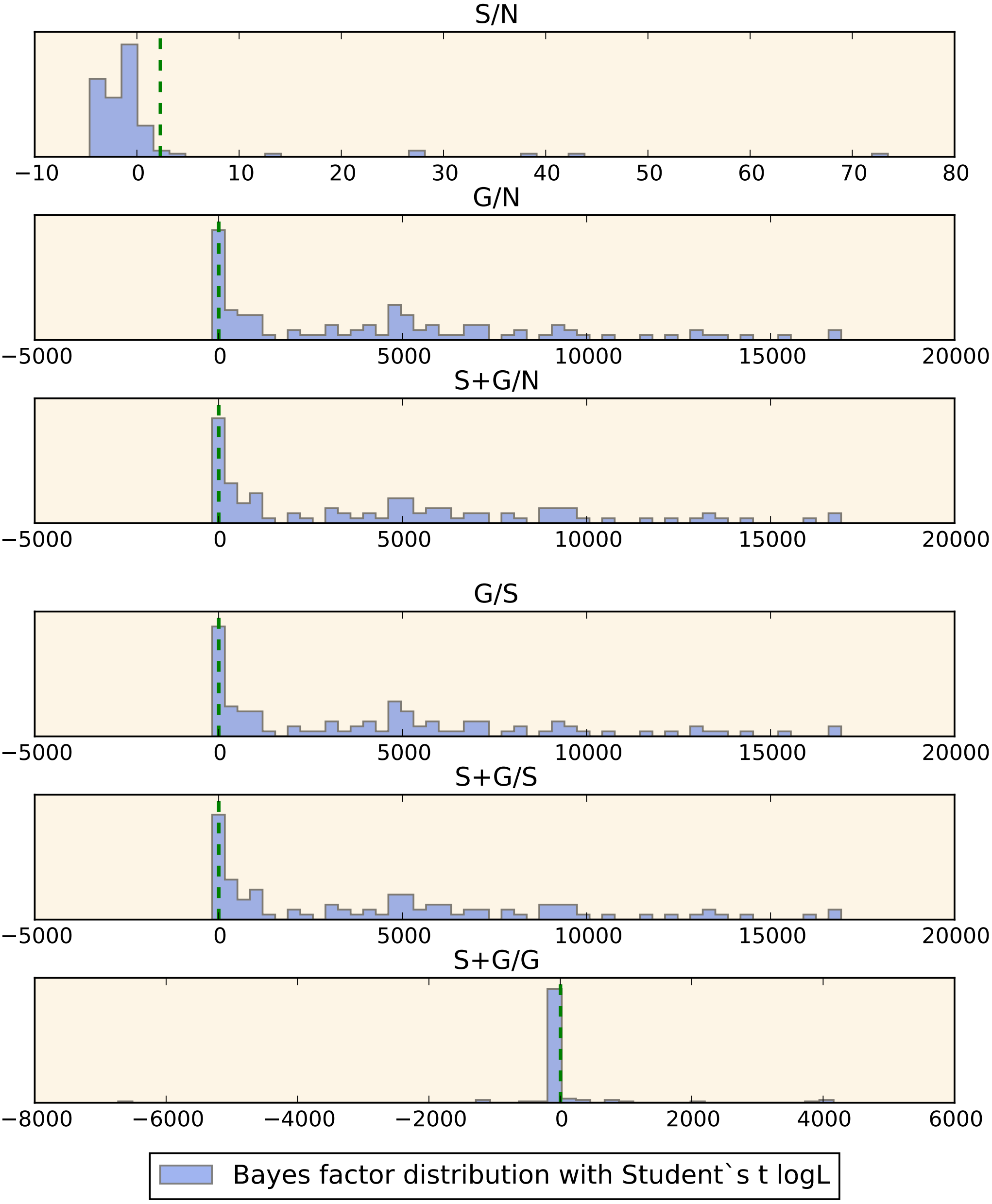

Figure 65: The distribution of the log Bayes factors for the case of the data G + N

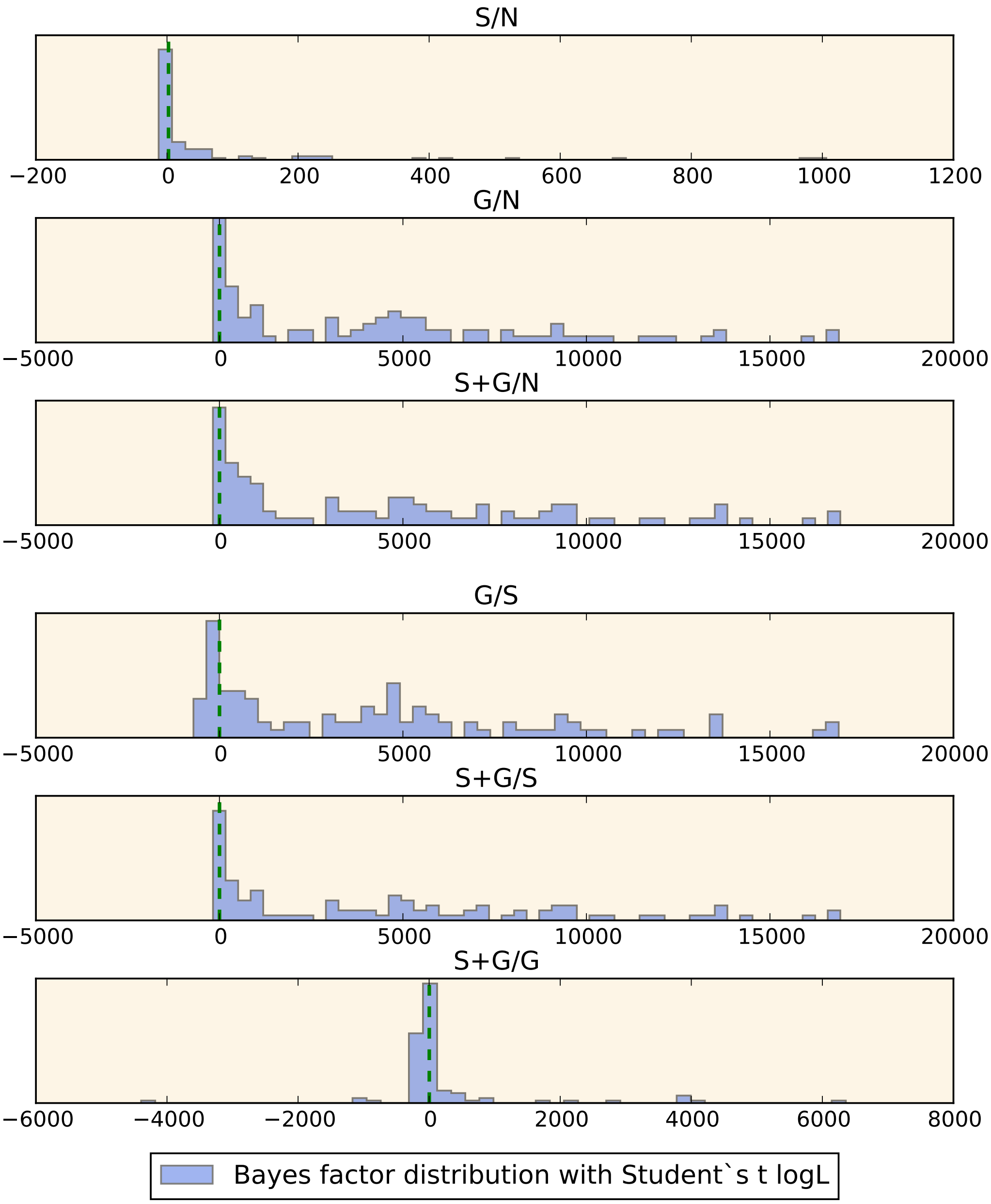

Figure 66: The distribution of the log Bayes factors for the case of the data $S+G+N$

9.12 PARAMETER ESTIMATION FOR GLITCHES AND SIGNALS

Together with the calculation of the Bayes Factors we also get estimates of the model parameters. Here we only present a set of results to illustrate the parameter estimation performance and to show how well parameter values are recovered for different models injected in the data.

We present the results for one random noise realisation. The signal, glitch and the mixture of the signal with the glitch models were injected at the following randomly chosen parameter values.

Parameters for the signal generated for this noise realisation are

$$\begin{aligned} A_s &= 1.7 \cdot 10^{-9} \text{ [m]}, \\ \Gamma &= 73.67 \text{ [s]}. \end{aligned}$$

Parameters for the glitch generated for this noise realisation are

$$\begin{aligned} \phi_0 &= 5.33 \text{ [rad]}, \\ A_g &= 3.57 \cdot 10^{-10} \text{ [m/s}^2\text{]}, \\ f_0 &= 0.06 \text{ [Hz]}, \\ Q &= 3.93, \\ t_0 &= 275.40 \text{ [s]}, \end{aligned}$$

Parameters for the mixture of the signal and glitch generated for one this noise realisation:

$$\begin{aligned} \phi_0 &= 5.33 \text{ [rad]}, \\ A_g &= 3.58 \cdot 10^{-10} \text{ [m/s}^2\text{]}, \\ f_0 &= 0.06 \text{ [Hz]}, \\ Q &= 3.93, \\ t_0 &= 275.40 \text{ [s]}, \\ A_s &= 1.06 \cdot 10^{-9} \text{ [m]}, \\ \Gamma &= 111.77 \text{ [s]}. \end{aligned}$$

	mean	standard deviation
A_s	$1.57 \cdot 10^{-9}$	$0.739 \cdot 10^{-10}$
Γ	69.879	1.988

Table 12: Results of the parameter estimation for the generalised signal model. The mean and the standard deviation of the posterior probabilities of the parameters are presented.

	mean	standard deviation
ϕ_0	5.33	$0.58 \cdot 10^{-3}$
A_g	$3.575 \cdot 10^{-10}$	$0.233 \cdot 10^{-12}$
f_0	0.064	$0.174 \cdot 10^{-4}$
Q	3.935	$0.581 \cdot 10^{-3}$
t_0	275.405	$0.219 \cdot 10^{-2}$

Table 13: Results of the parameter estimation for the glitch model. The mean and the standard deviation of the posterior probabilities of the parameters are presented.

The results for the posterior parameters estimates are presented in the following plots: the generalised signal model in Fig. 67, the glitch model in Fig. 68 and the signal with the glitch model in Fig. 69. The errors on the recovered parameters are given in Tables 12, 13 and 14. One can see that for this particular noise realisation the true values of parameters lie within their posterior distributions.

	mean	standard deviation
ϕ_0	533	$0.57 \cdot 10^3$
A_g	$3.577 \cdot 10^{-10}$	$0.227 \cdot 10^{-12}$
f_0	0.064	$0.171 \cdot 10^{-4}$
Q	3.934	$0.578 \cdot 10^3$
t_0	275.400	$0.223 \cdot 10^{-2}$
A_s	$1.087 \cdot 10^8$	$0.172 \cdot 10^{-9}$
Γ	117.087	10.404

Table 14: Results of the parameter estimation for the mixture of the generalised signal and glitch models. The mean and the standard deviation of the posterior probabilities of the parameters are presented.

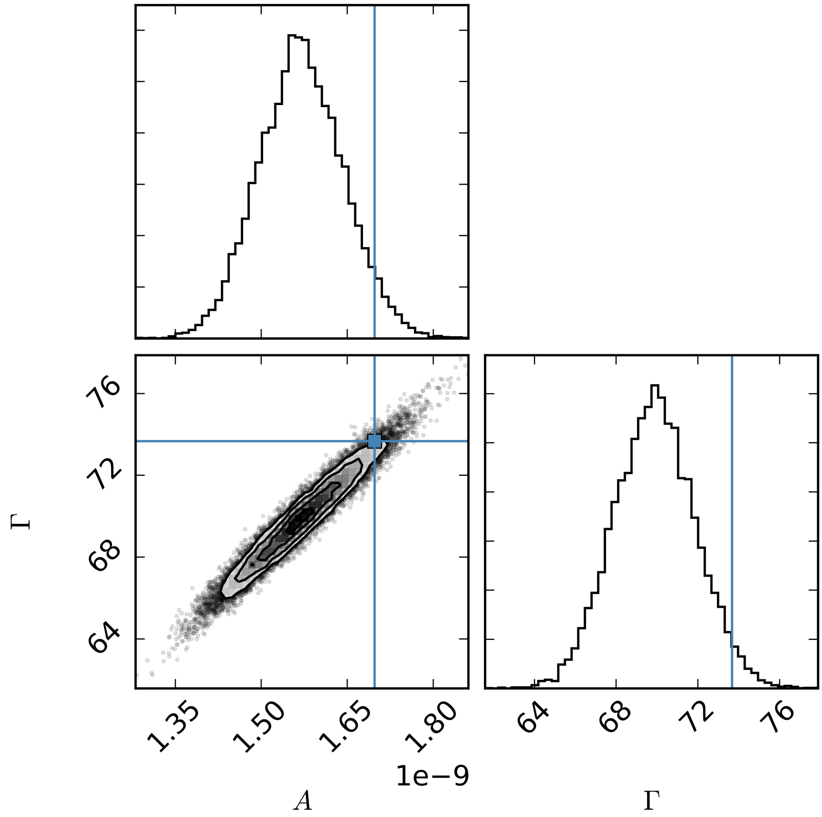

Figure 67: Posterior distribution contour plots for data and model assuming the generalised signal model. The contours contain 2.5 %, 16 %, 84 % and 97.5 % of the probability. The lines for each parameter indicate the location of the true values that were injected into simulated data.

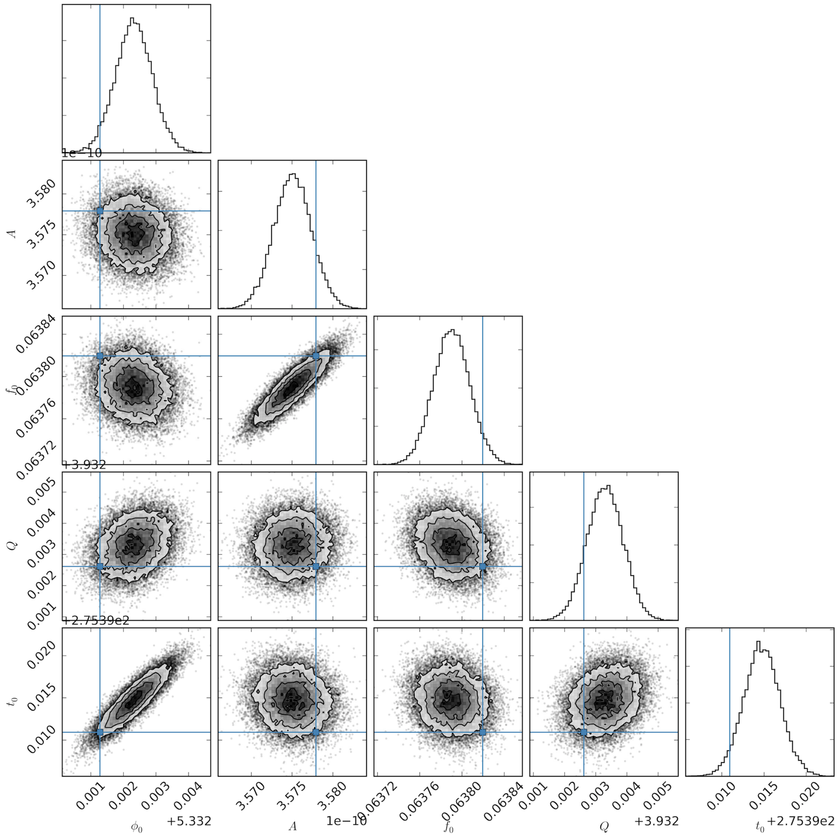

Figure 68: Posterior distribution contour plots for the data and model assuming the glitch model. The contours contain 2.5 %, 16 %, 84 % and 97.5 % of the probability. The lines for each parameter indicate the location of the true values that were injected into simulated data.

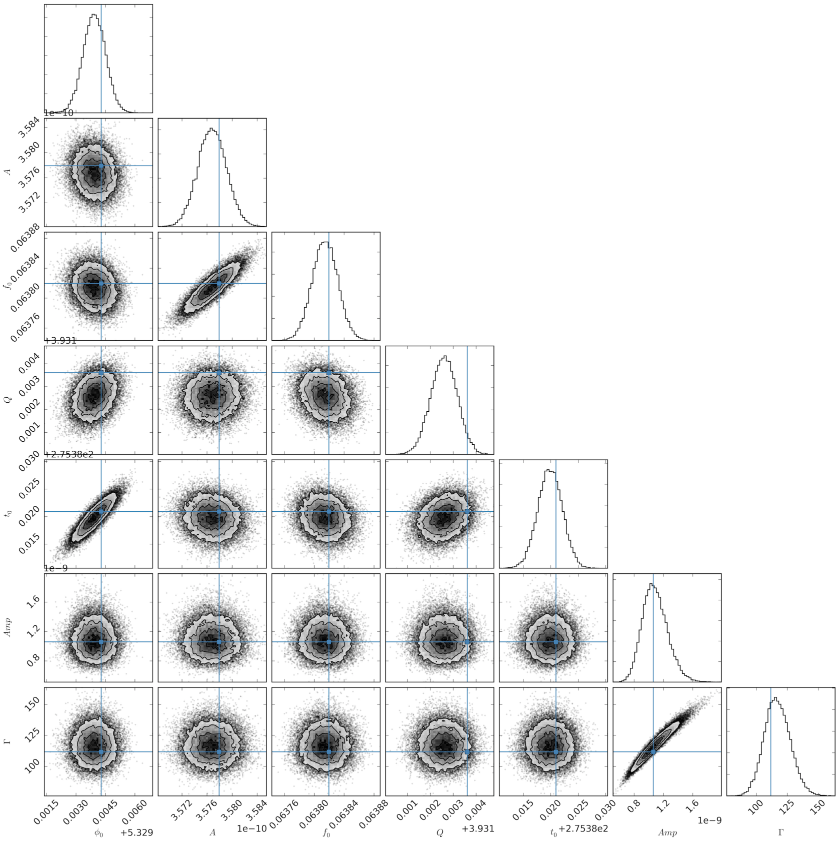

Figure 69: Posterior distribution contour plots for the data and model assuming the mixture of the generalised signal and glitch models. The contours contain 2.5 %, 16 %, 84 % and 97.5 % of the probability. The lines for each parameter indicate the location of the true values that were injected into simulated data.

9.13 CONCLUSIONS ON THE MODEL SELECTION

We have investigated the issue of the outliers in the LPF data. This question was provoked by the glitches that appear in the test campaign measurements for LPF. Combined with the conditions of the SP experiment (which will happen only once or possibly twice) the ability to distinguish the signal from the glitch becomes very important.

To extract information about LPF noise we have shown how we can convert the data to the acceleration measurement and add the noises from the other subsystems of the spacecraft that were not measured during the test campaign. Using the insight provided by this data, we have constructed artificial data that has the characteristics closest to the real world data.

To test our ability to distinguish a glitch from the signal we defined two models, one for the signal and one for the glitch. The signal model was constructed by making the simplest parameterised model based on the waveforms that we have from the numerical simulations for the T*e*V*e*S theories. We have mapped the parameter space of signals produced from numerical simulations to the parameter space of a generalised model. However the new parameter space now covers a broader range of models.

The glitch model was motivated by the test campaign data and by the experience with the ground based detectors that use similar kind of models. We used a sine-Gaussian model for a glitch.

For these two models, for the combination of a glitch with a signal and for the noise generated from the *Student's t* distribution we have performed model selection that is reliant on a Bayesian approach to data analysis. The estimated distributions of the Bayes Factors show that we have a very high chance of distinguishing the signal from the glitch. For example, the probability that the glitch will be misinterpreted as a signal is only 7%. This value was calculated by integrating over the whole parameter space. However in the future we plan to extend this study by finding a particular subspace of the signal parameters that are prone to being misleadingly fit to glitches in the data.

There remain a number of important studies that must be performed during the flight of LPF.

- We have to derive the optimal value for ν in the *Student's t* likelihood based on the test campaign data. It could be done, for example, by finding the maximum of the likelihood function as a function of the number of degrees-of-freedom parameter. This is equivalent to performing Bayesian model selection on the discrete set of models defined by ν.
- We need to estimate the frequency of glitches (the glitch rate) that would give us an estimate for the number of glitches that we can expect during the SP flyby.
- We must identify a prior parameter space on the glitch model that better describes the glitches in the real flight data. Moreover, we plan to investigate the feasibility of applying unsupervised machine learning algorithms which would ultimately estimate the glitch distribution and rate based on actual LPF data prior to the flyby.

Part V

CONCLUSIONS AND FUTURE PLANS

10

CONCLUSIONS AND FUTURE PLANS

10.1 DATA ANALYSIS FRAMEWORK FOR MISSION EXTENSION

In this thesis we have developed a data analysis framework for the mission extension of LPF. We study the signal that will be measured by LPF. First, we have looked at the parameterisation of the signal in terms of the spacecraft trajectory and its relative position to the SP. It was concluded that the precision of our knowledge on the errors of the trajectory parameters will increase once the navigation is performed. This precision would be good to the extent that these parameters can be fixed as known once we know the trajectory that has been used. This allows us, during the experiment, to disentangle the study of the measured signal from the uncertainty on the trajectory parameters.

Prior to the mission extension it has to be shown that valuable results can be obtained from the LPF measurement. This is demonstrated for one example of a theoretical prediction for a signal that could be measured around the SP. The impact of two possible outcomes was presented. First, the case where there is a signal present in the data. It was shown how well we would be able to estimate the parameters of this signal. Second, and most important, in the case that we have no signal. It was demonstrated how this measurement will be useful in ruling out a subspace of alternative theories of gravity.

The major concern for this experiment was always that it might be contaminated by spurious noise signals which can be misinterpreted as the measurement of a real gravity field. We have investigated this problem by proposing a model for the glitch based on real world data from a test campaign. The conclusion of this study is that we are able to distinguish the signal from the glitch with the high probability. Moreover, alongside this study we proposed a generalised model of the signal that will be useful in parameterising the stress tensor measurement and then mapping this measurement on to the parameter spaces of various theories.

10.2 FUTURE WORK

We need to put the SP flyby results in correspondence with the measurements and restrictions from other experiments.

10.2.1 *Observations of the planetary motions in the Solar System*

The observations of the planetary motions in the Solar System give very tight constraints on deviations from GR [80, 101].

The gravitational forces from the bodies in the Solar System can be written in a form

$$\ddot{\mathbf{r}}_i = \sum_{j \neq i} \frac{\mu_j (\mathbf{r}_j - \mathbf{r}_i)}{r_{ij}^3} + C_1 + C_2 + C_3, \qquad (10.1)$$

where C_1 are the relativistic corrections (in parameterised post-Newtonian approximation), C_2 are the components that come from the ellipticity of the Sun, and C_3 are the contributions from the small Solar System bodies. Here $\mathbf{r}_i$ and $\ddot{\mathbf{r}}_i$ are the solar-system-barycentric position and acceleration of the body i; $\mu_j = Gm_j$, where m_j is the mass of the body j and G is the gravitational constant; and $r_{ij} = |\mathbf{r}_j - \mathbf{r}_i|$. We can add additional components into equation 10.1 that will be responsible for modifications of the gravity at small gravitational accelerations and see how this additional component should influence the observations. The constraints imposed by the observation of the dynamics of the bodies in the Solar System will impose the constraint on the additional component in the equation of the Solar System dynamics.

10.2.2 *Pulsar timing tests*

Recent observations of the relativistic pulsar-white dwarf binary [51] impose very tight constraints on the deviations of gravity theories from GR. They also cover the class of the theories that we are interested in.

As was discussed in Sec. 2.2, the metric of those theories is coupled into the physical metric as follows

$$\begin{aligned} g_{00} &\equiv A^2(\phi) g^*_{00} \\ g_{ij} &\equiv A^{-2}(\phi) g^*_{ij}. \end{aligned} \tag{10.2}$$

In [51] it is proposed that $A(\phi)$ is expanded around the background value of the additional scalar potential

$$A(\phi) = \ln A(\phi_0) + \alpha_0(\phi - \phi_0) + \frac{1}{2}\beta_0(\phi - \phi_0)^2 + \ldots, \tag{10.3}$$

where α_0 is the linear and β_0 is the quadratic matter-scalar coupling. The restriction from the observations of the pulsars are imposed on these two constants. The values for these constants in GR are $\alpha_0 = \beta_0 = 0$. We need to cast these two parameters into the parameter space that defines our signal and see which constraints they impose on it.

Part VI

APPENDIX

A

DEFINITION OF THE FOURIER TRANSFORM

In this thesis the convention for the Discrete Fourier Transform (DFT) is the following

$$\tilde{x}_j = \sum_{j=0}^{N-1} x_j \exp(-2\pi\sqrt{-1}jk/N)\Delta t \tag{A.1}$$

where N is the number of samples in the time series and Δt is the sampling frequency.

LIST OF FIGURES

Figure 1 Field lines of the stress tensor from an oscillating gravitational wave 12
Figure 2 Plus polarisation 13
Figure 3 Cross polarisation 13
Figure 4 Figure taken from [63]. Measurements of the pulsar period, over several orbital periods. Pulsar radial velocity was calculated from the doppler shift. 20
Figure 5 Figure taken from [112]. Schematic representation of the orbits of the binary system of the neutron stars inferred from the observation of the pulsar. 20
Figure 6 Figure taken from [111]. Accumulated orbit phase error with the assumption that P_b had a fixed error at 1974.7 with $\dot{P}_b = 0$. 21
Figure 7 The scheme that represent the principle of the resonant detector. The space stretches due to the gravitational wave to $\xi = x_2 - x_1 - l_0$. 27
Figure 8 Resonant detectors 28
Figure 9 Sensitivities of Explorer and Nautilus detectors. The plot is taken from [14]. 28
Figure 10 Michelson interferometer. It measures the difference in the lengths of the arms as $\delta\varphi$. 30
Figure 11 Ground based detectors 38
Figure 12 Noise curves for laser interferometer detectors. This Figure is taken from [38]. 39
Figure 13 Scheme of the LISA constellation. Figure is taken from [64]. 39
Figure 14 Schematic representation of the LISA orbits. 40
Figure 15 LISA and eLISA sensitivities. This plot is taken from [11]. 40

Figure 16 Two test masses following geodesics 52
Figure 17 Definition of the LPF coordinates 52
Figure 18 LPF interferometers 53
Figure 19 Timeline of the LPF mission. 54
Figure 20 The transit of the spacecraft to L1 and Lissajous orbits around L1 54
Figure 21 LPF 55
Figure 22 Galaxy NGC 3198 61
Figure 23 Contribution to the overall noise from the different noise sources. The figures are taken from [12]. 70
Figure 24 LPF sensitivity. Amplitude spectral densities of the requirements and the current best estimate noise. 71
Figure 25 Location of the SP relative to the Sun, Earth and L_1. The Figure is not to scale (Pictures of the Earth and the Sun courtesy of ESA). 72
Figure 26 Trajectories of the double SP flyby. The figure is taken from [41]. 73

Figure 27 Schematic of the trajectory parameters. The coordinate system has its origin in the SP (S) and the x-axis is parallel to the line joining the Sun and the Earth and pointing in the direction of the Sun. The z-axis is perpendicular to the ecliptic and the spacecraft velocity $\mathbf{v}$ is aligned with the trajectory. The direction of the trajectory is defined by the two angles η (the angle between the z-axis and $\mathbf{v}$) and φ (the angle between x-axis and projection of $\mathbf{v}$ on the (x, y) plane, shown as the segment OD). The position of the spacecraft along the trajectory is determined by the variable r, the distance to the point A where the perpendicular dropped on the trajectory intersects with it. The length of the perpendicular is given by the parameter $\|\xi\|$. The position of the perpendicular is given by two angles, $\eta_\perp$ (the angle between the z-axis and the perpendicular) and $\varphi_\perp$ (the angle between the x-axis and the projection of the perpendicular on the (x, y) plane, segment BS). 75

Figure 28 Comparison between the interpolating function used for the numerical calculations and the one originally proposed in [16]. 80

Figure 29 Comparison between a template produced with a numerical calculation and the rescaled Newtonian background analytically estimated using Eq. (6.11). In this example, $k = 0.03$ and $a_0 = 10^{-10}\,\mathrm{m/s^2}$. The $\partial\Phi^2/\partial z^2$ and $\partial\Phi_N^2/\partial z^2$ components of the MONDian and Newtonian stress tensors are plotted. This means that the sensitive axis is parallel to the z-axis of the coordinate system and, therefore, that $\beta = 0$. 82

Figure 30 Fraction of trajectories n with SNR value specified on the horizontal axis. The SNR was calculated using 1000 trajectories with randomly varied parameters for both the current best noise estimate and the requirements noise. The parameter values were uniformly sampled over the ranges given in the last column of Table 3. The curves are the Gaussian fits to the discrete distributions that were obtained. 90
Figure 31 SNR as a function of the orientation angle of the sensitive axis β for the two noise realizations. The remaining mission parameters are fixed according to the set of values given in the last column of Table 3. 91
Figure 32 SNR as a function of the distance from the SP $||\xi||$ for the two noise realizations. The remaining parameters are fixed according to the set of values given in the last column of Table 3. 92
Figure 33 SNR as a function of the spacecraft velocity v for the two noise realizations. The remaining parameters are fixed according to the set of values given in the last column of Table 3. We vary the values of velocity within the larger range than given in the Table 2, i.e. from 0 to 4 km/s, to observe the maximum of SNR. 92
Figure 34 SNR as a function of the angles φ and η that determine the direction of the trajectory. The SNR estimates are plotted for the current best noise estimate. The behaviour for the requirements noise is similar, but with magnitudes in the range [8; 12]. The remaining parameters are fixed to the set of values given in the last column of Table 3. 94

Figure 35 Ambiguity function for the fly-by distance $\|\xi\|$ for the two noise realizations. The true value of the parameter is $\|\xi\|_0 = 20\,\text{km}$. The remaining parameters are fixed according to the set of values given in the last column of Table 3. 94

Figure 36 Ambiguity function for the spacecraft velocity v for the two noise realizations. The true value of the parameter is $v_0 = 1.5\,\text{km/s}$. The remaining parameters are fixed according to the set of values given in the last column of Table 3. 95

Figure 37 Two-dimensional ambiguity function for the angles φ and η that determine the direction of the spacecraft trajectory. The results are obtained with the current best noise estimate model. The true values of the parameters are set to $\varphi_0 = 30^\circ$ and $\eta_0 = 70^\circ$ and the remaining parameters are fixed according to the set of values given in the last column of Table 3. Both angles are varied with steps of 1°. The closed contour indicates the location of $\hat{c} = 0.99998$. 96

Figure 38 Ambiguity function for the angle $\eta_\perp$ which defines the position of the perpendicular to the trajectory for the two noise realizations. The true value of the parameter is $\eta_\perp = 90^\circ$ The remaining parameters are fixed according to the set of values given in the last column of Table 3. 98

Figure 39 The (k, a_0) parameter space. The shaded area represents the part of the parameter space ruled out by Eq. (8.7). Crosses indicate points where Eq. (4.15) was solved numerically. Signal templates are built upon these solutions and are used, in turn, to determine signal templates at a generic point (k, a_0) via bicubic interpolation. 105

Figure 40 SNR estimates for the current best noise estimate (right panel) and the requirements noise (left panel). The SNRs are calculated at the points in parameter space where the TeVeS numerical calculations were performed. The triangles correspond to the values of k and a_0 for which the signal templates were injected into the data (see Table 4). 110

Figure 41 Joint posterior probability distribution for the parameters k and a_0 using the current best estimate noise model. Contours represent lines of constant probability density defining regions that enclose 68%, 95%, and 99% of the probability. The panels represent 6 signal injections at the first 6 points in the parameter space listed in Table 5. 112

Figure 42 Same as Fig. 41 but for the requirements noise model. 113

Figure 43 Posterior probability distributions and marginalised posterior distributions for the current best noise estimate for the parameters of the injected signal at $k = 0.08$ and $a_0 = 3.5 \cdot 10^{-10} \mathrm{m/s}^2$. The red lines indicate the true values at which the simulated signal was injected. 116

Figure 44 Posterior probability and marginalised posterior distributions for requirements noise for the parameters of the injected signal at $k = 0.08$ and $a_0 = 3.5 \cdot 10^{-10} m/s^2$. The red lines indicate the true values at which the simulated signal was injected. 117

Figure 45 Posterior probability distributions and marginalised posterior distributions for the current best noise estimate for the parameters of the injected signal $k = 0.017$ and $a_0 = 3.1 \cdot 10^{-10} m/s$. The red lines indicate the true values at which the simulated signal was injected. 118

Figure 46 Same as Fig. 45 but for the requirements noise. 119

Figure 47 Posterior probability distributions and marginalised posterior distributions for the current best noise estimate for parameters of the signal modelled for $k = 0.1$ and $a_0 = 0.68 \cdot 10^{-10} m/s^2$. The red lines indicate the true values at which the simulated signal was injected. 120

Figure 48 Same as Fig. 47 but for the requirements noise. 121

Figure 49 Posterior probability density for the current best estimate noise realisation in the case of no signal injection, i.e. $\tilde{h}(f_j, \lambda_0^m, \lambda_0^t) = 0$. 122

Figure 50 Same as Fig. 49 but for the requirements noise. 123

Figure 51 Histograms of the logarithms of the Bayes factor $\log B$ for the 200 noise realisations (current best estimate) at the 7 representative points in the parameter space, where the signals were injected. These points are listed in Table 4. 124

Figure 52 Same as Fig. 51 but for the requirements noise. 125

Figure 53 Data from the test campaign with a glitch of unknown origin bandpass filtered in the sensitive frequency band of LPF. 132

Figure 54 Resulting posterior probability density for the parameter estimation in case of the realistic data of Fig. 53. 133

Figure 55 LPF simulator 137

Figure 56 Data from the test campaign (cold run) 141

Figure 57 Data from the test campaign (hot run) 142

Figure 58 Distribution of the data compared to the *Normal* distribution and to the cdf of the *Student's t* distribution. This is the probability plot that plots the sorted data versus the quantiles of the Gaussian distribution. 143

Figure 59 Examples of the sine-Gaussian signals with the following parameters: (1) $A = 2 \cdot 10^{-9} m/s^2$, $\varphi = 2\pi n$, $f_0 = 0.1 Hz$, $Q = 0.2$, $t_0 = 20s$ (2) $A = 10^{-9} m/s^2$, $\varphi_0 = 1.8 \pm 2\pi n$, $f_0 = 0.5 Hz$, $Q = 10$, $t_0 = 50s$ (3) $A = 10^{-9} m/s^2$, $\varphi_0 = \pi \pm 2\phi n$, $f_0 = 0.05 Hz$, $Q = 2$, $t_0 = 80s$, with $n \in \mathbb{Z}$ 145

Figure 60 Signal model for several choices of parameters. Functions are plotted on the interval $[0; 1000]$ s and in all cases the time of arrival is fixed to the same value $t_0 = 500$ s. 147

Figure 61 TeVeS parameter space transformed into generalised signal parameter space 149

Figure 62 The noise curve estimated from the data from the test campaign, generated by fitting to the averaged ASD estimate 154

Figure 63 The distribution of the log Bayes factors for the case of the data N. 165

Figure 64 The distribution of the log Bayes factors for the case of the data $S + N$ 166

Figure 65 The distribution of the log Bayes factors for the case of the data $G + N$ 167

Figure 66 The distribution of the log Bayes factors for the case of the data $S + G + N$ 168

Figure 67 Posterior distribution contour plots for data and model assuming the generalised signal model. The contours contain 2.5 %, 16 %, 84 % and 97.5 % of the probability. The lines for each parameter indicate the location of the true values that were injected into simulated data. 172

Figure 68 Posterior distribution contour plots for the data and model assuming the glitch model. The contours contain 2.5 %, 16 %, 84 % and 97.5 % of the probability. The lines for each parameter indicate the location of the true values that were injected into simulated data. 173

Figure 69 Posterior distribution contour plots for the data and model assuming the mixture of the generalised signal and glitch models. The contours contain 2.5 %, 16 %, 84 % and 97.5 % of the probability. The lines for each parameter indicate the location of the true values that were injected into simulated data. 174

LIST OF TABLES

Table 1 Parameters of the Hulse-Taylor pulsar. 19

Table 2 This table lists the seven mission parameters also shown graphically in Fig. 27 and provides estimates for their uncertainties. These parameters can be determined from measurements of the spacecraft position which are based on the spacecraft navigation system without involving the LPF optical readout [41, 1]. The uncertainties on the navigation parameter values before the flight, i.e., before the trajectory for the transition from L1 to SP is chosen, and those determined during the flight are provided in columns three and four, respectively. The errors on the angle, α, that defines the orientation of the solar panel are below 1°: as explained in Sec. 5.5.1, we set $\alpha = 90^\circ$ and the error may be neglected within the scope of this thesis. Additionally, the time of closest approach to the SP is not included in the parameter list as it is of the order of several seconds and can be neglected with respect to the signal length. 77

Table 3 This table lists the seven mission parameters also shown graphically in Fig. 27 and provides the ranges in which their values are varied to produce Fig. 30, and the values assigned to them during our parameter estimation analyses. The values reported in the last column are those used for the analysis of the theory parameters. These numbers are based on [105] and [41]. While, recent investigations show that it may be possible to realise a trajectory directly through the SP, we have conservatively set $\|\xi\| = 20\,\mathrm{km}$. 99

Table 4 Values of k and a_0 for which the signal template was injected in the data to probe parameter estimation. 110

Table 5 Average values of the standard deviations $\overline{\Delta k}$ and $\overline{\Delta a_0}$ of the one dimensional posteriors of the parameters. The values are given for the 6 points in the (k, a_0) parameter space where the *true* signal injections were made. The averages are determined from 200 different noise realisations (using the current best estimate noise) and posterior estimates truncated by our priors are artificially reduced. 115

Table 6 The list of the Bayes Ratios that represent all possible combinations of the models studied in this work. 153

Table 7 Simulations where run for all possible combinations of data and signal models. The results of the Bayes Factor distributions are presented in the Figures that are given in this table 159

Table 8 Probabilities for one model to be preferred over the other one. Results for the data with only noise present $\tilde{x}_j = \tilde{n}_j$. 163

Table 9 Probabilities for one model to be preferred over the other one. Results for the data with the signal in noise $\tilde{x}_j = \tilde{s}_j + \tilde{n}_j$. Bayes Factors are calculated with the *Student's t* likelihood. 163

Table 10 Probabilities for one model to be preferred over the other one. Results for the data with the glitch in noise $\tilde{x}_j = \tilde{g}_j + \tilde{n}_j$. Bayes Factors are calculated with the *Student's t* likelihood. 164

Table 11 Probabilities for one model to be preferred over the other one. Results for the data with the signal and the glitch in noise $\tilde{x}_j = \tilde{s}_j + \tilde{g}_j + \tilde{n}_j$. Bayes Factors are calculated with the *Student's t* likelihood. 164

Table 12 Results of the parameter estimation for the generalised signal model. The mean and the standard deviation of the posterior probabilities of the parameters are presented. 170

Table 13 Results of the parameter estimation for the glitch model. The mean and the standard deviation of the posterior probabilities of the parameters are presented. 170

Table 14 Results of the parameter estimation for the mixture of the generalised signal and glitch models. The mean and the standard deviation of the posterior probabilities of the parameters are presented. 171

CURRICULUM VITAE

PERSONAL INFORMATION

Name	Natalia Korsakova
Place of birth	Leningrad, USSR
Date of birth	February 26, 1985

EDUCATION

2010 – 2015	Doctoral student	Max Planck Institute for Gravitational Physics (Albert Einstein Institute) and Institute for Gravitational Physics of the Leibniz Universität Hannover
2007 – 2010	Master of Science	University of Eastern Finland, School of Computing
2002 – 2007	Diploma	Saint-Petersburg State University, Faculty of Mathematics and Mechanics, Laboratory of Theoretical Astrophysics

WORKING EXPERIENCE

2010	VTT Technical Research Centre of Finland	Data Mining group
2008 – 2010	Helsinki University of Technology (from 2010 Aalto University)	Department of Information and Computer Science Deep Learning and Bayesian Modelling Group
2006 – 2007	Moscow State University	Laboratory of Gravitational measurements

PUBLICATIONS

- *Data analysis methods for testing alternative theories of gravity with LISA Pathfinder*; Natalia Korsakova, Chris Messenger, Francesco Pannarale, Martin Hewitson and Michele Armano; Phys. Rev. D 89; doi:10.1103/PhysRevD.89.123511

- *Data series subtraction with unknown and unmodeled background noise*; Stefano Vitale, ... ,Natalia Korsakova, ...; Phys. Rev. D 90; doi:10.1103/PhysRevD.90.042003

- *Bayesian model selection for LISA Pathfinder*; Nikolaos Karnesis, ... Natalia Korsakova, ...;
  Phys. Rev. D 89; doi:10.1103/PhysRevD.89.06200

- *Improving Bayesian analysis for LISA Pathfinder using an efficient Markov Chain Monte Carlo method*; Luigi Ferraioli, ..., Natalia Korsakova, ...; Experimental Astronomy 37; doi:10.1007/s10686-014-9372-7

- *Kolmogorov-Smirnov like test for time-frequency Fourier spectrogram analysis in LISA Pathfinder*; Luigi Ferraioli, ..., Natalia Korsakova, ...; Experimental Astronomy 39; doi:10.1007/s10686-014-9432-z

- *Drifting linear dynamics*; Tapani Raiko, Alexander Ilin, Natalia Korsakova, Erkki Oja, Harri Valpola; Proceedings of the 13th International Conference on Artificial Intelligence and Statistics

- *Bayesian statistics for the calibration of the LISA Pathfinder experiment*; Michele Armano, ..., Natalia Korsakova, ...; Proceedings of the 10th International LISA Symposium; doi: 088/1742-6596/610/1/012027

- *State space modelling and data analysis exercises in LISA Pathfinder*; Miquel Nofrarias, ..., Natalia Korsakova, ...; Proceedings of the 9th International LISA Symposium
- *Disentangling the magnetic force noise contribution in LISA Pathfinder*; Michele Armano, ..., Natalia Korsakova, ...; Journal of Physics: Conference Series, volume 610, conference 1; doi:10.1088/1742-6596/610/1/012024
- *A Strategy to Characterize the LISA-Pathfinder Cold Gas Thruster System*; Michele Armano, ..., Natalia Korsakova, ...; Proceedings of the 10th International LISA Symposium; doi:10.1088/1742-6596/610/1/012026
- *In-flight thermal experiments for LISA Pathfinder: Simulating temperature noise at the Inertial Sensors*; Ferran Gilbert, ..., Natalia Korsakova, ..., Proceedings of the 10th International LISA Symposium; doi:088/1742-6596/610/1/012023
- *A noise simulator for eLISA: Migrating LISA Pathfinder knowledge to the eLISA mission*; Michele Armano, ..., Natalia Korsakova, ...; Proceedings of the 10th International LISA Symposium; doi:10.1088/1742-6596/610/1/012036
- *Free-flight experiments in LISA Pathfinder*; Michele Armano, ..., Natalia Korsakova, ...; Proceedings of the 10th International LISA Symposium; doi:10.1088/1742-6596/610/1/012006
- *The Gravitational Universe*; White paper; Pao Amaro Seoane, ..., Natalia Korsakova, ...

ACKNOWLEDGMENTS

During my PhD studies I have met so many wonderful people so it will be very hard to mention them all here.

First of all I want to thank Professor Karsten Danzmann for giving me the opportunity to do my PhD at the AEI and for being such an encouraging person.

I want to thank Martin Hewitson for suggesting me the topic and for always being there to help and Gerhard Heinzel for a wonderful atmosphere in the LISA group where I enjoyed my time during those years.

I cannot express how thankful I am to Chris Messenger and Francesco Pannarale, who during these year have taught me so many things and with whom I enjoyed working so much. I want to thank them for dedicating their time to me and for being patient.

From the first days at the AEI I had found a friend to talk about science and everything else, my dear Philip Peterson. That was a great time, when you were living in Hannover, I will always remember it and I hope we will always stay in touch.

I want to thank Heather Audley for being my friend and my flatmate, for time that we have spent together, for her understanding, and her creativity that made our Institute such a fun place. And, of course, for coming back to Hannover!

I want to thank people who have already left out Institute but whom I was lucky to meet while they were here, Ben Sheard, Yan Wang, Johanna Bogenstahl, Miquel Nofrarias, Antonio Garcia Martin, Pablo Rosado, Giulio Mazzolo, Jacob Slutsky and many others.

I want to thank people from the data anaysis group for the lovely time spent together, for the trips and for 4 o'clock coffee breaks.

I want to express my gratitude to all members of the LISA Pathfinder collaboration for a great working atmosphere and especially for very enjoyable times during STOC Simulations.

In particular, I want to thank my office mates, who where able to survive my company and remain very nice to me during all these years, Daniel Schütze and Gunnar Stede.

I want to thank Tom Dent, Alex Nilsen, Chris Messenger, Francesco Pannarale, Martin Hewitson, Nikos Karnesis and Sarah Paczkowski for reading my thesis and for their useful comments.

I want to thank Bergit Ohlendorf for her irreplacable help and for meeting me at the airport on the first day when I came to Hannover.

I want to thank Germán Fernández Barranco for letting me do the defence on the day of his seminar. Sorry German.

In the end I want to thank my friends who mean so much to me and who have always found time to meet, to travel and to be together independent of the distance that is separating us now. I want to thank my family, without their support I would not be able to achieve anything in my life.

BIBLIOGRAPHY

[1] Private communication with Christian Trenkel and Stephen Kemble.

[2] Computer clusters at the AEI. URL `http://www.aei.mpg.de/96456/20_Computer_Clusters`.

[3] LTPDA toolbox. URL `https://www.elisascience.org/ltpda/`.

[4] The gravitational universe. `https://www.elisascience.org/dl/TheGravitationalUniverse.pdf`, 2013. Science theme, as addressed by the eLISA mission concept.

[5] F. Acernese et al. Advanced virgo baseline design, 2009. URL `https://tds.ego-gw.it/itf/tds/file.php?callFile=VIR-0027A-09.pdf`.

[6] European Space Agency. Timeline for selection of l-class missions. URL `http://sci.esa.int/cosmic-vision/42369-l-class-timeline`.

[7] P. Ajith. Addressing the spin question in gravitational-wave searches: Waveform templates for inspiralling compact binaries with nonprecessing spins. *Phys. Rev. D*, 84:084037, Oct 2011. doi: 10.1103/PhysRevD.84.084037. URL `http://link.aps.org/doi/10.1103/PhysRevD.84.084037`.

[8] P. Ajith and Sukanta Bose. Estimating the parameters of non-spinning binary black holes using ground-based gravitational-wave detectors: Statistical errors. *Phys. Rev. D*, 79:084032, Apr 2009. doi: 10.1103/PhysRevD.79.084032. URL `http://link.aps.org/doi/10.1103/PhysRevD.79.084032`.

[9] Pau Amaro-Seoane et al. Low-frequency gravitational-wave science with elisa/ngo. *Classical and Quantum Gravity*, 29(12):

124016, 2012. URL `http://stacks.iop.org/0264-9381/29/i=12/a=124016`.

[10] Pau Amaro-Seoane et al. Low-frequency gravitational-wave science with elisa/ngo. *Classical and Quantum Gravity*, 29(12): 124016, 2012. URL `http://stacks.iop.org/0264-9381/29/i=12/a=124016`.

[11] Pau Amaro-Seoane et al. eLISA/NGO: Astrophysics and cosmology in the gravitational-wave millihertz regime. *GW Notes*, 6:4–110, 2013.

[12] F Antonucci et al. The LISA Pathfinder mission. *Classical and Quantum Gravity*, 29(12):124014, June 2012. doi: 10.1088/0264-9381/29/12/124014.

[13] M Armano et al. Lisa pathfinder: the experiment and the route to lisa. *Classical and Quantum Gravity*, 26(9):094001, 2009. URL `http://stacks.iop.org/0264-9381/26/i=9/a=094001`.

[14] P. Astone, M. Bassan, E. Coccia, S. D'Antonio, V. Fafone, G. Giordano, A. Marini, Y. Minenkov, I. Modena, A. Moleti, G. V. Pallottino, G. Pizzella, A. Rocchi, F. Ronga, R. Terenzi, and M. Visco. Analysis of 3 years of data from the gravitational wave detectors explorer and nautilus. *Phys. Rev. D*, 87:082002, Apr 2013. doi: 10.1103/PhysRevD.87.082002. URL `http://link.aps.org/doi/10.1103/PhysRevD.87.082002`.

[15] S Barke, Y Wang, J J Esteban Delgado, M Tröbs, G Heinzel, and K Danzmann. Towards a gravitational wave observatory designer: sensitivity limits of spaceborne detectors. *Classical and Quantum Gravity*, 32(9):095004, 2015. URL `http://stacks.iop.org/0264-9381/32/i=9/a=095004`.

[16] J. D. Bekenstein. Relativistic gravitation theory for the modified Newtonian dynamics paradigm. *Phys. Rev. D*, 70(8):083509, October 2004. doi: 10.1103/PhysRevD.70.083509.

[17] Jacob D. Bekenstein. Relation between physical and gravitational geometry. *Phys. Rev. D*, 48:3641–3647, Oct 1993. doi: 10.1103/PhysRevD.48.3641. URL `http://link.aps.org/doi/10.1103/PhysRevD.48.3641`.

[18] Jacob D. Bekenstein and Robert H. Sanders. Gravitational lenses and unconventional gravity theories. *The Astrophysical Journal*, 429:480, 1994. doi: 10.1086/174337.

[19] B. Bertotti, B. J. Carr, and M. J. Rees. Limits from the timing of pulsars on the cosmic gravitational wave background. *Monthly Notice of the Royal Astronomical Society*, 203:945–954, June 1983. URL `http://adsabs.harvard.edu/abs/1983MNRAS.203..945B`.

[20] Neil Bevis, João Magueijo, Christian Trenkel, and Steve Kemble. MONDian three-body predictions for LISA Pathfinder. *Classical and Quantum Gravity*, 27(21):215014, November 2010. ISSN 0264-9381. doi: 10.1088/0264-9381/27/21/215014. URL `http://stacks.iop.org/0264-9381/27/i=21/a=215014?key=crossref.3f3b7bbbe513bd676f8c94e8b0f46e55`.

[21] Luc Blanchet. Gravitational radiation from post-newtonian sources and inspiralling compact binaries. *Living Reviews in Relativity*, 9(4), 2006. URL `http://relativity.livingreviews.org/Articles/lrr-2006-4/`.

[22] Roger Blandford, Ramesh Narayan, and RogerW. Romani. Arrival-time analysis for a millisecond pulsar. *Journal of Astrophysics and Astronomy*, 5(4):369–388, 1984. doi: 10.1007/BF02714466. URL `http://dx.doi.org/10.1007/BF02714466`.

[23] Matthias Blau. Lecture notes on general relativity. 2014. URL `http://www.blau.itp.unibe.ch/newlecturesGR.pdf`.

[24] A. Bosma. 21-cm line studies of spiral galaxies. II. The distribution and kinematics of neutral hydrogen in spiral galaxies of various morphological types. *Astronomical Journal*, 86: 1825–1846, December 1981. doi: 10.1086/113063. URL `http://adsabs.harvard.edu/abs/1981AJ.....86.1825B`.

[25] Alessandra Buonanno. Gravitational waves. In *Les Houches Summer School - Session 86: Particle Physics and Cosmology: The Fabric of Spacetime Les Houches, France, July 31-August 25, 2006*, 2007. URL `http://inspirehep.net/record/762437/files/arXiv:0709.4682.pdf`.

[26] Sean Carroll. *Spacetime and geometry: an introduction to general relativity*. Pearson Education Limited, 2013.

[27] Timothy Clifton, Pedro G. Ferreira, Antonio Padilla, and Constantinos Skordis. Modified gravity and cosmology. *Physics Reports*, 513:1 – 189, 2012. doi: http://dx.doi.org/10.1016/j.physrep.2012.01.001. URL `http://www.sciencedirect.com/science/article/pii/S0370157312000105`.

[28] Neil J Cornish and Shane L Larson. Space missions to detect the cosmic gravitational-wave background. *Classical and Quantum Gravity*, 18(17):3473, 2001. URL `http://stacks.iop.org/0264-9381/18/i=17/a=308`.

[29] Neil J. Cornish and Tyson B. Littenberg. BayesWave: Bayesian Inference for Gravitational Wave Bursts and Instrument Glitches. *Classical and Quantum Gravity*, 32(13):135012, 2015. doi: 10.1088/0264-9381/32/13/135012. URL `http://stacks.iop.org/0264-9381/32/i=13/a=135012`.

[30] Neil J. Cornish and Louis J. Rubbo. Lisa response function. *Phys. Rev. D*, 67:022001, Jan 2003. doi: 10.1103/PhysRevD.67.022001. URL `http://link.aps.org/doi/10.1103/PhysRevD.67.022001`.

[31] Curt Cutler. Angular resolution of the lisa gravitational wave detector. *Phys. Rev. D*, 57:7089–7102, Jun 1998. doi: 10.1103/PhysRevD.57.7089. URL `http://link.aps.org/doi/10.1103/PhysRevD.57.7089`.

[32] T Dal Canton, S Bhagwat, S V Dhurandhar, and A Lundgren. Effect of sine-gaussian glitches on searches for binary coalescence. *Classical and Quantum Gravity*, 31(1), 2014. doi: 10.

1088/0264-9381/31/1/015016. URL `http://stacks.iop.org/0264-9381/31/i=1/a=015016`.

[33] T. Damour and G. Esposito-Farèse. Tensor-multi-scalar theories of gravitation. *Class. Quantum Grav.*, 9:2093–2176, 1992. doi: 10.1088/0264-9381/9/9/015.

[34] Stefan L. Danilishin and Farid Ya. Khalili. Quantum measurement theory in gravitational-wave detectors. *Living Reviews in Relativity*, 15(5), 2012. doi: 10.12942/lrr-2012-5. URL `http://www.livingreviews.org/lrr-2012-5`.

[35] M. M. Davis, J. H. Taylor, J. M. Weisberg, and D. C. Backer. High-precision timing observations of the millisecond pulsar psr1937 + 21. *Nature*, 315(6020):547–550, 1985. URL `http://dx.doi.org/10.1038/315547a0`.

[36] S. Detweiler. Pulsar timing measurements and the search for gravitational waves. *Astrophysical journal*, 234:1100–1104, December 1979.

[37] S. V. Dhurandhar and B. S. Sathyaprakash. Choice of filters for the detection of gravitational waves from coalescing binaries. II. Detection in colored noise. *Physical Review D*, 49:1707–1722, February 1994. doi: 10.1103/PhysRevD.49.1707.

[38] Michal Dominik, Emanuele Berti, Richard O?Shaughnessy, Ilya Mandel, Krzysztof Belczynski, Christopher Fryer, Daniel E. Holz, Tomasz Bulik, and Francesco Pannarale. Double compact objects iii: Gravitational-wave detection rates. *The Astrophysical Journal*, 806(2):263, 2015. URL `http://stacks.iop.org/0004-637X/806/i=2/a=263`.

[39] Albert Einstein. Die feldgleichungen der gravitation. 1915.

[40] Albert Einstein. Prinzipielles zur allgemeinen relativitätstheorie. 1917.

[41] E. Fabacher, S. Kemble, C. Trenkel, and N. Dunbar. Multiple Sun-Earth Saddle Point flybys for LISA Pathfinder. *Advances in*

Space Research, 52:105–116, July 2013. doi: 10.1016/j.asr.2013.02.005.

[42] J. E. Faller and P. L. Bender. A possible laser gravitational wave experiment in space. In B. N. Taylor and W. D. Phillips, editors, *Precision measurement and fundamental constants II*, pages 689–690, 1984. JILA Pub. 2593.

[43] Benoit Famaey and Stacy McGaugh. Modified Newtonian Dynamics (MOND): Observational Phenomenology and Relativistic Extensions. *Living Reviews in Relativity*, 15(10), 2012.

[44] Antonio De Felice and Shinji Tsujikawa. f(r) theories. *Living Reviews in Relativity*, 13(3), 2010. doi: 10.12942/lrr-2010-3. URL `http://www.livingreviews.org/lrr-2010-3`.

[45] F Feroz, M P Hobson, and M Bridges. MultiNest: an efficient and robust Bayesian inference tool for cosmology and particle physics. *Monthly Notices of the Royal Astronomical Society*, 398(4):1601–1614, October 2009. ISSN 00358711. doi: 10.1111/j.1365-2966.2009.14548.x. URL `http://mnras.oxfordjournals.org/cgi/doi/10.1111/j.1365-2966.2009.14548.x`.

[46] Valeria Ferrari and Leonardo Gualtieri. General relativity, 2014–2015. URL `http://www.roma1.infn.it/teongrav/VALERIA/TEACHING/ONDE_GRAV_STELLE_BUCHINERI/AA2013_14/dispense.pdf`.

[47] A. Fienga, J. Laskar, P. Kuchynka, C. Le Poncin-Lafitte, H. Manche, and M. Gastineau. Gravity tests with INPOP planetary ephemerides. In S. A. Klioner, P. K. Seidelmann, and M. H. Soffel, editors, *IAU Symposium*, volume 261 of *IAU Symposium*, pages 159–169, January 2010. doi: 10.1017/S1743921309990330.

[48] Ewan D. Fitzsimons. *Techniques for Precision Interferometry in Space*. PhD thesis, School University of Glasgow, 2010.

[49] R Flatscher, R Gerndt, K Rogalla, N Gradmann, and D Kolbe. Test Report on OMS Performance Parameter Characterization

During OSTT. Technical report, Astrium Ltd., Astrium Satellite GmbH (Astrium Deutschland (ASD)), 2013.

[50] K. C. Freeman. On the Disks of Spiral and so Galaxies. *Astrophysical journal*, 160:811, June 1970. doi: 10.1086/150474. URL `http://adsabs.harvard.edu/abs/1970ApJ...160..811F`.

[51] Paulo C. C. Freire, Norbert Wex, Gilles Esposito-Farèse, Joris P. W. Verbiest, Matthew Bailes, Bryan A. Jacoby, Michael Kramer, Ingrid H. Stairs, John Antoniadis, and Gemma H. Janssen. The relativistic pulsar?white dwarf binary psr j1738+0333 ? ii. the most stringent test of scalar?tensor gravity. 423(4):3328–3343, 2012. doi: 10.1111/j.1365-2966.2012.21253.x.

[52] Jonathan R. Gair, Michele Vallisneri, Shane L. Larson, and John G. Baker. Testing general relativity with low-frequency, space-based gravitational-wave detectors. *Living Reviews in Relativity*, 16(7), 2013. doi: 10.12942/lrr-2013-7. URL `http://www.livingreviews.org/lrr-2013-7`.

[53] Andrew Gelman, John B. Carlin, Hal S. Stern, David B. Dunson, Aki Vehtari, and Donald B. Rubin. *Bayesian Data Analysis*. Chapman and Hall/CRC, 2013.

[54] G. Gentile, G. I. G. Józsa, P. Serra, G. H. Heald, W. J. G. de Blok, F. Fraternali, M. T. Patterson, R. A. M. Walterbos, and T. Oosterloo. HALOGAS: Extraplanar gas in NGC 3198. *Astronomy and Astrophysics*, 554, 2013. doi: 10.1051/0004-6361/201321116.

[55] S.W. Hawking and G.F.R. Ellis. *The large scale structure of spacetime*. Cambridge University Press, 1973.

[56] Gerald Hechenblaikner and Reinhold Flatscher. Fundamental performance determining factors of the ultrahigh-precision space-borne optical metrology system for the LISA Pathfinder mission. In Bernd Bodermann, Karsten Frenner, and Richard M. Silver, editors, *Society of Photo-Optical Instrumentation Engineers (SPIE) Conference Series*, vol-

ume 8789 of *Society of Photo-Optical Instrumentation Engineers (SPIE) Conference Series*, 2013. doi: 10.1117/12.2020498. URL `http://proceedings.spiedigitallibrary.org/proceeding.aspx?doi=10.1117/12.2020498`.

[57] Gerald Hechenblaikner, Rüdiger Gerndt, Ulrich Johann, Peter Luetzow-Wentzky, Vinzenz Wand, Heather Audley, Karsten Danzmann, Antonio Garcia-Marin, Gerhard Heinzel, Miquel Nofrarias, and Frank Steier. Coupling characterization and noise studies of the optical metrology system onboard the LISA Pathfinder mission. *Applied Optics*, 49(29):5665–77, October 2010. ISSN 1539-4522. URL `http://www.ncbi.nlm.nih.gov/pubmed/20935714`.

[58] David Hilbert. Grundlagen der physik (Erste Mitteilung), 1915.

[59] D. Hils, P. L. Bender, and R. F. Webbink. Gravitational radiation from the Galaxy. *The Astrophysical Journal*, 360:75–94, 1990. doi: 10.1086/169098.

[60] Christopher M. Hirata. Lecture XXXIII: Lagrangian formulation of GR. URL `www.tapir.caltech.edu/~chirata/ph236/`.

[61] Scott A. Hughes and Kip S. Thorne. Seismic gravity-gradient noise in interferometric gravitational-wave detectors. *Phys. Rev. D*, 58:122002, Nov 1998. doi: 10.1103/PhysRevD.58.122002. URL `http://link.aps.org/doi/10.1103/PhysRevD.58.122002`.

[62] Scott A. Hughes, Szabolcs Marka, Peter L. Bender, and Craig J. Hogan. New physics and astronomy with the new gravitational wave observatories. *eConf*, C010630:P402, 2001.

[63] R.A. Hulse and J.H. Taylor. Discovery of a pulsar in a binary system. *The Astrophysical Journal*, 195, 1975.

[64] LISA international science team. Lisa, unveiling a hidden universe, assessment study report. Technical report, ESA, February 2011. URL `http://sci.esa.int/lisa/48364-lisa-assessment-study-report-yellow-book/`.

[65] Ted Jacobson. *Einstein-Æther gravity: theory and observational constraints*, chapter 14, pages 92–99. doi: 10.1142/9789812779519_0014. URL `http://www.worldscientific.com/doi/abs/10.1142/9789812779519_0014`.

[66] Ted Jacobson. Einstein-Æther gravity: A Status report. *PoS*, QG-PH:020, 2007.

[67] Harold Jeffreys. *Theory of Probability*. Oxford University Press, 1961.

[68] Duncan R. Lorimer. Binary and millisecond pulsars. *Living Reviews in Relativity*, 11(8), 2008. doi: 10.12942/lrr-2008-8. URL `http://www.livingreviews.org/lrr-2008-8`.

[69] J. Magueijo and A. Mozaffari. Case for testing modified newtonian dynamics using lisa pathfinder. *Phys. Rev. D*, 85: 043527, Feb 2012. doi: 10.1103/PhysRevD.85.043527. URL `http://link.aps.org/doi/10.1103/PhysRevD.85.043527`.

[70] J. Magueijo and A. Mozaffari. Saddle stresses for generic theories with a preferred acceleration scale. *Phys. Rev. D*, 86: 123518, Dec 2012. doi: 10.1103/PhysRevD.86.123518. URL `http://link.aps.org/doi/10.1103/PhysRevD.86.123518`.

[71] M. Milgrom. A modification of the Newtonian dynamics as a possible alternative to the hidden mass hypothesis. *The Astrophysical Journal*, 270:365–370, July 1983. doi: 10.1086/161130.

[72] Mordehai Milgrom. Bimetric mond gravity. *Phys. Rev. D*, 80: 123536, Dec 2009. doi: 10.1103/PhysRevD.80.123536. URL `http://link.aps.org/doi/10.1103/PhysRevD.80.123536`.

[73] V. N. Mironovskii. Gravitational Radiation of Double Stars. *Soviet Astronomy*, 9:752, 1966. URL `http://adsabs.harvard.edu/abs/1966SvA.....9..752M`.

[74] Charles W Misner, Kip S Thorne, and John Archibald Wheeler. *Gravitation*. W.H Freeman and Company, 1973.

[75] Anneke Monsky et al. The first mock data challenge for LISA Pathfinder. *Classical and Quantum Gravity*, 26(9):094004, May 2009. doi: 10.1088/0264-9381/26/9/094004.

[76] Gunnar Nordström. Über die möglichkeit, das elektomagnetische feld und das gravitationsfeld zu vereinigen. *Physik. Zeitschr.*, XV:504–506, 1914.

[77] J. H. Oort. The force exerted by the stellar system in the direction perpendicular to the galactic plane and some related problems. *Bulletin of the Astronomical Institutes of the Netherlands*, 6:249, August 1932. URL `http://adsabs.harvard.edu/abs/1932BAN.....6..249O`.

[78] J. P. Ostriker and P. J. E. Peebles. A Numerical Study of the Stability of Flattened Galaxies: or, can Cold Galaxies Survive? *Astrophysical Journal*, 186:467–480, December 1973. doi: 10.1086/152513. URL `http://adsabs.harvard.edu/abs/1973ApJ...186..467O`.

[79] Francesco Pannarale, Emanuele Berti, Koutarou Kyutoku, and Masaru Shibata. Nonspinning black hole-neutron star mergers: A model for the amplitude of gravitational waveforms. *Phys. Rev. D*, 88:084011, Oct 2013. doi: 10.1103/PhysRevD.88.084011. URL `http://link.aps.org/doi/10.1103/PhysRevD.88.084011`.

[80] E.V. Pitjeva. Updated iaa ras planetary ephemerides-epm2011 and their use in scientific research. *Solar System Research*, 47(5):386–402, 2013. ISSN 0038-0946. doi: 10.1134/S0038094613040059. URL `http://dx.doi.org/10.1134/S0038094613040059`.

[81] William H. Press, Brian P. Flannery, Saul A. Teukolsky, and William T. Vetterling. *Numerical Recipes in C: The Art of Scientific Computing*. Cambridge University Press, New York, NY, USA, 1988. ISBN 0-521-35465-X.

[82] V.I. Pustovoit and M.E. Gertsenshtein. Gravitational radiation by a relativistic particle. *Soviet Physics Journal of Experimental and Theoretical Physics*, 15(1), July 1962.

[83] Giuseppe D. Racca and Paul W. McNamara. The lisa pathfinder mission. *Space Science Reviews*, 151(1-3):159–181, 2010. ISSN 0038-6308. doi: 10.1007/s11214-009-9602-x. URL `http://dx.doi.org/10.1007/s11214-009-9602-x`.

[84] Nathan Rosen. A bi-metric theory of gravitation. *General Relativity and Gravitation*, 4(6):435–447, 1973. ISSN 0001-7701. doi: 10.1007/BF01215403. URL `http://dx.doi.org/10.1007/BF01215403`.

[85] Christian Röver. Degrees-of-freedom estimation in the student-t noise model. Technical Report LIGO-T1100497. URL `https://dcc.ligo.org/LIGO-T1100497/public`.

[86] Christian Röver. Student-t based filter for robust signal detection. *Phys. Rev. D*, 84:122004, Dec 2011. doi: 10.1103/PhysRevD.84.122004. URL `http://link.aps.org/doi/10.1103/PhysRevD.84.122004`.

[87] Christian Röver, Renate Meyer, and Nelson Christensen. Modelling coloured residual noise in gravitational-wave signal processing. *Classical and Quantum Gravity*, 28(1), 2011. URL `http://stacks.iop.org/0264-9381/28/i=1/a=015010`.

[88] V. C. Rubin and W. K. Ford, Jr. Rotation of the Andromeda Nebula from a Spectroscopic Survey of Emission Regions. *Astrophysical Journal*, 159:379, February 1970. doi: 10.1086/150317. URL `http://adsabs.harvard.edu/abs/1970ApJ...159..379R`.

[89] V. C. Rubin, W. K. Ford, Jr., N. Thonnard, and D. Burstein. Rotational properties of 23 SB galaxies. *Astrophysical Journal*, 261:439–456, October 1982. doi: 10.1086/160355. URL `http://adsabs.harvard.edu/abs/1982ApJ...261..439R`.

[90] R. H. Sanders. A Stratified framework for scalar - tensor theories of modified dynamics. *The Astrophysical Journal*, 480:492–502, 1997. doi: 10.1086/303980.

[91] B S Sathyaprakash and Bernard F Schutz. Physics, Astrophysics and Cosmology with Gravitational Waves. *Living Reviews in Relativity*, 12(2), 2009.

[92] M.V. Sazhin. Possibility of detecting superlong gravitational waves. *Astronomicheskij zhurnal*, 55(1):65–68, 1978.

[93] Bernard Schutz. *A first course in General Relativity*. Cambridge University Press, second edition, 2009.

[94] Bernard F Schutz and Franco Ricci. Gravitational Waves, Sources, and Detectors. 2010.

[95] Naoki Seto, Seiji Kawamura, and Takashi Nakamura. Possibility of direct measurement of the acceleration of the universe using 0.1 hz band laser interferometer gravitational wave antenna in space. *Phys. Rev. Lett.*, 87:221103, Nov 2001. doi: 10.1103/PhysRevLett.87.221103. URL `http://link.aps.org/doi/10.1103/PhysRevLett.87.221103`.

[96] David Shoemaker and LIGO Scientific Collaboration. Advanced ligo anticipated sensitivity curves, 2010. URL `https://dcc.ligo.org/LIGO-T0900288/public`.

[97] D. Sivia and J. Skilling. *Data Analysis: A Bayesian Tutorial*. Oxford science publications. OUP Oxford, 2006. ISBN 9780198568322.

[98] John Skilling. Nested Sampling. In *AIP Conference Proceedings*, volume 735, pages 395–405. AIP, 2004. doi: 10.1063/1.1835238. URL `http://link.aip.org/link/?APC/735/395/1&Agg=doi`.

[99] John Skilling. Nested sampling for general bayesian computation. *Bayesian Analysis*, 1(4):833–859, 12 2006. doi: 10.1214/06-BA127. URL `http://dx.doi.org/10.1214/06-BA127`.

[100] Kentaro Somiya. Detector configuration of kagra?the japanese cryogenic gravitational-wave detector. *Classical and Quantum Gravity*, 29(12):124007, 2012. URL `http://stacks.iop.org/0264-9381/29/i=12/a=124007`.

[101] E. Myles Standish and James G. Williams. Orbital ephemerides of the sun, moon, and planets. In Sean E. Urban and P. Kenneth Seidelmann, editors, *Explanatory Supplement to the Astronomical Almanac*. Univ Science Books, 2012. URL `ftp://ssd.jpl.nasa.gov/pub/eph/planets/ioms/ExplSupplChap8.pdf`.

[102] LISA study team. Laser interferometer space antenna for the detection and observation of gravitational waves, pre-phase a report. Technical report, MPQ, July 1998. URL `http://lisa.nasa.gov/Documentation/ppa2.08.pdf`.

[103] J. H. Taylor, L. A. Fowler, and P. M. McCulloch. Measurements of general relativistic effects in the binary pulsar psr1913 + 16. *Nature*, 277(5696):437–440, 02 1979. URL `http://dx.doi.org/10.1038/277437a0`.

[104] Kip S. Thorne. Gravitational radiation. In S.W. Hawking and W. Israel, editors, *Three Hundred Years of Gravitation*, pages 330–458. Cambridge University Press, Cambridge, 1987.

[105] C. Trenkel, S. Kemble, N. Bevis, and J. Magueijo. Testing Modified Newtonian Dynamics with LISA Pathfinder. *Advances in Space Research*, 50:1570–1580, December 2012. doi: 10.1016/j.asr.2012.07.024.

[106] T. S. van Albada, J. N. Bahcall, K. Begeman, and R. Sancisi. Distribution of dark matter in the spiral galaxy NGC 3198. *Astrophysical Journal*, 295:305–313, August 1985. doi: 10.1086/163375. URL `http://adsabs.harvard.edu/abs/1985ApJ...295..305V`.

[107] S Vitale. Measurement of differential acceleration noise on LISA Pathfinder. *S2-UTN-TN-3053*, 2007.

[108] S. Vitale, K. Danzmann, P. Mcnamara, M Armano, R Dolesi, C Dunn, A Garcia Marin, G Heinzel, and Cesar Garcia. Lisa pathfinder experiments master plan, 2006.

[109] Stefano Vitale et al. Data series subtraction with unknown and unmodeled background noise. *Phys. Rev. D*, 90:042003, Aug 2014. doi: 10.1103/PhysRevD.90.042003. URL `http://link.aps.org/doi/10.1103/PhysRevD.90.042003`.

[110] J. Weber. Detection and generation of gravitational waves. *Phys. Rev.*, 117:306–313, Jan 1960. doi: 10.1103/PhysRev.117.306. URL `http://link.aps.org/doi/10.1103/PhysRev.117.306`.

[111] Joel M. Weisberg and Joseph H. Taylor. Relativistic binary pulsar b1913+16: Thirty years of observations and analysis. *ASP Conf.Ser.*, 328:25, 2005.

[112] Joel M. Weisberg, Joseph H. Taylor, and Lee A. Fowler. Gravitational waves from an orbiting pulsar. *Scientific American*, 1981.

[113] Peter D. Welch. The use of fast fourier transform for the estimation of power spectra: A method based on time averaging over short, modified periodograms. *Audio and Electroacoustics, IEEE Transactions on*, 15(2):70–73, Jun 1967. ISSN 0018-9278. doi: 10.1109/TAU.1967.1161901.

[114] Clifford M. Will. *Theory and Experiment in Gravitational Physics*. Cambridge University Press, March 1993.

[115] Clifford M. Will. The confrontation between general relativity and experiment. *Living Reviews in Relativity*, 17(4), 2014. doi: 10.12942/lrr-2014-4. URL `http://www.livingreviews.org/lrr-2014-4`.

[116] F. Zwicky. Republication of: The redshift of extragalactic nebulae. *General Relativity and Gravitation*, 41(1):207–224, 2009. ISSN 0001-7701. doi: 10.1007/s10714-008-0707-4. URL `http://dx.doi.org/10.1007/s10714-008-0707-4`.

[117] Éanna É Flanagan and Scott A Hughes. The basics of gravitational wave theory. *New Journal of Physics*, 7(1):204, 2005. URL `http://stacks.iop.org/1367-2630/7/i=1/a=204`.